BSc Karin Malli

Enhancement of iron-based Oxygen Carriers for the Steam-Iron Process: Effects of Preparation Methods and Additive Metals on Hydrogen Production

MASTER'S THESIS

to achieve the university degree of

Diplom-Ingenieurin

Master's degree programme: Technical Chemistry

submitted to

Graz University of Technology

Supervisor
Assoc.-Prof. Dipl.-Ing. Dr.techn. Viktor Hacker

Institute of Chemical Engineering and Environmental Technology

Graz, July 2016

Abstract

This work aims to optimise the iron-based oxygen carrier for the steam-iron process (SIP). One of the main challenges for SIP is to prepare an oxygen carrier (OC) which can undergo a high number of consecutive hydrogen production (oxidation) and regeneration steps (reduction) at elevated temperatures, without losing productivity caused by sintering over time. An increase of cycle numbers before the oxygen carrier must be replaced means a substantial cost reduction. A successful optimisation of the iron material leads to increased competitiveness and marketability of the SIP, which is an attractive alternative to other hydrogen production and purification systems.

In order to obtain stable oxygen carriers, five routes of synthesis –namely, co-precipitation, citrate method, dissolution, impregnation and mechanical mixing- were compared, by preparing haematite with 10 wt% of alumina as supporting additive. The obtained oxygen carriers were analysed to evaluate their physical properties like surface area and homogeneity as well as their reactive properties like stability during oxygen exchange process. The final results favoured the oxygen carrier prepared by co-precipitation, which was homogeneous before and after 20 cycles of repeated reduction and oxidation. It provided a stable yield of hydrogen of $29.35\,\mathrm{mg\,g_{OC}}^{-1}$.

After choosing the best route of synthesis the metals cerium, zirconium, and copper were added during synthesis with and without alumina as support. Their effect on stability during hydrogen production and reaction behaviour were evaluated. Results showed that only cerium provided a stable hydrogen yield for 6 cycles. In order to provide a stable hydrogen production 5 wt% of alumina was added. With additional alumina, oxygen carriers containing cerium or copper lead to a fast reduction and high hydrogen yields of $30\,\mathrm{mg\,g_{OC}}^{-1}$.

Kurzfassung

Das Ziel dieser Arbeit ist es, die auf Eisen basierte Kontaktmasse (Oxygen Carrier OC) für den Dampf-Eisen-Prozess (SIP) zu verbessern. Eine der größten Herausforderungen des SIP ist es eine hohe Anzahl an aufeinanderfolgenden Reaktionszyklen, mit jeweils einem Wasserstoff produzierenden Schritt (Oxidation) und einem darauffolgenden Regenerationsschritt (Redutktion), zu erzielen. Hierbei kann es aufgrund der hohen Prozess-Temperaturen zu Versinterung des Materials kommen, was zu einer Verschlechterung der Wasserstoffausbeute führt. Eine Steigerung der Zyklenstabilität und eine damit einhergehende verlängerte Einsatzdauer der Kontaktmasse trägt zur Kostenminimierung bei. Die erfolgreiche Optimierung der Kontaktmasse führt daher zu einer Steigerung der Markt- und Wettbewerbsfähigkeit des SIP, der eine attraktive Alternative zu anderen Wasserstoff Produktions- und Reinigungs-Systemen darstellt.

Für diese Arbeit wurden die fünf Synthesemethoden Co-Fällung, Citrat-Methode, "Dissolution", Imprägnierung und Mechanisches Mischen verglichen, indem Hämatit mit 10 wt% Aluminiumoxid zur Stabilisierung hergestellt wurden. In Folge wurden sowohl deren physikalische Eigenschaften wie Oberflächengröße und Homogenität als auch deren Reaktionseigenschaften wie die Stabilität während des Sauerstoff-Austausch-Prozesses ermittelt. Die besten Ergebnisse wurden mit der durch Co-Fällung hergestellten Kontaktmasse erzielt, die auch nach 20 Zyklen homogen blieb. Dabei wurde eine konstante Wasserstoffausbeute von $29.35\,\mathrm{mg}\,{g_{OC}}^{-1}$ erreicht.

Nachdem die beste Synthesemethode ausgewählt wurde, wurden bei der Synthese die Metalle Cer, Zirkonium und Kupfer sowohl mit als auch ohne Aluminiumoxid als Stabilisator der Eisen-Kontaktmasse zugesetzt, um deren Auswirkungen auf die Stabilität der Wasserstoffproduktion und auf das Reaktionsverhalten zu untersuchen. Als einziges der drei Metalle zeigte Cer eine stabile Wasserstoffausbeute für 6 Zyklen. Um jedoch eine stabile Wasserstoffproduktion zu erreichen wurden 5 wt% Aluminiumoxid der Kontaktmasse beigefügt. Schließlich konnte mit Eisenkontaktmassen die zusäztlich zu dem Aluminiumoxid Cer oder Kupfer enthielten eine schnellere Reduktion und eine höhere Wasserstoffausbeute von $30\,\mathrm{mg}\,{g_{OC}}^{-1}$ erzielt werden.

AFFIDAVIT

Ich erkläre an Eides statt, dass ich die vorliegende Arbeit selbstständig verfasst, andere als die angegebenen Quellen/Hilfsmittel nicht benutzt, und die den benutzten Quellen wörtlich und inhaltlich entnommenen Stellen als solche kenntlich gemacht habe. Das in TUGRAZonline hochgeladene Textdokument ist mit der vorliegenden Masterarbeit identisch.

I declare that I have authored this thesis independently, that I have not used other than the declared sources/resources, and that I have explicitly indicated all material which has been quoted either literally or by content from the sources used. The text document uploaded to TUGRAZonline is identical to the present master‘s thesis.

July, 2016
Date Signature

Acknowledgement

I would like to thank Prof. Viktor Hacker for giving me the opportunity to contribute to the field of renewable energy. His dedication to research made this work possible. I am deeply grateful for his support and inspiration. I also want to express my gratitude to Prof. Matthäus Siebenhofer, who provided, as the head of institute, a friendly and productive environment. My thanks also go to Stephan Nestl and Gernot Voitic, who supported me during my work. I appreciate their help and input. Further I like to thank Bernhard Marius and Michael Lammer, who helped me to operate the analytical devices used for this work. Very special thanks go to Norbert Kienzl and his team at Bionergy 2020+ GmbH as well as Julian Wagner from the Institute of Electron Microscopy and Nanoanalysis, who kindly supported me with their analytical work. I also want to thank the staff of the Institute of Chemical Engeneering and Environmental Technology including Peter Letonja, Herta Luttenberger, Tanja Weiß, Sarah Kunihs and Simon Brandner who helped me when help was needed. Last but not least, I would like to express my thanks to my colleagues at the Fuel Cell group, which made the time I spend on this work a wonderful and enjoyable one I will never forget.

Contents

1 Introduction

Hydrogen has been an important element for chemical industry and the global population for a long time. As main reactant used in the Haber-Bosch process it binds nitrogen from the air to form ammonia. Approximately 121×10^9 kg of ammonia per year is needed in synthetic fertilizers to feed half of the world's population [1]. In addition there are other important fields of application for hydrogen like oil refining, steel industry and methanol production. As much as it plays an important role in the chemical industry, it is also expected to be an essential energy carrier to facilitate energy transition.

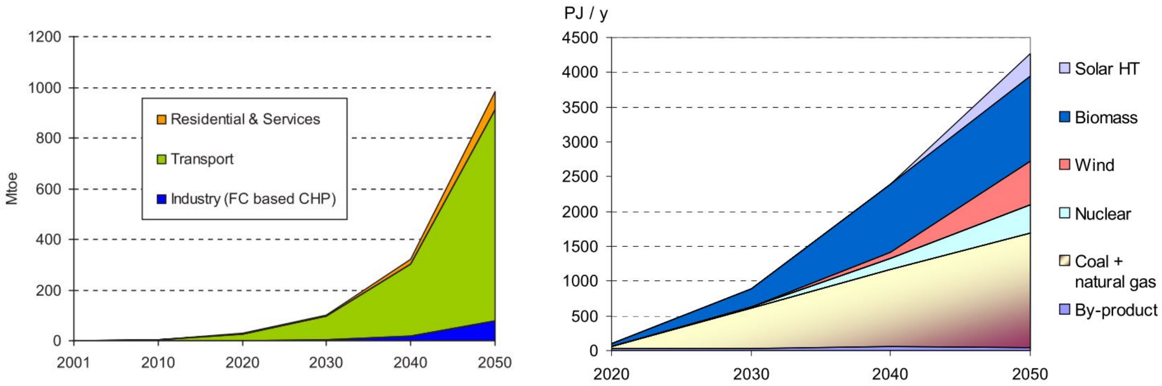

Figure 1.1: Hydrogen outlook of the European Union: (left) Hydrogen production mix according to the "least cost solution" chosen by the stake holders published in HYWAYS [2]. (right) Development of the hydrogen demand according to the H2 Case [3].

Energy transition aims to transform today's energy system into a sustainable one, based on renewable instead of fossil resources. Rising global temperature and signs of climate change have been associated with greenhouse gas (GHG) emissions like carbon dioxide, which can be directly connected to the combustion of fossil fuels [4]. Since the Kyoto Protocol in 1997 efforts have been made by the world community to cut down GHG emissions [5]. Further, a transition will secure energy supply by achieving independence from finite fossil energy sources. In regard to these challenges, the European Union is dedicated to the change in energy sector of its countries. Its vision is a *clean, sustainable, and secured energy system* using renewable sources like wind power, sun energy and biomass. However, those sources are severely dependent on external factors. Therefore seasons, weather and local circumstances amongst other factors must be considered and pose a great challenge to the adaptation of the energy system. High flexibility in the mix of resources is essential to overcome those challenges, but also new ways of energy storage and energy carriers which can be used as transportation fuels are needed.

Hydrogen is a highly promising secondary energy carrier. It can provide long-term storage of energy and is also considered as power to gas solution. Used with fuel cells clean and efficient energy is provided, whereby water is emitted, which is short-lived in the troposphere [6]. Particularly in conurbations it can combat the growing smog problem if used in domestic heating as stationary combined heat and power solution or instead of gasoline for automotive transport. Combined with fast tank refuelling, it takes about 3 minutes, and similar handling to gasoline it is viable for wide and short distance transport. A strong increase of hydrogen demand is predicted by the European Union as Figure 1.1(a) shows. In order to meet the rising demand overall hydrogen production must be increased and adapted to provide a clean alternative fuel. The European Hydrogen Roadmap relies on a mix of primary energy sources for future hydrogen production as seen in Figure 1.1(b).

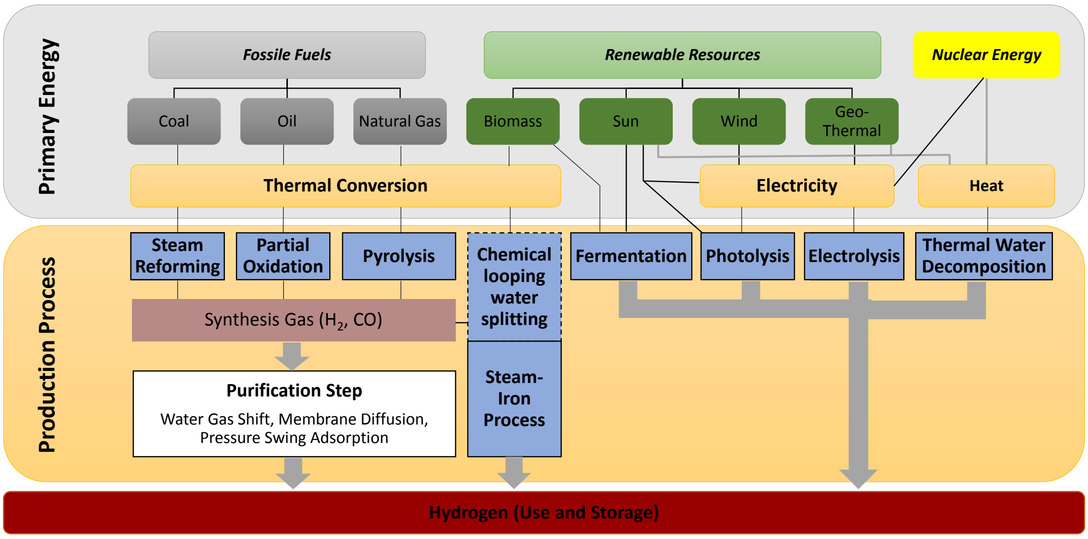

Figure 1.2: Major pathways of hydrogen production.

The main pathways of hydrogen production are listed in Figure1.2. There are several hydrogen production pathways like electrolysis and photolysis that can directly provide clean hydrogen. Yet they are still under development, because of drawbacks like low efficiency and high costs. Nowadays hydrogen is mainly produced by steam reformation of natural gas, which produces synthesis gas at high temperatures. For providing carbon neutral hydrogen, hydrocarbons from biomass like ethanol can be used. Other processes for hydrogen production based on carbon containing matter are partial oxidation, auto-thermal reforming or pyrolysis. Carbon based production often requires multiple cleaning steps to be used in low temperature fuel cells, which increases complexity of the production processes.

The steam-iron process is an long-established production process for hydrogen, which was replaced by natural gas steam reforming because of economic reasons [7]. Already used at the early 20th century on an industrial scale, it has been rediscovered as an alternative way for decentralised hydrogen production [8]. It offers several advantages over other processes, when renewable carbon-sources are used, which are mainly based on its two staged process flow. Iron, which is used as oxygen carrier, generates pure hydrogen from water, while undergoing oxidation. The exhausted metal is regenerated by reduction step, during which the metal oxide is reduced back into its metal form by any reducing gas like synthesis gas. Both reactions are separated in time or space, which provides on one hand pure hydrogen without additional cleaning step and permits on the other hand separate exhaust of polluting gases like CO_2 and CO . Furthermore, an alternating process flow offers the possibility to pressurise the hydrogen during production up to several bars, which facilitates cost reduction and simplifies the process of pressurisation of hydrogen [9].

At the current state of research one main challenge of the process is the oxygen carrier, which must undergo a high number of consecutive hydrogen production and regeneration steps at elevated temperatures, without losing productivity caused by sintering over time. An increase in numbers of reaction cycles before the oxygen carrier must be replaced means a substantial cost reduction by saving material costs and decreasing of downtime for re-filling [7]. This work aims to enhance the iron-based oxygen carrier for the steam-iron process, in order to increase stability as well as to improve reaction behaviour of the alternating hydrogen production and regeneration step.

2 Theoretical Background

2.1 The Steam-Iron Process

The steam-iron process (SIP) is based on the ability of iron to undergo oxidation with steam. Hereby oxygen is bound by the metal and hydrogen is generated. In a recovering step the iron oxide is reduced back into its metallic form using a reducing gas like synthesis gas, which may be provided by steam reforming of methane/higher hydrocarbons, or gasification of biomass. The reactions for this cyclic way of hydrogen production are given in C 2.1 to C 2.3.

haematite $\longleftrightarrow$ magnetite:

$$3\,\mathrm{Fe_2O_3} + \mathrm{H_2}\,/\,\mathrm{CO} \rightleftharpoons 2\,\mathrm{Fe_3O_4} + \mathrm{H_2O}\,/\,\mathrm{CO_2} \tag{C 2.1}$$

magnetite $\longleftrightarrow$ wustite:

$$\mathrm{Fe_3O_4} + \mathrm{H_2}\,/\,\mathrm{CO} \rightleftharpoons 3\,\mathrm{FeO} + \mathrm{H_2O}\,/\,\mathrm{CO_2} \tag{C 2.2}$$

wustite $\longleftrightarrow$ iron:

$$\mathrm{FeO} + \mathrm{H_2}\,/\,\mathrm{CO} \rightleftharpoons \mathrm{Fe} + \mathrm{H_2O}\,/\,\mathrm{CO_2} \tag{C 2.3}$$

In order to provide fast reaction kinetics this process is performed at high temperatures. The reaction of iron depends on temperature and partial pressure of reaction gasses. The Baur-Glaessner diagram describes the theoretical phase transition equilibrium according to the temperature and reducing/oxidising agent ratios of hydrogen to water or carbon monoxide to carbon dioxide. It also shows that the re-oxidation back to haematite, as described in reaction C 2.1, is thermodynamically not possible with steam. Experiments of Beeker et al. proved that 40% water content only leads to 10% conversion [10]. And even concentrations of 5% steam during reduction phase can decelerate the reduction process, which was explained by kinetic influences on the reduction process. Therefore, preferably a low water content must be provided in the reducing gases, which must be considered when syngas derived from renewable resources are used [11].

Nevertheless, SIP is attractive for generating pure hydrogen based on these materials. The process is either performed in a fluidise bed reactor, where the iron-based oxygen carrier is circulated or in a fixed bed reactor where the gas streams are alternated. These systems provide a two-staged process flow, which allows to separate the reduction and oxidation streams either in space or time. When the iron oxide is reduced with gas carrying contaminations they ideally exit the system with the lean gas. Afterwards the re-oxidation is performed with pure steam, which can be subsequently condensed and doing so it can be easily separated from pure hydrogen gas [12]. This is a simple process flow, which opposes other complex purification unit set-ups used for syngas clean-up. In order to maintain a pure hydrogen production, carbon formation during reduction with carbonaceous gases must be avoided by choosing the right reaction conditions [13]. Nestl et al. provided hydrogen from methane without detectable carbon monoxide and only 700 ppm of carbon dioxide [9]. Therefore, the hydrogen can be directly used for high temperature PEM fuel cells. Hacker et al. studied the effects of additional pollutants hydrogen sulphide and hydrogen chlorides, which are typical for synthesis gas produced from biomass [11]. The recovered hydrogen only contained $H_2S < 1$ ppm and HCl < 4 ppm. They found out that a great extant was solved and condensed in the water stream leaving the test plant.

2.2 Reaction Mechanisms

The reduction and oxidation reactions of the SIP are gas-solid reactions. Their reaction kinetics are primarily dictated by diffusion mechanisms, as described by Oeters et al. and shown in Fig. 2.1 [14]. Each mechanism can be rate-limiting depending on the conditions of the reaction e.g. temperature, gas flow, gas concentration, size and structure of oxygen carrier.

2.2.1 The Gas-Solid Reaction

Oeters' model states that mass transport of the reaction gas takes place from the gas stream into the outer gas layer, which is placed around the particle [14]. After passing this layer, molecules are driven further into the porous structure. At first through macro pores, where porosity and tortuosity of the particle directly influence the diffusion coefficient. If the pore diameter is smaller than the mean free path of the gas molecules, the pores are defined, according to this model, as micro pores. In this scale 'Knudsen diffusion' takes place, where gas molecules are more likely to hit the walls of the particle than to collide with other gas molecules. As a result of wall collision the hydrogen adsorbs at the surface of the solid iron oxide, where the interface reaction takes place. The resulting product gas diffuses out in the

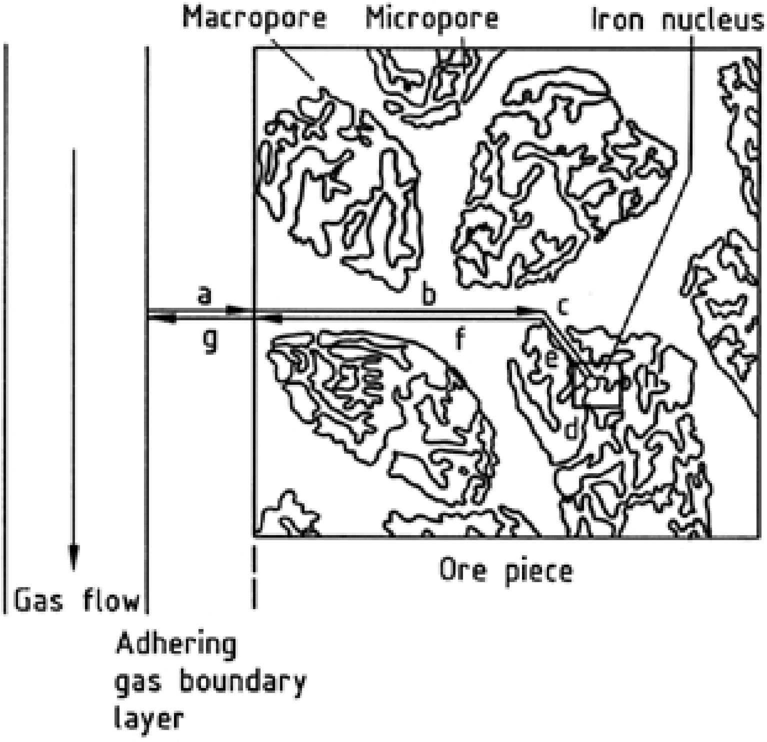

Figure 2.1: Illustration of the reduction mechanism in porous iron ore particles. (a) Diffusion through the Outer Gas Boundary, Diffusion through the macro- (b) and micropores (c), (d) Interfacial reaction, (e + f) Back-Diffusion of the product gas through the micro- and macropores, (g) Back-Diffusion of the product gas through the Outer Gas Boundary Layer [14].

reversed diffusion mechanism as described before in Figure 2.1 (e-g). In highly porous iron the removal of water is slow hindering the reduction process, while in sintered iron the solid-state reaction poses the rate-limiting reaction [15].

2.2.2 The Reduction Process

When haematite is reduced a layer of magnetite starts to form at the surface, which inhibits the direct reduction of the haematite phase. As a consequence of this barrier a flow of Fe^{2+} and $2\,e^-$ from gas-surface reaction zone to the magnetite-haematite interface, which is positioned inside of the particle, starts to control the reaction. At the interface, iron ions transform the haematite to magnetite, which leads to a continuous inwards shift of the magnetite-haematite interface. The transition of magnetite to wustite follows the same reaction mechanism. The haematite transition, however, is particularly prone to create failures in the lattice structure [15]. During reduction of wustite iron metal is formed, which can precipitate in the wustite phase or at the surface. At the surface an iron metal may build a layer, which further slows down the reduction process.

2.2.3 The Oxidation Process

The general mechanism for steam-oxidation is described in literature as an interaction of the water vapour with the iron (oxide) surface [16, 17]. There are two reaction mechanisms discussed for iron oxidation with steam. The reaction mechanisms are given in equations C 2.4-C 2.6. After adsorption the water molecule can split into atomic (H') hydrogen and an hydro-oxygen (OH', which then further separates into hydrogen and oxygen ions. While hydrogen ions combine and diffuse back to the gas diffusion barrier, the oxygen ion travels through lattice vacancies to its reaction site. Other sources report that the mechanism for steam is possibly governed by the formation and lattice diffusion of an hydroxyl ion, after water adsorption [18]. Overall oxygen/oxygen hydroxide conductivity are an important rate determining reaction mechanism [19].

$$\mathrm{H_2O\,(g)} \longleftrightarrow \mathrm{H_2O\,(ads)} \tag{C 2.4}$$

$$\mathrm{H_2O\,(ads)} \longleftrightarrow \mathrm{O_O} + \mathrm{V_{Fe}^{''}} + \mathrm{H_2} + 2\,\mathrm{h} \tag{C 2.5}$$

$$\mathrm{H_2O\,(ads)} \longleftrightarrow \mathrm{OH_O^{'}} + \mathrm{H_i^{'}} \tag{C 2.6}$$

The oxidation process induced by steam is confirmed by Yuan et al. as a two-staged reaction process in the temperature range of 600°C to 750°C . At start reaction kinetics are linear and fast. This kinetic changes after a certain amount of time to a parabolic reaction kinetic which indicates a change in the rate-determing reaction step due to reaching a local equilibrium at the surface.

- **First stage:** surface-gas reaction is the rate limiting reaction step. At the beginning the diffusion of hydroxyl ions through the freshly formed oxide layer is considered to be faster.
- **Second stage:** Is rate-determined by the diffusion process of the hydroxyl ions. It is considered that longer pathways cause a slower reaction.

2.3 Deactivation Processes

Deactivation is any process that results in decreasing of the oxygen conversion capability of iron-based oxygen carriers during cyclic use. Common deactivation processes are fouling, solid-solid reaction, vapour formation and sintering.

2.3.1 Coke Formation

Coke Formation is relevant for applications where carbon oxides are contained in the reduction gas. As there is a sensitive balance between the gas phase and the solid carbon phase, carbon can deposit on the surface and in pores of the oxygen carrier. This carbon deposition prevents contact between iron and reaction gases and must be avoided by careful adjustment of the reaction parameters. A common way to depose the solid carbon is oxidation with oxygen/air, which will also oxidise magnetite to haematite.

2.3.2 Solid-Solid Reaction

Metals which are added for promoting and supporting the iron can react and form new phases with none or decreased oxygen exchange capability. Hercynite is a compound, which is known for this inactivation of the iron-based oxygen carrier [20].

2.3.3 Vapour Formation

Vapour formation plays a minor role in the steam-iron process. However, when a metal is used which forms volatile compounds with the gas phase, it may result in loss of the metal. This can effect the oxygen exchange capability by removing the promotor/support.

2.3.4 Sintering

Sintering is the most crucial deactivation process for iron, caused by the high temperatures used for the working conditions of the steam iron process. It is a mainly an irreversible process resulting in the loss of active surface area. In consequence, solid state diffusion becomes the rate limiting reaction step at an early phase of reaction, which will slow down oxygen exchange processes.

In terms of thermodynamics, sintering, is the result of a system lowering its free surface energy by reducing its surface while forming a denser material. This process is governed by material transport which needs high activation temperatures that must be higher than 0.5 times the melting temperature of a material. These temperatures are referred to as Tammann-temperatures [21]. For iron and its oxides Tammann-temperatures can be found in table 2.1.

Table 2.1: List of Tammann-temperatures for different metals and several oxidation states, based on the melting points taken from [22].

metal species	melting point / °C	Tammann temperature / °C
haematite	1565	782,5
magnetite	1538	769
wustite	1369	684,5
iron	1538	769
aluminium(III) oxide	2045	1022.5
cerium(II) oxide	2600	1300
zirconium(II)oxide	2700	1350
copper(II)oxide	1326	663
copper	1083	541,5

Those transport mechanisms lead to neck growth at the contact areas between particles. As a result of this, particle boundaries continuously decrease. The main transport mechanisms are shown in Fig 2.2(a) [23, 24]. Generally neck growth takes place by material transport, either through the lattice, across the surface, or from the grain boundaries. Diffusion to lattice vacancies at the contact zones are more important, while evaporation/condensation and viscous flow play a minor role for solid phase sintering. A particularity for the iron-based oxygen carrier, which undergoes repeated oxidation and reduction, is the permanent shrinkage and swelling. This size changes are also the result of material transport which promote particle coalescence. Figure 2.2(b) shows the general model of sintering, which progresses in 3 stages [24].

- **Initial stage:** Adjacent particles start to build bridges in order to reduce lattice defects and tensions.
- **Intermediate stage:** Necks continue to grow and cristall growth starts, which results in loss of porosity and increasing of the material density. The open pore structure changes to a closed one.
- **Final stage:** The crystallites start to heal out remaining pores and grow to a maximum size, which is influenced by impurities.

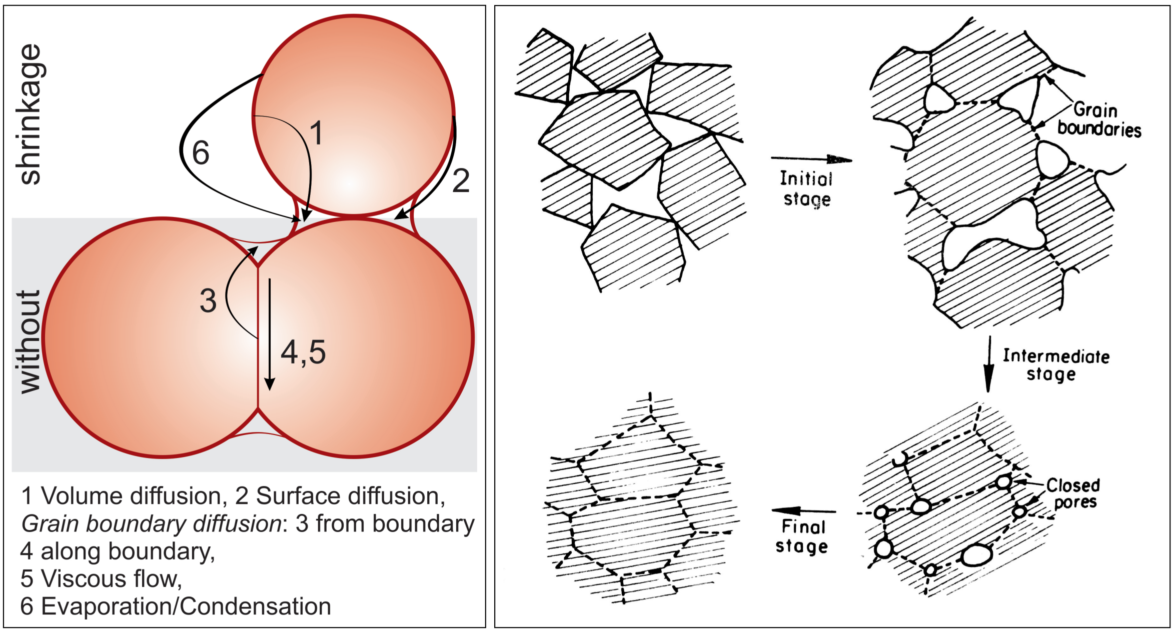

(a) Mechansims of mass transport. An adaptation based on [23].

(b) Three stages of sintering [24].

Figure 2.2: Schematic illustration of the sintering process.

2.4 The Oxygen Carrier

2.4.1 Iron as Oxygen Carrier

Iron has several advantages as oxygen carrier material. It possesses a high availability (4.7 wt% of the Earth's crust), a low price and low health and environmental risks in its application [14]. However, it is not stable during cyclic use at the high temperatures needed for high reaction rates. It shows degradation by sintering and only allows a limited amount of redox cycles. For increasing the number of cycles and hence the amount of produced hydrogen per unit-filling, stabilisation of the oxygen carrier is needed.

2.4.2 Alternative Metals as Oxygen Carrier

With the poor sintering behaviour in mind the use of an alternative metal system might be considered. In order to evaluate better metal systems Markus Thaler examined metals as suitable alternative materials for the SIP [25]. Using thermodynamic studies he excluded inert metals which are not oxidised by steam like gold, copper and nickel, but also metals with opposite behaviour were investigated. Those metals with exceedingly high affinity to oxygen are not reduced by hydrogen or carbon monoxide up to 1300 °C like MgO, ZrO_2, and Al_2O_3.

With the support of thermodynamic experiments, he narrowed suited metals for the SIP down to molybdenum, tungsten and iron. He overall suggested tungsten as good alternative metal. In literature, however, it can be found that tungsten can form volatile hydroxide and hydrate compounds with water vapour at high temperatures [26, 27]. Therefore, a change of the main oxygen carrier to tungsten can pose new challenges. Fan et al. generally concluded that only iron is suitable for the hydrogen production due to the lack of reactivity of other metals within the temperature range used for the metal oxidation with steam [7]. Hence, a optimisation of iron-based oxygen carrier is the main focus of general research.

2.4.3 Additve Metals

In order to stabilise and improve kinetics during hydrogen production at high temperature the addition of other metals can either give support and/or enhance the reactivity of the oxygen carrier.

Often different metal ferrites with the form of $\mathrm{Me_xFe_{3-x}O_4}$ (e.g. Me= Ce, Cr, Al, Zr) are reported to prevent sintering, by building layers on the particle surface [28]. These are assumed to function as a thermochemical stable barrier between iron grains that reduce the probability of sintering neck formation and hence, prevent sintering [21, 29].

Many metals have been reported to minimize the deactivation process by sintering. Especially alumina received large attention for this purpose [30, 31]. However, it can reduce reactivity of the iron-based oxygen carrier [20]. Other metal oxides that were found to have a positive effect on the stabilisation of the iron-based oxygen carrier are $\mathrm{CeO_2}, \mathrm{ZrO_2}$ and $\mathrm{TiO_2}$ [21, 29, 32, 33].

Otsuka et al. proposed several effects on the iron-based oxygen carrier other metal oxides can have to promote reduction/oxidation [34]. They suggested that the formation of a new metal species is generally involved. It either can precipitate at the surface or inside the iron-based oxygen particle. If the compound forms on the surface it can participate into the water/hydrogen splitting. Or, if it is driven further into the iron lattice during succeeding red-ox reactions it may promote the breakage of Fe-O bonds.

Often platinum-group metals (Pd, Pt, Rh, Rd, Cu) are found to accelerate the reduction process and decrease reaction temperatures, because they catalyse hydrogen splitting [32, 35]. Other metals can have a more direct influence on the iron lattice. Cerium oxide has been reported to facilitate the oxygen-diffusion during reduction as well as oxidation by forming vacancies in the iron lattice, while building $\mathrm{CeFeO_3}$ [19, 36, 37].

The oxidation process can also be positively influenced by molybdenum or zirconium, which already showed a positive influence at even low concentrations of 0.23 mol%, if applied on the surface [35].

2.5 Preparation Methods in the Field of the Steam-Iron Process

It is a challenge to prepare the ideal iron-based oxygen carrier for the SIR process, since it has to meet several important criteria. The main properties, which affect the performance, can be listed as follows:

- thermal and mechanical stability
- high stability of oxygen conversion/hydrogen production
- high reactivity during the oxygen exchange reaction
- high surface area
- good porosity to promote reaction and product gas exchange
- low cost and long cycle life
- environmental and health safety

The addition of additive metals take influence on the properties described above. However, the effect of the proper choice of the route of synthesis may not be underestimated. The way of synthesis can have a major influence on the properties, like surface area, porosity and costs of the oxygen carrier (e.g. precursors, energy input, preparation time, post-preparation steps) [38]. Especially when foreign metals are added to the iron-based oxygen carrier, homogeneity in their distribution can have an effect on the oxygen carrier, as discussed in this work.

In the research field of the SIR process and the related chemical looping combustion several methods to prepare iron-based oxygen carriers are used. In many cases the oxygen carrier is prepared on a macroscopic level by combining metal oxide powders, which are shaped to spheres, pellets or rods during the process. In general methods like mechanical mixing, extrudation and freeze granulation are used for this kind of preparation [39–42]. In general they are easy and cheap methods to intermix metal oxides. Basic materials are metal oxide powders, which are mechanically mixed in desired ratios. The procedure can vary by either mixing the powders dry, with or without binder, or wet including a drying step. Due to the macroscopic level of mixing, the resulting carrier is less homogeneous than by routes of synthesis using metal salts.

Another frequently used method is the impregnation of metal oxide particles with solutions of metal salts like nitrates and acetates [43]. Impregnation is a well-established method for the preparation of supported heterogeneous catalysts. It is technically easy and cheap. During impregnation metal salts are deposited from a solution on a porous solid. As for most catalyst-applications only low amounts of the precious metal are needed, the ratio of precious metal to support may be low. For the SIP, however, the highest possible amount of oxygen carrier must be reached by the preparation method. High loadings of active oxygen carrier would require several impregnation steps resulting in a complicated and more expensive oxygen carrier preparation method. Therefore, Bohn et al. introduced the term of "wet-impregnation with back addition", where the metal support is impregnated on the metal oxygen carrier [44].

In contrast to the methods above wet chemical preparation methods provide the possibility to obtain materials with better homogeneity on a molecular level. They can give a better control on particle size and porosity, but have the disadvantage that they are more complex [45]. Typical wet-chemical procedures are precipitation methods like dissolution and co-precipitation. They are distinguished by their sequence of metal salt addition to the precipitation agent [7]. During co-precipitation metal salts, which are dissolved in water, are added to the the precipitation agent (like NaOH, Na_2CO_2, ammonia or alcohol), while the dissolution allows the direct *dissolution* of the metal salts in the precipitation agent. "By this method, 2-propanol, water, and nitric acid in the solution can be evaporated off at different stages, thereby offering production of fine and porous powder [46]."

Another method which is often used for the preparation of oxygen carriers is the citrate method. It has the particular advantages, opposing to other precipitation methods, that it posses a high tolerance to many different kinds of metal compositions. This results from an amorphous precursor, which is formed by the metal salts and citric acid in a combined heat treatment and evaporation step. A final eruptive decomposition step leads to a porous solid caused by gas evolution [47].

Sol-gel methods are offering the best control during the preparation of solid particles [30, 31]. They are based on the condensation of metal hydroxides in order to form polymer-like structures, where many parameters like concentration and kind of precursor, temperature, solvent or water content can be controlled and have an influence on the characteristics of formed solid products [48]. The complexity of this method precludes a good knowledge and high experience of this method.

2.6 Thermogravimetric Analysis

The performance of oxygen carriers during the alternating hydrogen production and regeneration process can be evaluated by thermo-gravimetric analysis. During an isothermal measurement the weight changes over a measured time according to the reactive atmosphere, which is either reducing or oxidising. This weight change reflects the amount of oxygen, which is either removed or added during the segments of the measurement. The exchanged number of oxygen is directly relatable to elemental hydrogen consumption/production of each reaction, as it is described in reaction C 2.2 and C 2.3. If the mass difference between the reduced state of a cycle ($w_{Red,n}$) and the oxidised state ($w_{Ox,n}$) is compared, a judgement over the stability of hydrogen yield of an oxygen carrier can be made. While the mass difference gives information on the hydrogen yield the curve progression gives information on changes in reaction kinetics. If the oxygen carrier changes for example by sintering at the surface, the reaction becomes limited by the slower solid-solid diffusion. The curve of the thermo-gravimetric measurement reflects this deceleration by a decreasing slope .

3 Experimental

3.1 Sample Preparation

3.1.1 List of Chemicals

1. Iron(III)nitrate nonahydrate, (Alfa Aesar; purity > 98 %; metals basis)
2. Aluminum(III)nitrate nonahydrate, (Sigma Aldrich; purity > 98 %; ACS reagent)
3. Cerium(III) nitrate hexahydrate, (Alfa Aesar; purity 99.5 %; REacton®)
4. Copper(II) nitrate trihydrate, (Sigma Aldrich; purity 98 %)
5. Zirconium(IV) oxynitrate hydrate, (Sigma Aldrich; purity 99 %)
6. Sodium Carbonate, (Merck; purity 99.5 %)
7. Citric acid (Sigma Aldrich, anhydrous; purity > 99.5 %, ACS reagent)
8. 2-Propanol (Carl Roth; purity > 99.9 %; ROTISOLV®)
9. Iron sponge (Alfa Aesar; purity 99.9 %; -100 mesh; metals basis)

All materials were used as purchased and without any special treatment except zirconium(IV) oxynitrate hydrate. This salt did not easily dissolve in water like all other nitrates. Therefore, the zirconium(IV) oxynitrate hydrate powder (13.4 wt%) was boiled in distilled water with an excess of nitric acid (12.3 wt%). The obtained clear and colourless solution was consecutively hot filtrated through a glass frit (100 °C) and finally stored in a Schott Duran® bottle.

3.1.2 Co-Precipitation

A continuous precipitation method described by P. Kidambi et al. was used for the preparation of oxygen carriers named **Pre**, **Fe-Ce**, **Fe-Al-Ce**, **Fe-Zr**, **Fe-Al-Zr**, **Fe-Cu** and **Fe-Al-Cu** (16 h and 3 h) [20]. For each synthesis two solutions were prepared. The first solution was a metal nitrate solution containing the required metals with the overall metal ion concentration of $1\,\mathrm{mol\,l^{-1}}$ in H_2O. The second solution was used as precipitation agent which contained $1\,\mathrm{mol\,l^{-1}}$ Na_2CO_3 in H_2O. A 3-necked flask was attached with a pH-meter and two dropping funnels. The metal nitrate solution and the precipitation agent were added simultaneously to the flask. While the nitrate flow ($\sim 1.5\,\mathrm{ml\,min^{-1}}$) was constant the Na_2CO_3 flow was adjusted manually in order to keep the pH value at 7.8 ± 0.5. A magnetic stirrer was used for agitation during precipitation ($\sim$ 600 rpm) and the following ageing process (1 h; 800 rpm).

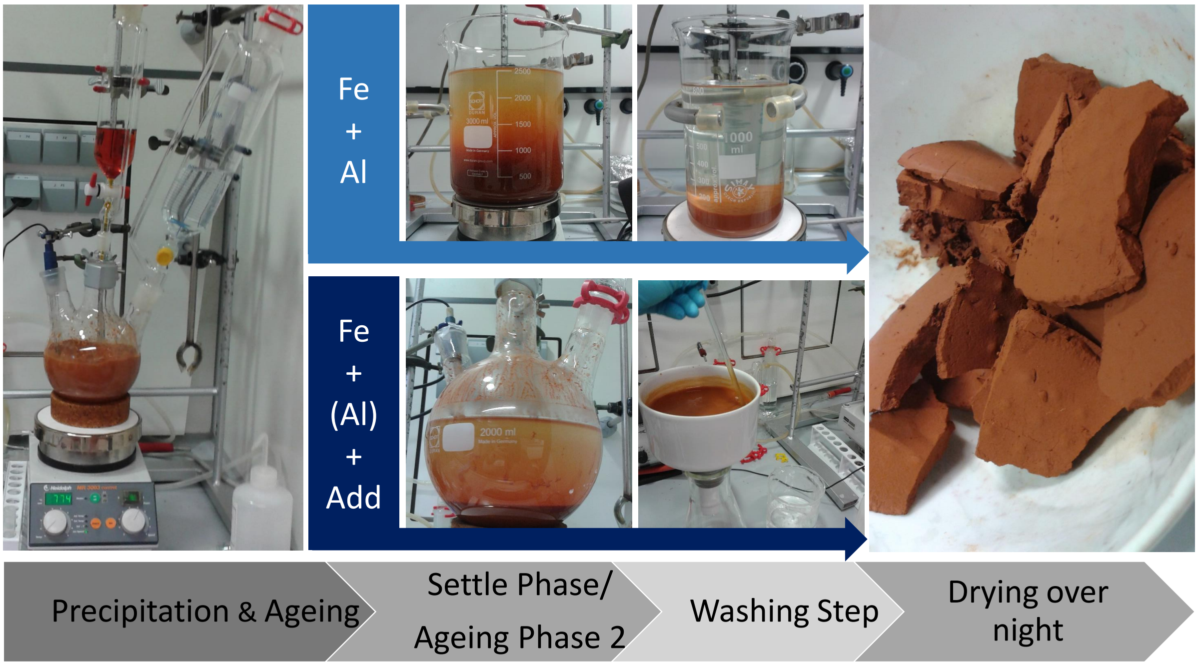

Figure 3.1: Overview diagram of Co-Precipitation.

The suspension of oxygen carrier Pre was allowed to settle for 50 minutes. Afterwards the supernatant liquid was discarded and the precipitate was washed with reverse osmosis water (30 times the volume of the precipitation). Several washing steps followed, which were altered between settling the precipitate and adding water until the conductivity of the supernatant liquid was < 40 µS. Eventually the precipitate was filtrated. In contrast to oxygen carrier Pre, the other oxygen carriers were washed with a faster method. After the same agitated ageing step of one hour, the suspension was aged without stirring for 50 minutes, in order to reproduce the settling phase in the concentrated precipitation-solution. Then the suspension was filtrated and subsequently washed with reverse osmosis water (about 10 times the volume of the precipitation) until the conductivity of the filtrate was < 40 µS. Finally the filter cake of both washing methods was dried overnight in air at 110 °C. The final product resembled dark brown clay fragments, which were roughly crushed with an agate mortar and pestle. The sample was calcinated at 900 °C in air for 3 h to decompose the precipitation products and to form metal oxides. The final product was crushed and sieved to a grain diameter of 90-125 µm.

3.1.3 Citrate Method

A comparably fast procedure of the citrate method was chosen using a rotary evaporator. Therefore, methods used by J. Kirchnerova et al. and E. Lorente et al. were merged for the preparation of oxygen carrier named **Cit** [49, 50]. A solution of $Fe(NO_3)_3 \cdot 9\,H_2O$ and $Al(NO_3)_3 \cdot 9\,H_2O$ was prepared (100 ml; 1 $mol\,l^{-1}$) and put in a single necked flask. The citric acid solution (50 ml; 2 $mol\,l^{-1}$) was added, while the metal nitrate solution was stirred with a magnetic stirrer. The mixture of ctirc acid metal nitrates was stirred for 10 minutes at room temperature. Afterwards a rotary evaporator (80 °C; 150 mbar; Hei-VAP Advantage Rotary Evaporator) was used to remove water until a viscous liquid was formed, which turned into gel after cooling to room temperature. The gel, which was kept in the flask, was dried at 110 °C overnight. After this drying step a bristle, highly porous solid was obtained, which was easily crushed with a pestle before undergoing calcination at 900 °C in air for 3 h.

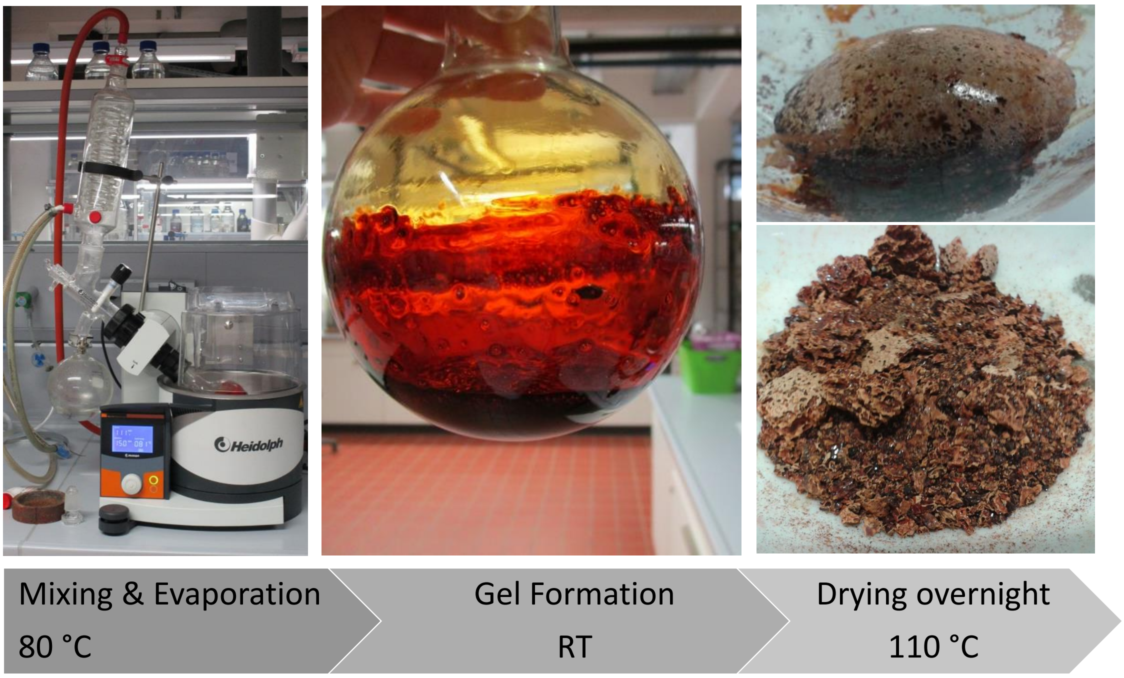

Figure 3.2: Overview diagram of Citrate Method.

3.1.4 Dissolution

Ishida et al. described this method [46, 51–53]. For preparing oxygen carrier named **Dis**, a mixture of 2-propanol and water (300 ml; 3:1 vol%) was prepared and filled in a 3-necked flask attached with a gas in- and outlet and a thermometer. For agitation a magnetic stirrer was used. The $FeNO_3 \cdot 9\,H_2O$ (22.77 g) and $Al(NO_3)_3 \cdot 9\,H_2O$ (3.68 g) were dissolved in the solution and stirred at room temperature for 1 h. A silicon bath was heated up to 100 °C while the mixture was under gentle air purge, which helped to exhaust water and propanol vapour as well as nitrous gases in a controlled way. The temperature was held until the sample was roughly dried (24 h). The powder, which contained spherical agglomerates, was transferred to a crucible and was initially dried at 150 °C (24 h) and afterwards at 200 °C (5 h) to remove and decompose nitrates and the remaining alcohol. At last the sample was calcined at 900 °C for 3 h in air and fractionated by crushing in an agate mortar and sieving to a grain size of 90 - 125 µm.

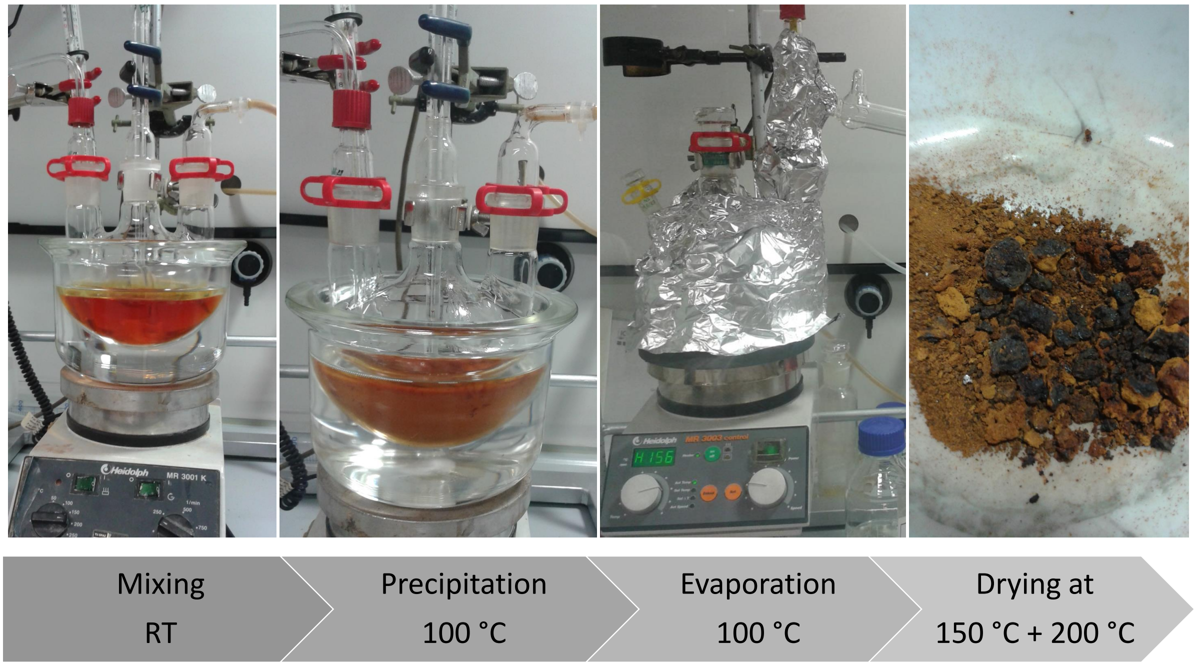

Figure 3.3: Overview diagram of Dissolution.

3.1.5 Impregnation

The procedure was done by wet impregnation with "back-addition" of the support material based on a method described by C. Bohn et al. [44]. As active support material porous iron sponge was chosen, which was impregnated with $Al(NO_3)_3 \cdot 9\,H_2O$ to obtain a high amount of oxygen carrier within one impregnation step. For oxygen carrier named **Imp** a solution of $Al(NO_3)_3 \cdot 9\,H_2O$ was prepared (250 ml; $0.05\,mol\,l^{-1}$; in H_2O) and transferred into a 4-necked flask, which was attached with a gas in- and outlet, a KPG-stirrer and a thermometer. The KPG-stirrer was chosen due to the magnetic properties of the iron sponge. Under permanent stirring the fractionated iron sponge powder (4.01 g; 90 – 125 µm) was slowly added to the prepared solution. A gentle air purge was set to assist the transport of steam and nitrous gases, while the mixture was heated and kept at 80 °C until a light brown powder was formed. The prepared oxygen carrier was heat treated at 900 °C for 3 h in air to decompose the nitrate and form the metal oxides. Finally the powder was crushed in an agate mortar and sieved to obtain a grain size of 90 - 125 µm.

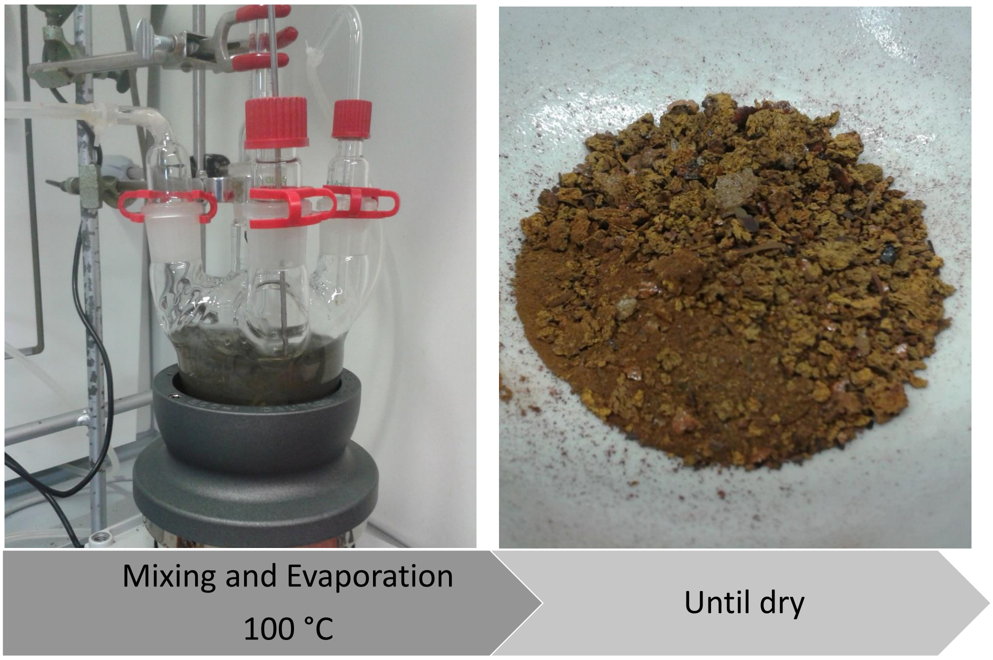

Figure 3.4: Overview diagram of Impregnation.

3.1.6 Mechanical Mixing

In this thesis, samples prepared using mechanical mixing served as reference material. Those materials are oxygen carrier named **MM** with 90 wt% of Fe_2O_3 and 10 wt% of Al_2O_3 and oxygen carrier **Fe-Al-Cu (mixed)** with 90 wt% Fe_2O_3, 5 wt% Al_2O_3 and 5 wt% CuO, which were prepared by S. Nestl and G. Voitic in previous experiments [9, 13]. During preparation an intensive mixer (Maschinenfabrik Gustav Eirich GmbH & Co KG) was used to create a homogeneous powder blend of haematite (Alfa Aesar; purity 98%; -325 mesh), $\alpha - Al_2O_3$ (Alfa Aesar; purity 99.9%; 20-50 µm) and optionally of CuO (Alfa Aesar; purity 97%; -325 mesh) . Before finishing the mixing process, deionized water was added to agglomerate the particles. To provide the same conditions for the reference material as for the samples that were synthesized for this work the agglomerates were roughly crushed, calcined (900 °C, 3h) and finally fractionated to a grain size diameter of 90-125 µm by sieving and grinding.

3.2 Characterisation

3.2.1 Thermogravimetric Analysis

Instrumental Set-Up

For thermo-gravimetric analysis (TGA) a STA 449 C Jupiter (NETZSCH) was used. It was equipped with a steam generator (aDROP Feuchtemeßtechnik GmbH), which vaporized water at 200 °C. In order to transport the provided amount of steam to the furnace chamber a transfer line was used. The furnace featured a heating collar and a heated gas outlet, which were located at the bottom of the furnace to prevent condensation of steam. If needed the furnace chamber was evacuated with a vacuum pump-system. For the gas feed a mass flow controller (NETZSCH) was used, which provided the thermo-microbalance with nitrogen and hydrogen gases. For measurements a TG-sample carrier system without radiation shield was used. As measuring head "slip-on plates" made of aluminium oxide ($\sim$ 1.6 g) were chosen. A setup of the measuring equipment is shown in figure 3.5.

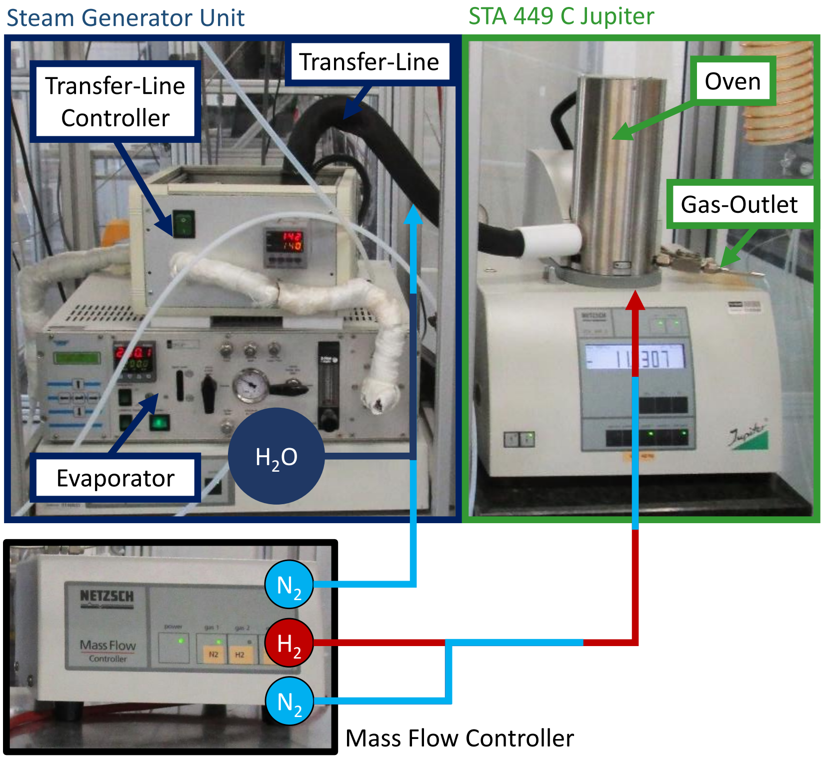

Figure 3.5: Scheme of the thermo-gravimetric analysis set-up.

Sample Preparation and Measurement

In advance of measurements each sample was dried at 110 °C over night because all oxygen carriers were stored for a couple of weeks before analysis. In the case of the oxygen carrier which was prepared by the citrate method, a problem with the heating furnace prevented a complete removal of water as can be seen in the segments of the heating process shown in diagram 4.14(b).

Table 3.1: Programming of the TG-measurement: 20 cycles of reduction and oxidation at 800 °C.

segment	process	T [°C]	t [min^{-1}]	N_2 [ml min^{-1}]	H_2 [ml min^{-1}]	H_2O [g min^{-1}]
-	preheating	-	~40	50	-	-
0	start	90	-	50	-	-
1	heating	750	44	50	-	-
2	heating	780	3	50	-	-
3	heating	800	5	50	-	-
4	stabilisation	800	10	50	-	-
5	reduction	800	20	50	60	-
6	purge	800	5	50	-	-
7	oxidation	800	20	50	-	0.0633
8	purge	800	5	50	-	-
9-83			segments 5-8 are repeated			
84	final purge	800	60	50	-	-
85	cool-down	100	47	50	-	-

Exactly 100 ± 1 mg of the oxygen carrier was weighted out on a slip-on plate using an analytical balance. The powder was flattened and spread with a spatula. Then the measuring head was put on the sample carrier. After all gas valves had been opened and the gas flow had been controlled, the furnace chamber was evacuated and filled with nitrogen gas three times to provide an inert atmosphere to protect the apparatus. In following preheating phase, all auxiliary heaters (transfer line, vaporizer adapter, heating collar, gas outlet) were switched on in order to heat up to set temperatures. When the thermocouple unit showed a temperature of 90 °C, the weight value was zeroed and the measurement was started. The programming of the measurement is described in table 3.1. Since different reactive gases were used a purge segment of 5 minutes with nitrogen followed each reduction and oxidation step. The purpose of this was to remove the reactive gases out of the furnace chamber. However, this also provided segments for evaluation taken in the same atmosphere, which eliminated uplift effects caused by different gas densities. After a completed measurement the oxidised sample was photographed and stored for further analysis.

Calculations

To easily compare the prepared oxygen carriers in this work, which slightly differed in their iron - aluminium composition, the term of oxygen exchange" was defined. The oxidation of the iron with water vapour only reaches the magnetite level. Following this, the magnetite level was defined as maximal theoretical oxygen exchange ($\Delta w_m ax, th$), which was calculated based on the analytically determined iron content of each oxygen carrier as seen in Equation 3.1.

$$\Delta w_{max,th} = w_{Fe_3O_4,th} - w_{Fe,th} \tag{3.1}$$

To obtain the oxygen exchange of the TGA-measurement the difference between the median of the purge phase after each reduction w_{red} and the median of the values of the purge phase after each oxidation w_{ox} of the cycle n were devided by the maximal theoretical oxygen exchange as shown in Equation 3.2.

$$OxygenExchange = \frac{\Delta w_{ox,n} - \Delta w_{red,n}}{\Delta w_{max,th}} * 100\% \tag{3.2}$$

The purge phase after each reaction was chosen as basis of calculation to avoid biased weights by dilution effects resulting from the different reaction gases [54].

3.2.2 Mercury Intrusion Porosimetry

Instrumental Set-up

Pascal Series mercury intrusion porosimeter modules 140 and 440 (Thermo Finnigan Italia S.p.A.) were used for analysis. For specifications of the modules see table 3.2. Since powders of 90-125 µm were measured a dilatometer of the series CD3P (POROTEC) combinde with a notch for powders was used. The mercury had a purity of 99.995%.

Table 3.2: Specifications of the modules Pascal 140 and Pascal 440 for mercury intrusion porosimetray [55].

	Pascal 140	**Pascal 440**
Functions	degassing mercury filling low pressure porosimetry	high pressure porosimetry
Measuring range	0.01 to 0.1 kPa 0.1 to 400 Kpa	0.1 to 400 MPa
Pore size range	116 - 3.8 µm	15 - 0.0036 µm
Accuracy	> 0.25%	> 0.2%
Pressure mode	continuous	pressure equilibrium

Sample Preparation and Measurement

Before analysis the sample material was dried at 110 °C over night. An amount of 250 ± 10 mg was weighted into the dilatometer, which was subsequently evacuated in the Pascal 140 for 15 minutes to degas the sample. Eventually the dilatometer and its reference notch were filled with mercury and low pressure measurement (0.1 to 400 kPa) was started. After the measurement was finished it either was repeated with the function provided for this purpose (samples: Fe-Ce, Fe-Al-Ce) or it was already transferred to the oil-containing autoclave of the Pascal 440 (samples: MM, Imp, Pre, Cit, Dis). In Pascal 440 the remaining space of the reference notch and thereafter the autoclave were filled with hydraulic oil. The measurement was performed in the pressure range of 0.1 to 400 MPa.

Calculations

The calculations were executed in the evaluation software MilesW 1.0.2.1 by ThermoFinnigan. The obtained values were calculated by following equations [56]. The pore diameter d can be derived from the Washburn equation (see equation 3.3), which takes into account that mercury is a non wetting liquid and needs a certain pressure to intrude into a pore of a certain diameter. It shows that the pore diameter is indirectly proportional to the pressure which must be applied for mercury intrusion.

$$pd = -4\gamma cos(\theta) \tag{3.3}$$

With θ as surface tension of mercury, γ as wetting angle and p as applied absolute pressure.

Assuming that all pores have a cylindrical shape, 480 dyn cm^{-1} is used for the surface tension of mercury and the contact angle between the mercury and the sample is 141,3° following equation is obtained from equation 3.3.

$$d = \frac{2 \cdot 7500}{p}\ [nm] \tag{3.4}$$

The porosity was calculated according to equation 3.5 by the total pore volume V_{pores}, sample volume V_{sample} and the sample mass w_{sample}.

$$Porosity\ [\%] = \frac{100 \cdot V_{pores} \cdot w_{sample}}{V_{sample}} \tag{3.5}$$

The total specific surface area A_i was calculated by the cylindrical pore model as described in equation 3.6. It assumes that all pores possess a cylindrical shape, which is defined by the pore diameter d_i and its corresponding intrusion volume V_i.

$$A_i \; [m^2 \; g^{-1}] = \frac{V_i}{d_i \cdot w_{sample}} \tag{3.6}$$

The bulk density ρ_{sample} represents the density which is directly related to the sample volume, which includes the pore volume. It can be directly related to the blank-corrected volume of mercury $V_{Hg,blank\ cor}$ which is displaced by the sample of a certain weight w_{sample} in a vacuum atmosphere.The bulk density was calculated according to equation 3.7.

$$\rho_{sample} \; [g \; cm^{-3}] = \frac{V_{Hg,blank\ cor}}{w_{sample}} \tag{3.7}$$

The apparent density ρ_{app} relates to an approximation to the real volume the solid sample occupies excluding the pore volume. It is, however, limited to the maximal pressure of the measurement and discriminates pores, which are too small for the analysis method.

$$\rho_{app} \; [g \; cm^{-3}] = \frac{V_{sample} - V_{pores} \cdot w_{sample}}{w_{sample}} \tag{3.8}$$

3.2.3 Scanning Electron Microscopy

All pictures were taken by J. Wagner on a Zeiss Ultra 55 at the Graz Center for Electron Microscopy. Oxygen carrier powders were applied on metal specimen holder, which were prepared with an adhesive tape. For further fixation and minimizing of charging effects the sample powders were coated with $\sim$ 60 nm of carbon.

3.2.4 Elementary Analysis

Elementary analysis was carried out by N. Kienzl and his team at Bioenergy 2020+ GmbH using ICPOES (Spectro Arcos SOP) with external calibration. In order to solve the metal oxide samples microwave assisted acid digestion under elevated pressure was used (30 min at 190 °C; HCl – HNO_3 mixture). Samples Pre, Cit, Dis and Imp were prepared and analysed separately from other samples. Problems during preparation of the remaining samples which contained alumina and zirconia were encountered. A white, solid residue was found after the digestion step leading to a repetition of the dissolution step.

4 Results and Discussion

4.1 Evaluation of Synthesis Methods using Alumina supported Iron

Five samples containing 10 wt% alumina as support, were characterised. Whereas four were synthesised for this work the fifth one, mechanical mixing, was chosen as an already prepared reference sample which is described in chapter 3.1.6 . Figure 4.1 shows the final products of the preparation steps. All samples have a characteristic reddish brown colour of haematite. Impregnation, however, stands out with a light orange tone, which suggests different surface properties.

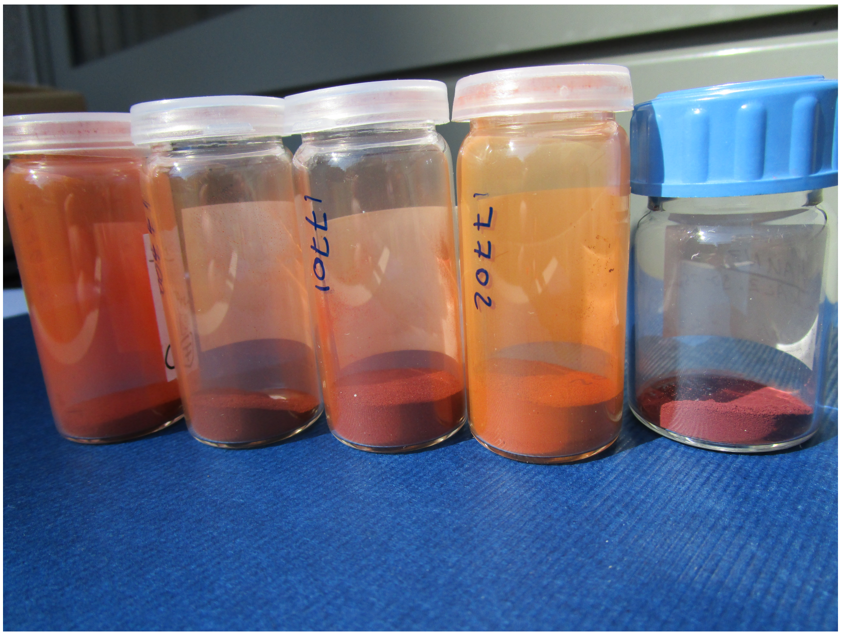

Figure 4.1: The final products of five different preparation methods. From left to right: co-precipitation, dissolution, citrate method, impregnation and mechanical mixing.

4.1.1 Yields and Oxygen Carrier Compositions

Aluminium was chosen as support metal, because of the good stability previous works could obtain with this combination of metals [9, 13, 25, 57, 58]. Since the reference sample MM contained 10 wt% of alumina, the other samples were synthesised with the corresponding aluminium content with the assumption of full oxidation of the metals.

Table 4.1 presents the results of the elementary analysis among other values. Overall the expected oxide composition with 90 wt% of haematite was achieved. Oxygen carrier Pre and Cit are very close to this value, with a slightly higher alumina content. In comparison to these methods, samples Dis and Imp deviated further from the determined haematite value. Therefore, the sum of metal oxides ($\sum$ Metal) was calculated as a guide value. If the metals are fully oxidised, 100 wt% should be reached. Because both oxygen carriers obtained a slightly higher value it suggests that the samples were either not completely oxidised or formed a compound with a lower state of oxidation, in this case for example hercynite. Mechanical mixing stands out with a significantly lower share of haematite. Additionally the overall sum of metal oxides only amounts to a total of 95.5 wt%. This could be explained by contamination, but the first reduction during thermo-gravimetric measurements proves a higher reducibility than the iron content suggests. Derived from this, it is likely a result of an higher iron content than 86.7 wt%. The same deviation occurs in another chapter, in which the reduction values for the aluminium and zirconium containing samples (also see table 4.7) could not match the stated iron content during the reduction process as well. These things lead to the assumption that problems during sample digestion (second batch) could have had an effect on the accuracy of the iron content.

Table 4.1: Calculated theoretical metal oxide composition based on the metal content obtained by elementary analysis and *on the first reduction during TGA measurement.

sample	**yield [%]**	**$Fe_2O_{3,Red}$* [wt%]**	**Fe_2O_3 [wt%]**	**Al_2O_3 [wt%]**	**$\sum$ Metal [wt%]**
Co-Precipitation	91.6	89.2	89.9	10.7	100.6
Dissolution	92.6	89.7	91.4	10.1	101.4
Citrate Method	95.1	89.4	89.2	10.9	100.1
Impregnation	98.1	90.4	92.4	9.2	101.6
Mechanical Mixing	-	90.6	86.7	11.3	95.5

The yield of synthesis was calculated for estimating material conversion. Over 90 wt% of the theoretical yield could be obtained with every preparation method. Impregnation yielded 98.1 wt% after synthesis, which was followed by the citrate method with 95.1 wt%. Preparation method dissolution showed a higher product loss, which resulted from product-deposition on the flask walls. For co-precipitation, which only yielded 91.6% of the expected value, the major losses can be explained by the washing procedure. The solid phase could not be completely settled before the liquid phase was disposed of and hence reduced the overall yield. There are no direct values for the preparation yield of sample MM, but its preparation resulted in higher product losses by caking on the bottom of the mixing equipment.All methods had further losses in the after preparation step, which was generally around 50 wt% of the product yield of the synthesis.

4.1.2 Surface Properties

Scanning Electrode Microscopy

Co-Precipitation: As figures 4.2 and figure 4.3 show, the co-precipitated oxygen carrier has a good surface structure before and after red-ox cycling. EDX after cycling proves a slightly higher aluminium content of 9.3 wt% aluminium compared to 8.2 wt%, which were detected by elementary analysis. Overall, iron and aluminium remained distributed and did not undergo visible phase separation at the surface. This aspect suggests aluminium accumulation during cycling on the outer region of the particle, which is a good property in order to stabilise an iron particle if hercynite is formed. The grainy surface structure, however, underwent sintering. Neighbouring grains merged and built an angular structure that is still homogeneous and porous but lost surface by building bigger, edged agglomerates with distinct sintering necks.

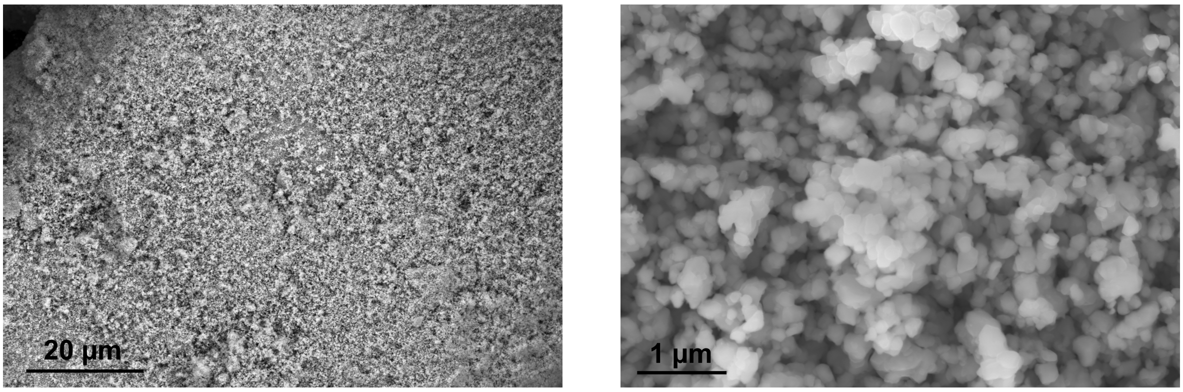

(a) Structure overview.

(b) Grain structure detail.

Figure 4.2: SEM pictures of the fresh co-precipitated oxygen carrier Pre.

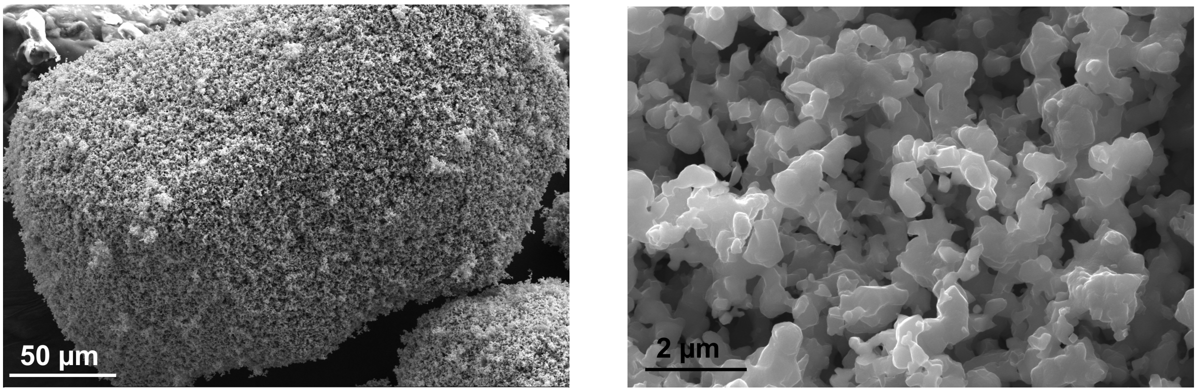

(a) Structure overview. (b) Grain structure detail.

Figure 4.3: SEM pictures of the co-precipitated oxygen carrier Pre after 20 red-ox cycles.

Citrate Method: In figure 4.4 the particles of the oxygen carrier Cit is shown. The particles are sharply edged and partly rectangular, with some small particles in between. The SEM pictures show that the oxygen carrier overall kept its shape during TGA-measurement. Yet, the particle surfaces transformed from a closed to a porous structure after red-ox cycling. More details can be seen in figure 4.5. The fresh oxygen carrier consists of a dominant darker structure 4.5(f) with a "waved" texture and insular, round holes. This darker phase is partly covered by a grainy phase, which appears in a lighter colour 4.5(e) in SEM pictures. While the first phase only consists of 0.77 wt% aluminium in EDX, the second phase reaches a high amount of 9.7 wt% aluminium, which may be even higher caused by the scattering effect of the surrounding iron-rich, darker phase. These pictures clearly illustrate the partly inhomogeneous nature of the oxygen carrier prepared by the citrate method. SEM pictures of the sample after TGA-measurement in figure 4.5(d) and 4.5(g) show completely different results. The surface became porous and far more homogeneous than in the initial state. The overall EDX shows an aluminium content of 8.9 wt% to 9.7 wt% aluminium which slightly exceeds the expected values obtained by elementary analysis of 8.5 wt%.

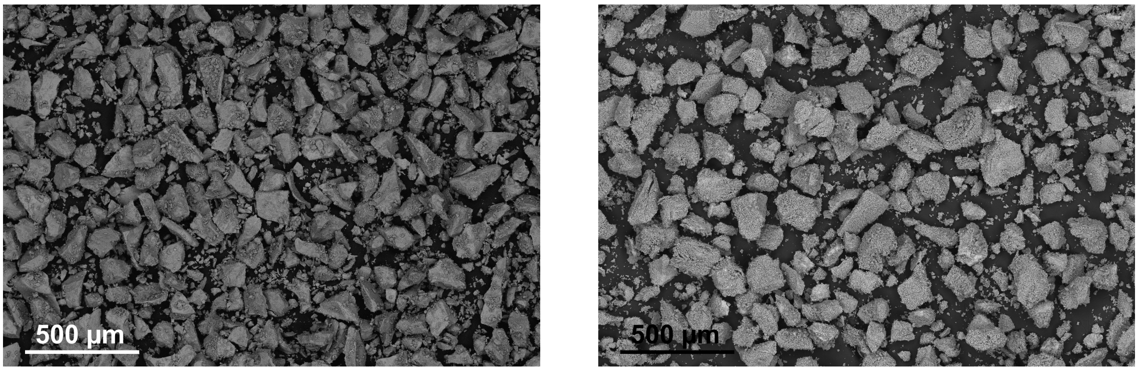

(a) Powder of the fresh oxygen carrier. (b) Powder after 20 cycles of TGA-measurement.

Figure 4.4: SEM pictures of the oxygen carrier Cit. An overview of the powder and particles.

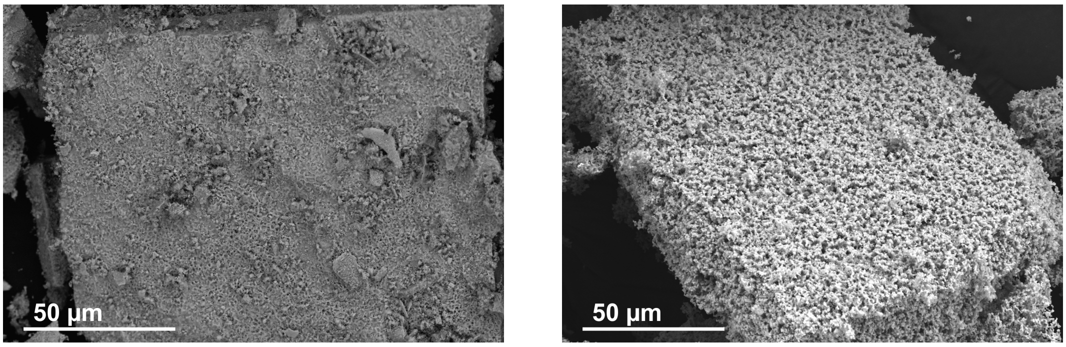

(a) Fresh oxygen carrier particle.

(b) A particle after 20 red-ox cycles.

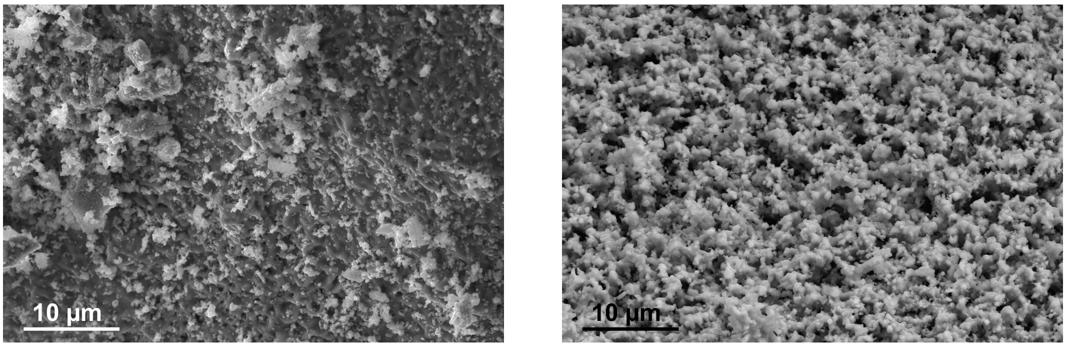

(c) Surface of the fresh oxygen carrier.

(d) Surface detail after 20 redox cycles.

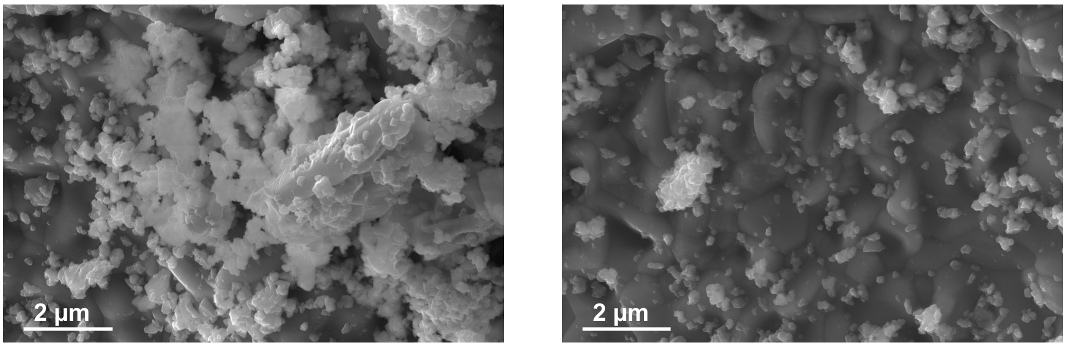

(e) The lighter phase of a fresh oxygen carrier.

(f) The darker phase of a fresh oxygen carrier.

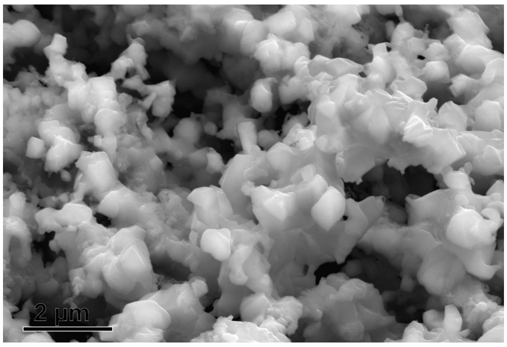

(g) Closer detail of the surface after 20 redox cycles.

Figure 4.5: Structure details of the oxygen carrier prepared by the Cit.

Dissolution: The precipitation by dissolution produced an inhomogeneous iron-aluminium material. Oxygen carrier Dis stands out with variously shaped particles, which differ in form and structure. In figure 4.6(a), a great part of the sample is degraded into very small particles far below 90 µm. This dis-composition can be the result of strain applied by the high voltage of 15 kV used for SEM analysis or might be caused by friction during sample handling and storing. Although post-preparation steps were the same for all samples in this work, Dis is the only sample showing a severe degradation in SEM pictures. After TGA-measurement, however, the particles keep their determined size and shape. It appears that the cycling positively affected the mechanical stability of the sample as can be seen in figure 4.6. Figure 4.7(a) shows details of a fresh sample. It stands out with a vast amount of various structures. They differ in grain size (4.7(d) area B) but also show several areas (4.7(c) area A) which already sintered during the calcination step. The progressed state of sintering clearly indicates a lack of homogeneous distribution of the added aluminium, which normally is a good stabiliser during heat treatment. After TGA-measurement the sample became more uniform, but still the two prominent structures remained. Figure 4.7(b) and 4.7(e) show a lighter area which reached the final state of sintering and lacks any inter-granular space or porosity. This structure possesses a low aluminium content of only 0.3 % in EDX, see figure 9.3. While structure D with a aluminium content of 2.5 % resembles the other samples with an uniform, porous surface.

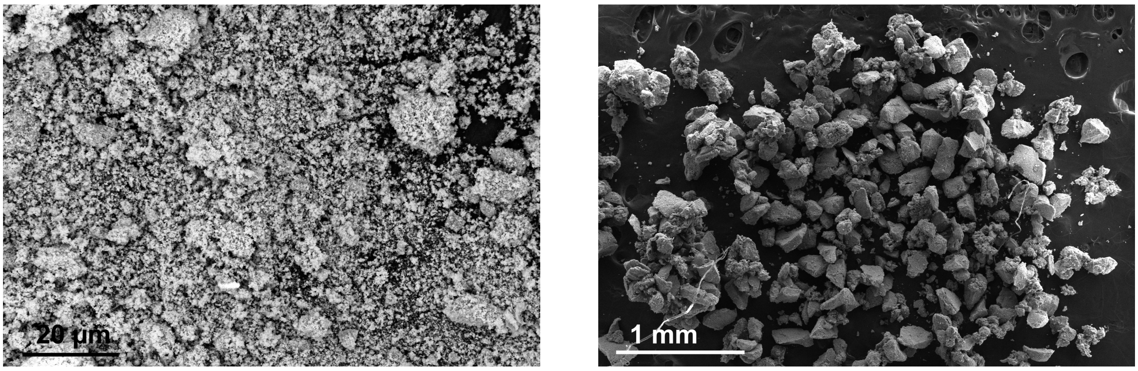

(a) Before TGA measurement.

(b) After TGA measurement.

Figure 4.6: SEM pictures of the general particle structure of oxygen carrier Dis.

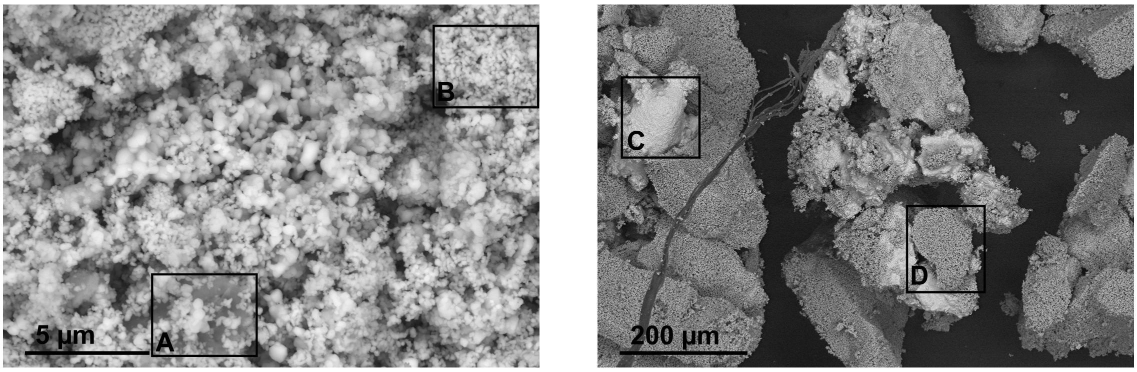

(a) Partical surface with typical grain formation, which consists of two prominent surface structures A and B before TGA measurement.

(b) Partical surface with typical grain formation, which consists of two prominent surface structures C and D after TGA measurement.

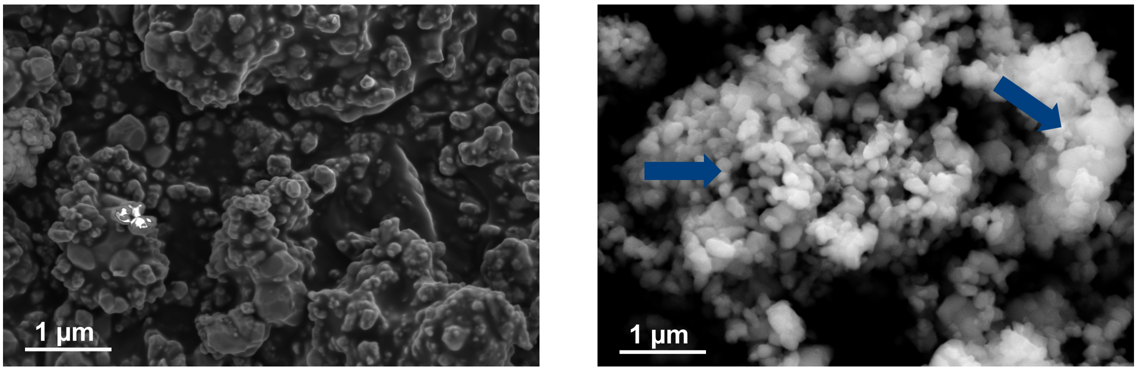

(c) Structure A before TGA measurement.

(d) Structure B before TGA measurement.

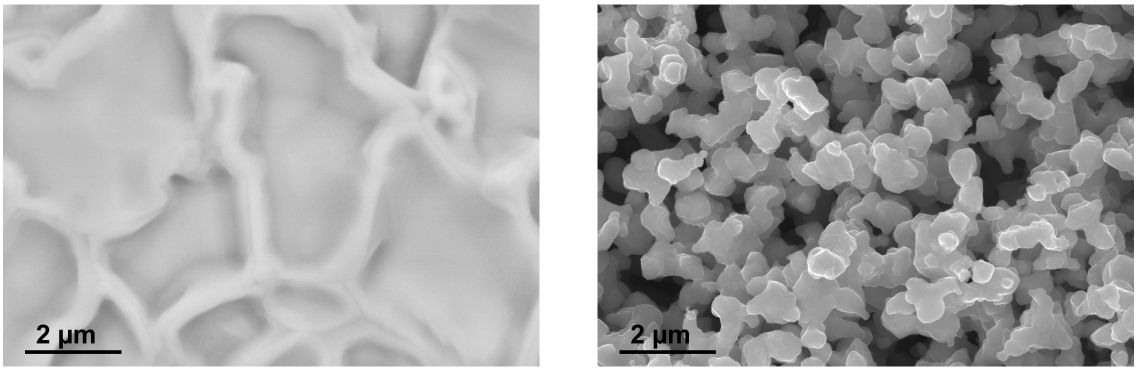

(e) Structure C after TGA measurement.

(f) Structure D after TGA measurement.

Figure 4.7: SEM pictures of the oxygen carrier Dis before and after 20 cycles of reduction and oxidation.

Impregnation: The particles presented in figure 4.8 show a two-phased structure before cycling. It consists of a darker iron-rich phase and an aluminium-rich lighter coloured, grainy layer seemingly coating the iron rich particle. After cycling, however, this structure can no longer be found. Figure 4.10 shows particles characterized by a light-coloured, porous surface structure resembling other oxygen carriers. Throughout this surface, areas with a seemingly higher (see figures 4.10(a) and 4.10(c)) and a lower porosity (see figures 4.10(b) and 4.10(d)) can be found. These structures vary in their aluminium content. While the tighter-packed, sharp-edged structure with lower porosity consists of 4.3 wt% aluminium in EDX the other one only contains 2.3 wt% aluminium, which are both far lower than the expected 7.0 wt%.

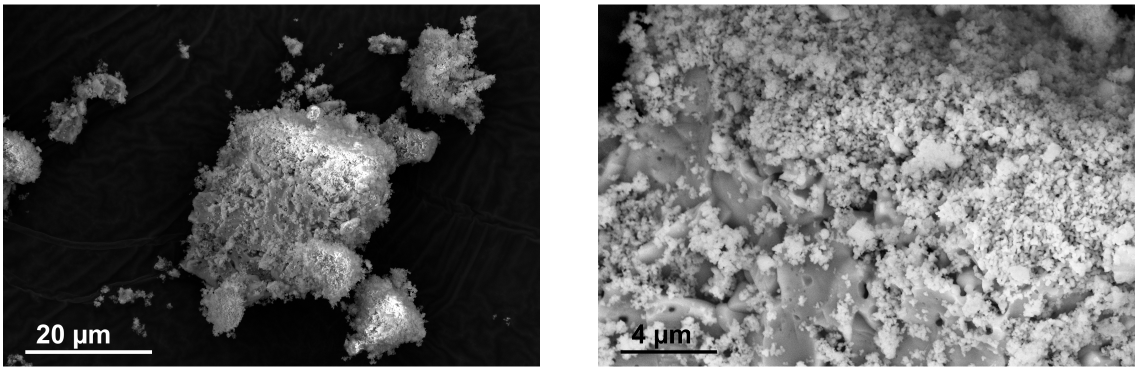

(a) A particle.

(b) Surface detail.

Figure 4.8: SEM pictures of the impregnated oxygen carrier before TGA-measurement.

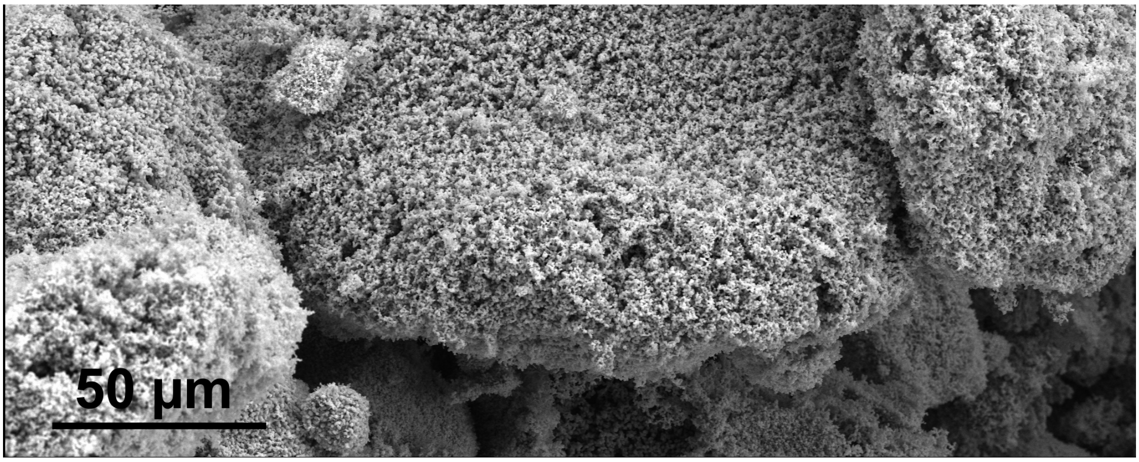

Figure 4.9: Typical grain formation after 20 cycles of reduction and oxidation.

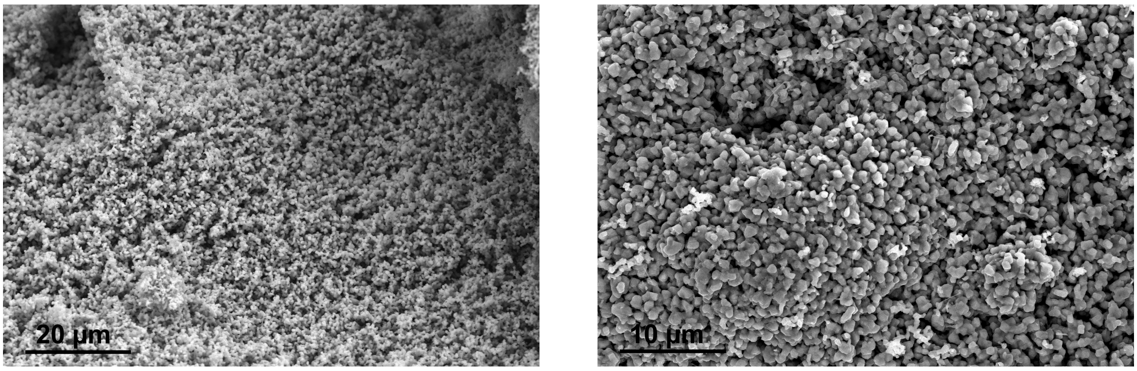

(a) Structure with higher porosity.

(b) Structure with lower porosity.

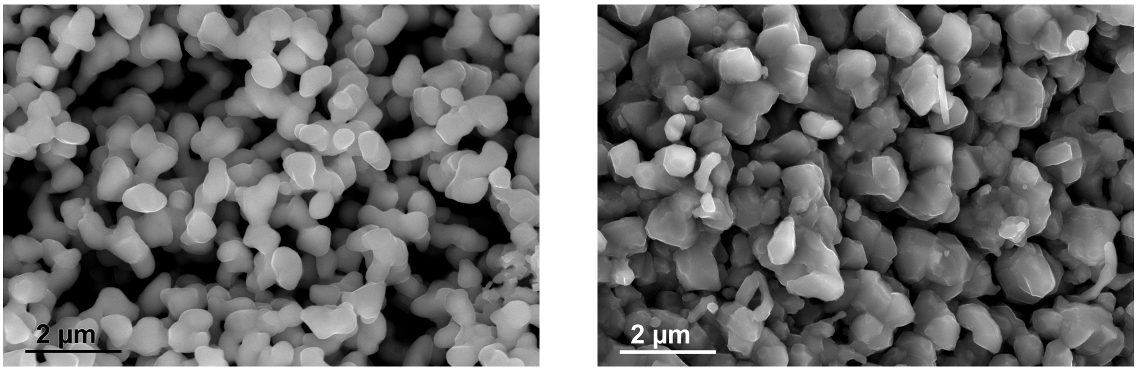

(c) Detail of the structure with higher porosity.

(d) Detail of the structure with lower porosity.

Figure 4.10: SEM pictures of the impregnated oxygen carrier after 20 cycles of reduction and oxidation. With two different surface structures.

Mechanical Mixing: Figure 4.11 depicts that the mechanical mixed oxygen carrier consisted of round-shaped particles that did not change shape during repeated red-ox reactions. The boxed area in figure 4.11(c) highlights an alumina particle on the surface of a bigger iron-rich particle, which can be seen in detail in figure 4.11(c). The EDX of the framed spot yielded a high aluminium content of 79.0 wt%, while the surrounding surface only consists of 2.2 wt% aluminium. After TGA-measurement agglomerates are still visible on the surface as shown in figure 4.11(d), however, an EDX of this area detected only 2.5 wt% of aluminium. Therefore, the alumina-rich agglomerates disappeared and only a homogeneous surface composition remained. SEM pictures with more details of the iron-rich phases show a further remarkable structure. Before red-ox cycling the surface features the characteristic grainy surface, as can be seen in figure 4.11(e). Yet, during TGA-measurement, grains sintered and built a terrace-formed structure, which might provide easier access for reaction gases.

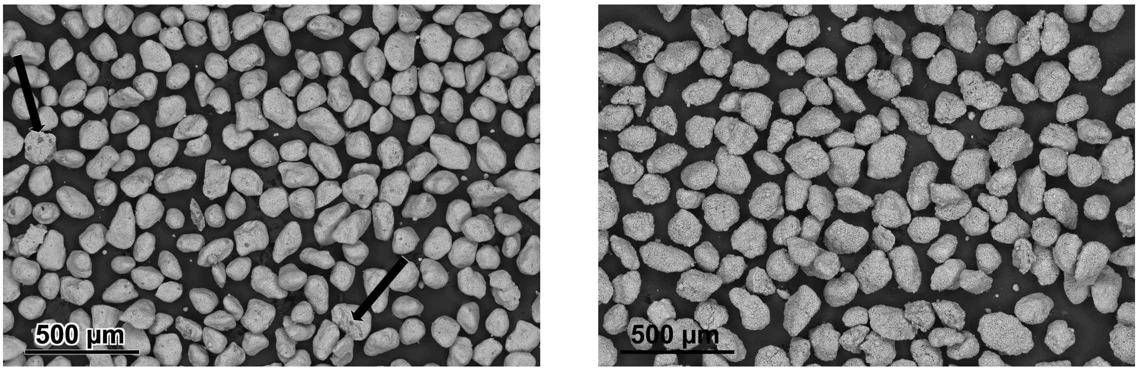

(a) Powder of a fresh oxygen carrier.

(b) Powder after 20 cycles of TGA-measurement.

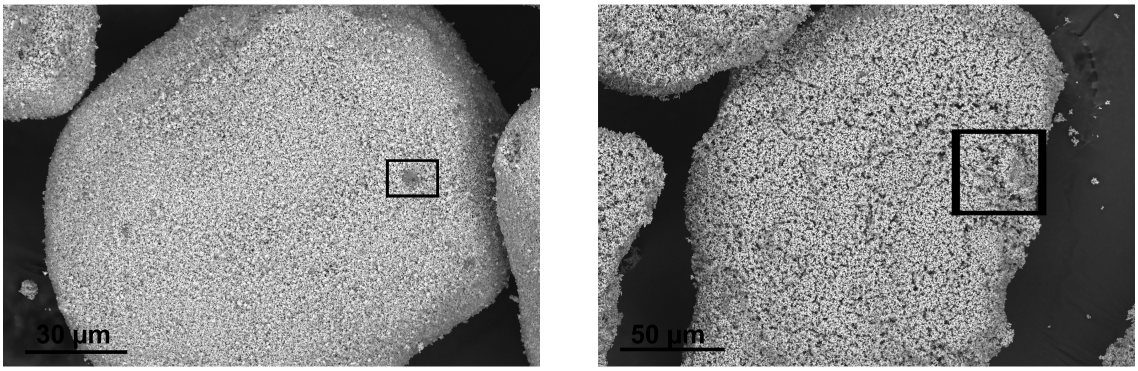

(c) A single particle of the fresh oxygen carrier.

(d) A single particle after 20 cycles of TGA-measurement.

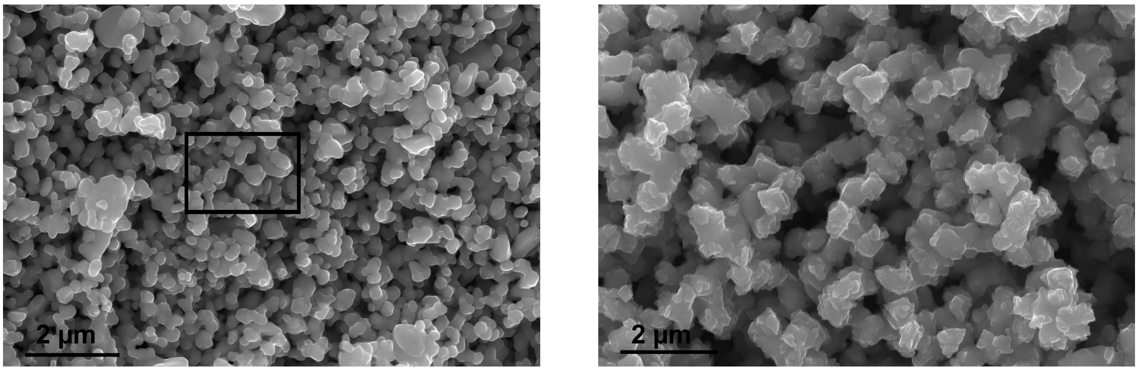

(e) Surface detail of the fresh oxygen carrier.

(f) Detail of the surface structure after 20 redox cycles.

Figure 4.11: SEM pictures of the oxygen carrier prepared by MM.

Mercury Intrusion Porosimetry

To further evaluate the surface properties mercury intrusion porosimetry was carried out on the iron - alumina samples. This method gives general values like surface area, total porosity and pore radii distribution, which are important factors in reaction kinetics. The obtained values for the samples are shown in table 4.2.

Measurements showed that sample MM possesses the highest surface area with 7.9 $m^2\,g^{-1}$ with a total porosity of 59.4 % and a comparably small average pore diameter of 0.2 µm. Samples Imp and Pre closely follow with 6.9 $m^2\,g^{-1}$ and 6.6 $m^2\,g^{-1}$ respectively and a total porosity with 42.7 % and 39.0 %. While those are resembling values, the average pore diameter, however, is significantly smaller for Imp with 11.3 µm than for sample Pre with 34.3 µm. Samples Dis and Cit share the smallest surface areas with 4.6 $m^2\,g^{-1}$ and 4.3 $m^2\,g^{-1}$ respectively. While oxygen carrier Dis additionally reaches the lowest total porosity with 29.0 % with a higher average pore diameter of 33.2 µm, Cit has the highest value for the total porosity with 42.7 % and a smaller average pore diameter of 25.7 µm.

Results show that samples MM and Imp, which are based on commercial powders, have the highest total specific surface area. Furthermore, both oxygen carrier possess rather small pore radii, whereas the average pore diameter of MM is smaller by the factor ten if compared to oxygen carrier Imp.

Table 4.2: Values of surface properties for the oxygen carriers prepared by different preparation methods as obtained by mercury intrusion porsimetry.

	Precipitation	**Dissolution**	**Citrate Method**	**Impregnation**	**Mechanical Mixing**
Total cumulative volume [$mm^3\,g^{-1}$]	295.4	143.7	404.4	314.4	362.3
Total specific surface area [$m^2\,g^{-1}$]	6.6	4.6	4.3	6.9	7.9
Average pore diameter [µm]	34.3	33.2	25.7	11.3	0.2
Total porosity [%]	39.0	28.0	75.0	42.7	49.4
Bulk density [$g\,cm^{-3}$]	1.3	1.9	1.9	1.4	1.4
Apparent density [$g\,cm^{-3}$]	2.2	2.7	7.4	2.4	2.7

Diagrams in figure 4.12 show the detailed pore diameter distribution. For a better overview the data points were summarised in 50 intervals. All samples show a multi-modal pore size distribution with two predominant areas. First area lies in the diameter range of 0.005-0.3 µm, second around 10-100 µm. As the samples are powders in a range of 90 - 125 µm, the first area can be related to the internal pore system, the second must be mainly assigned to inter-particle space which is filled during lower pressure ranges. Sample MM, however, is the only sample which does not possess a sharp volume increase in this range. It shows a linear increase instead. This progress can be explained by the missing calcination step before mercury porosimetry was performed. Although it was fractionated the mixed powder of alumina (20 - 30 µm) and haematite (< 325 µm) was not heat treated like the other samples which may have lead to weak cohesion. Therefore, it is likely that the second area resulted from a collapsing agglomerate structure or a rearrangement process. At 20 µm in figure 4.13(e) a signal jump correlates with the size of alumina powder used, which is a typical measurement artefact for collapsing powder agglomerates.

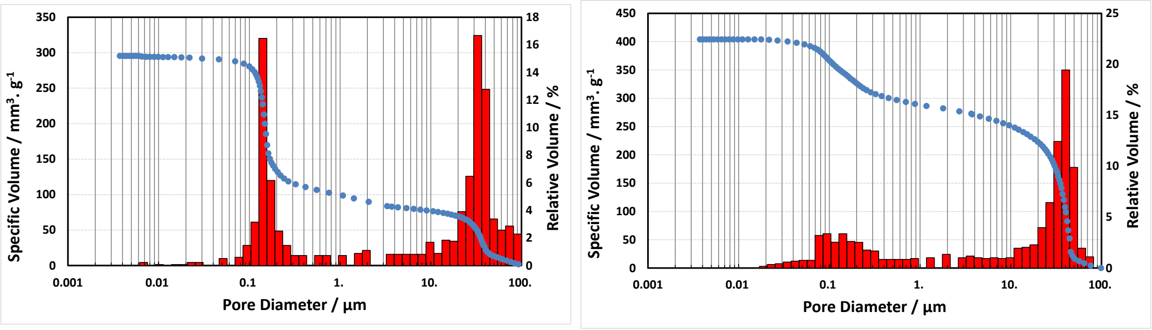

(a) Precipitation (b) Citrate method

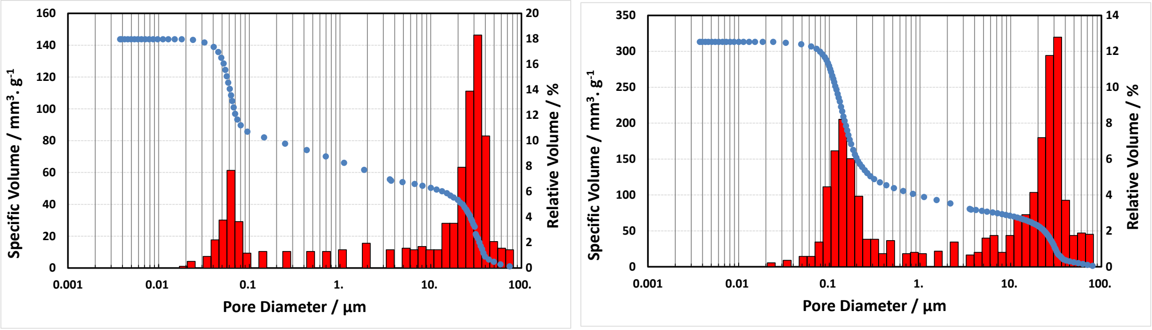

(c) Dissolution (d) Impregnation

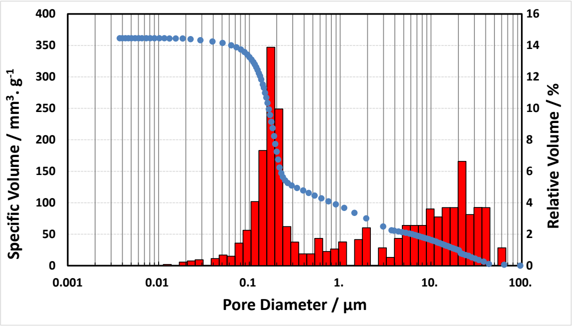

(e) Mechanical mixing

Figure 4.12: Mercury intrusion curve and pore diameter distribution.

Considering the inter-particle space discussed above, values for the specific surface area and the average pore diameter were recalculated to evaluate the inner porosity. For this, only data for the area between 0.001 µm and a chosen start diameter were included, which was chosen according to the linear area after the first rise of the specific volume. Results are listed in table 4.3. In general, values for surface area did not change. As a result of recalculation, however, the average pore diameter changed. Oxygen carriers Dis and Cit possess the smallest average pore radii with < 0.1 µm, while the other preparation methods have radii around 0.15 µm. These values correlate to the SEM images in the chapters before, where Dis and Cit show surfaces with non-porous structures.

Table 4.3: Recalculated values for the mercury intrusion porosimetry excluding values obtained by inter-particle space.

	Precipitation	**Dissolution**	**Citrate Method**	**Impregnation**	**Mechanical Mixing**
Start Diameter [µm]	5	1	4	3	2
spec. Surface [$m^2 \cdot g^{-1}$]	6.533	4.201	4.515	6.369	7.499
Pore Diameter [µm]	0.141	0.053	0.083	0.131	0.187

In figure 4.13 the mercury intrusion and extrusion according to its pressure is presented. Their shape and hysteresis give information on the particular pore structure and geometry. Sample Pre shows a typical curve of a powder with cylindrical pore structure [59]. Area A-B result from powder particles which rearrange under rising pressure. In area B inter-particle space is filled, as discussed before. The intra-pores are intruded in area C. The extrusion curve has the same shape as the intrusion curve showing only a small amount of entrapped mercury, which is typical for cylindrical pores [60]. While the intrusion for sample Imp is comparable to sample Pre, MM lacks the first sharp increase because of the loose powder as discussed before. Both samples show the comparable extrusion behaviour, as for the finally extruded mercury volume is much lower than the intruded volume. This incomplete release of mercury is generally caused by the bottle-neck effect which is characteristic for sphere-shaped pores. However, a certain amount is still released during extrusion. Sample Imp shows the highest amount of entrapped mercury. It only releases 33 % of its intruded volume, while sample MM recovers 64 % of the mercury. Therefore it might be that only a part of the pores posses a spherical form. It is mentioned here, that calculated values in table 4.3 and table 4.8 might differ from the true value as the spherical shapes generate a higher surface than cylindrical pores on which surface calculation were based on. The extrusion curve of sample Dis is out-standing. It shows no hysteresis during extrusion until 25 MPa is reached.This could either be the result of micro-fissures which have a sheet shaped form, or it could be entrapped air which was not removed by the evacuation process. This may be the result of occlusion caused by the sintering process becoming accessible by destructive forces of the high pressure applied during the analysis process, or insufficient out-gassing at the beginning of measurement. Striking feature of oxygen carrier Cit is its big inter-particle and a rather low intra-particle space, which causes a high porosity value of 75 %. There is no significant extrusion shape which may indicate a special pore structure.

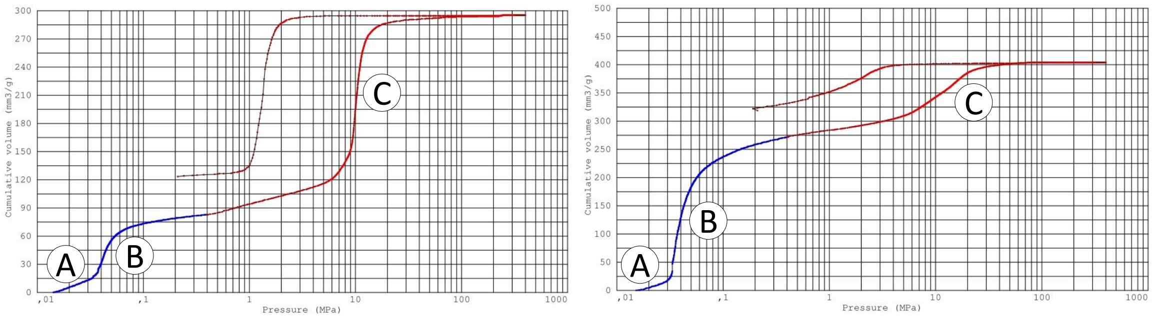

(a) Precipitation (b) Citrate method

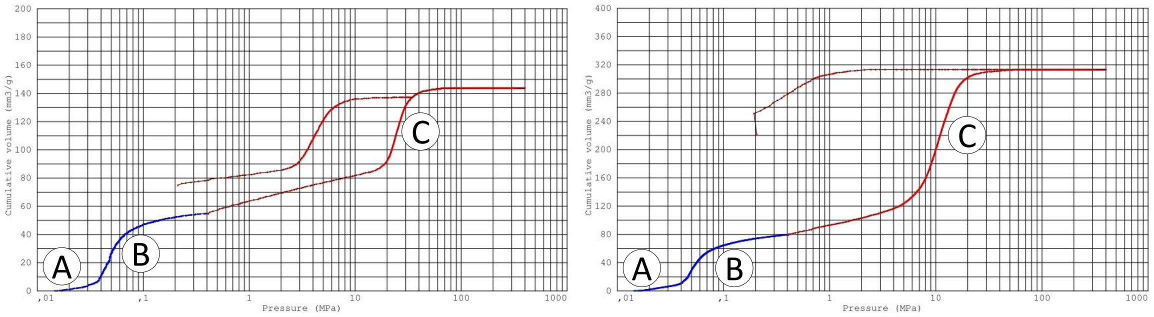

(c) Dissolution (d) Impregnation

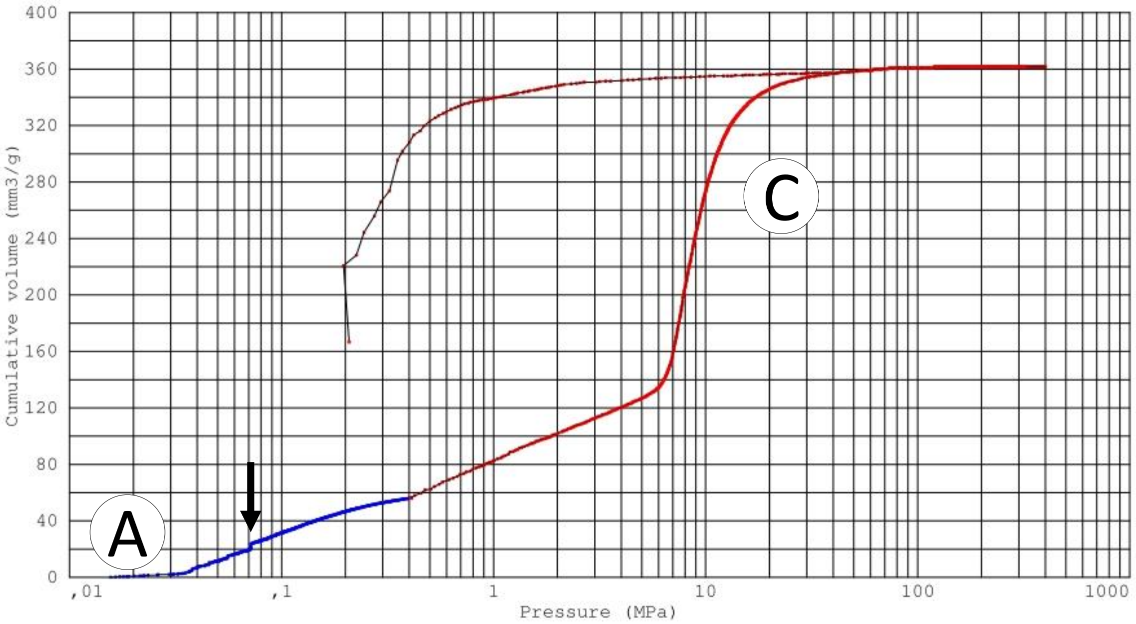

(e) Mechanical mixing

Figure 4.13: Mercury intrusion and extrusion curve.

4.1.3 Stability during cyclic thermo-gravimetric measurement

The influence of different preparation methods on the conversion stability and reaction behaviour during the steam-iron process were evaluated by thermo-gravimetric analysis. The obtained diagrams in figure 4.14(a-e) show that all routes of synthesis provided oxygen carriers with a high stability during 20 cycles of red-ox reaction, when compared to unsupported haematite in figure 4.14(f). The pure iron oxide severely sintered, which is accompanied by loss of reaction speed and conversion capability during given time frame of oxidation and reduction.

As reference for conversion, lines for each oxidation level were included (Fe, FeO, Fe_3O_4), which were based on the iron content obtained by elementary analysis. On first examination it can be seen that for all oxygen carriers reduction mostly reached the iron level as predicted by calculations, while the oxidation steps gradually underperformed. It is likely that the first reduction, like in the pure haematite sample, lead to a loss of surface area. This might be caused by coagulation or other structural changes during the oxygen exchange process. An additional reason can be a solid-solid reaction between the alumina and wustite, leading to hercynite which can not be oxidised by water vapour leading to losses during the oxidation step. The weight deviation as a function over time (DTG), also reflects deactivation after the 1^{st} cycle. It suggests that the first reduction is overall the fastest reaction.

Two oxygen carriers (MM and Cit), however, fell below the calculated iron level. As discussed before in chapter 4.1.1, mechanically mixed samples were analysed with difficulties, which lead to lower iron contents than expected. This deviation of the expected value is reflected by not reaching the calculated weight of iron metal and hence will be considered in calculations later on. In these calculations the iron content is assumed to be the iron level of the first reduction. As for the deviation of oxygen carrier Cit the error can be related to an weighing error. During the drying process before the TGA-measurement a defect of the oven prevented drying at 110 °C. This resulted in a lack of water-removal and a distorted sample weight, as the adsorbed water evaporated eventually during the heat-up phase. Another important issue for this measurement was a program error after the reduction of the 12^{th} cycle. It prevented a jump from the purge phase into the oxidation phase putting the cycling at a halt for 11 h. In this time, as can be clearly seen in 4.14(b), the sample slowly oxidised to the weight of the magnetite level, which should not happen under nitrogen atmosphere. The last purge phase shows the same behaviour. This one, however, followed an oxidation step and surpassed the magnetite level, which is thermodynamically impossible with water vapour. This leads to the conclusion that low amounts of oxygen entered the sample-room and caused oxidation of the sample.

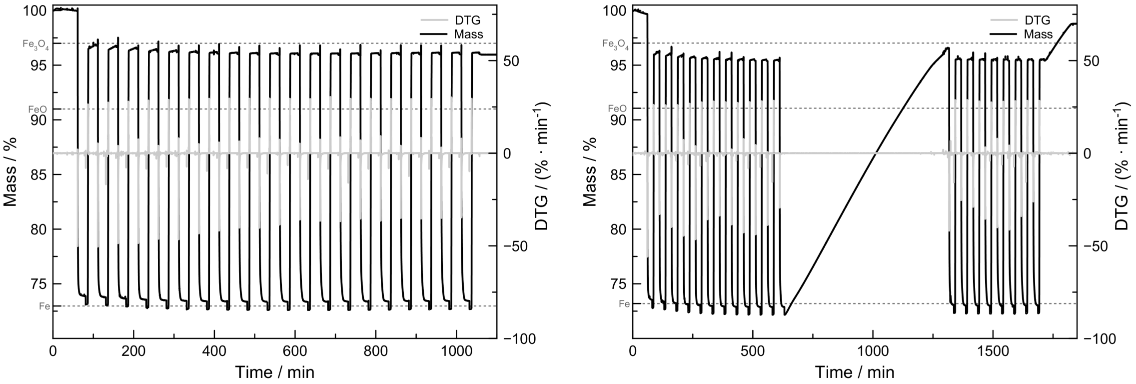

(a) Co-precipitation (b) Citrate method

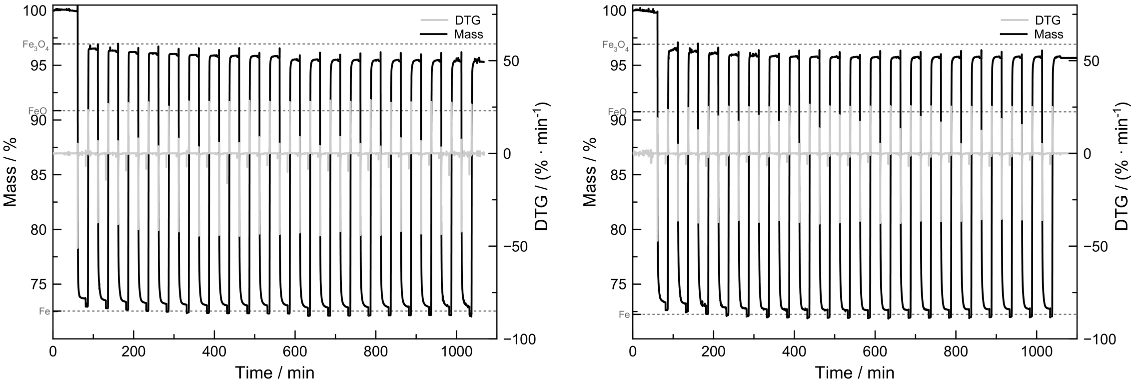

(c) Dissolution (d) Impregnation

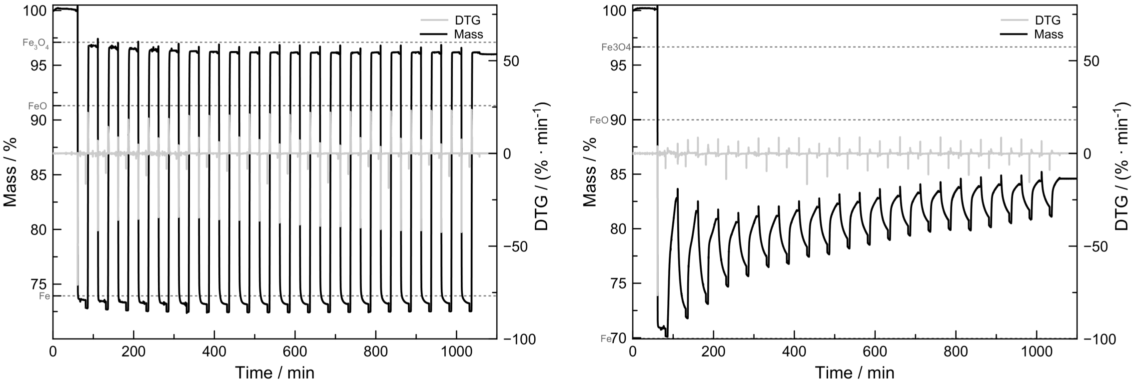

(e) Mechanical Mixing (f) Unsupported haematite powder

Figure 4.14: Results of thermo-gravimetric analysis with 20 cycles of alternating hydrogen reduction and following steam oxidation.

4.1.4 Conversion Stability

The oxygen exchange was calculated as defined in chapter 2.4 to facilitate the comparison of different oxygen carriers. Mechanically mixing was the only sample which was based on the amount of iron obtained by the first reduction, while all other samples were calculated using analytical iron content.

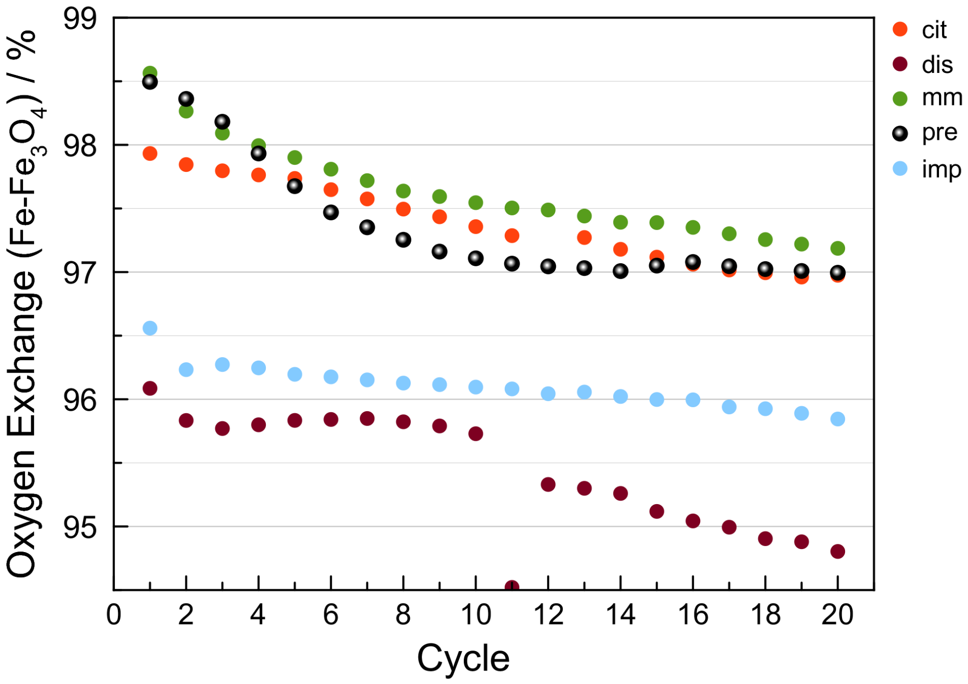

Figure 4.15: Development of the oxygen exchange over 20 red-ox cycles for all routes of synthesis.

Figure 4.15 presents the obtained values for the conversion. None of the methods could achieve an oxygen exchange of 100% during oxidation. Co-precipitation and MM started with the highest value around 98.5% but both decreased their conversion and only reached a value around 97.0% and 97.2% in the last cycle. It is noticeable, while mechanically mixing slowly decreased, the oxygen carrier Pre deteriorated rapidly until cycle 12. From then on, an almost steady oxygen conversion can be recognized. The progress of sample Cit can be compared to mechanically mixing, however, it starts at only 98% of the possible oxygen exchange. During cycle 12 the halt, caused by a program error, lead to an interruption of the negative trend of the oxygen exchange. After a high conversion which is excluded from the diagram, following value shows a slightly higher oxygen exchange (∼0.02%) than the value before oxygen oxidation. In literature a regenerating effect is ascribed to oxygen on one hand as a result of the decomposition of hercynite, on the other hand full oxidation to haematite build defects which can improve the diffusion kinetics.

Oxygen carrier Dis and Imp start at a much lower oxygen exchange. The first at 96.1% and the latter at 96.6%. Obviously the inhomogeneous and sintered areas, which were found only for these samples in the SEM pictures, did effect the performance during reaction. Yet, both show after a loss in conversion a small improvement. For Imp between cycle 2 - 4 and for Dis between the cycle 3 - 8. It is possible that the reactions, which are accompanied by mass and gas transport, changed structural properties of the oxygen carriers. In SEM images certain areas posses a better homogeneity as well as higher porosity after the measurement, which might lead to a slight improvement. Impregnation is the oxygen carrier with the overall slowest decrease in conversion. Which could be an indication that the stabilising effect of the alumina is effected by coating the grains, which is a clear property of this sample as SEM images showed. Dissolution shows a conspicuous drop during the 11^{th} cycle. As figure 4.16 proves, swelling of the oxygen carrier caused some of the material to grow over the borders of the sample plate and to break off. Hence, the loss of conversion capability during cycling.

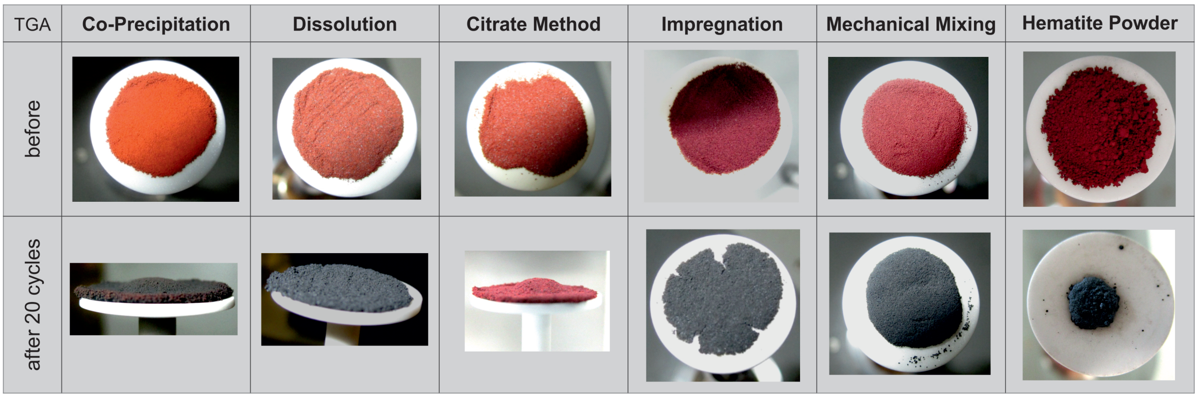

Figure 4.16: Oxygen carrier before and after thermo-gravimetric analysis.

4.1.5 Change of Reactivity during the Reduction and Oxidation Process

Following diagrams 4.17 to 4.21 depict the effects of repeated reduction and oxidation on reactivity over time, which is shown in the reaction progress during TGA measurement. In the diagrams, a certain number of curves were selected and superimposed on one another to facilitate comparison of occurring changes. Because of the fast changes during the first cycles more curves of the earlier cycles were chosen. Interference signals are due to vibrations caused by movements in the measurement room and were not removed by mathematically smoothing to avoid falsification of the curve progress.

The reaction curves of all oxygen carriers have a characteristic shape for oxidation and reduction. Both reactions divide in a fast reaction where most of the oxygen carrier reacts rapidly. In this phase oxygen is freely accessible for the reaction gases and available at the surface. This fast reaction ends at a more or less sharp bend, where it becomes very slow.

After this point just small changes in weight can be seen. Kidambi et al. contributed this slow mass loss to the reduction of hercynite, but also diffusion through the product layer might be the limiting reaction step at this point [20, 61]. For all oxygen carriers the reduction is an overall slower process than the oxidation and reaction progress is more likely to change. All diagrams show a higher mass loss during reduction after several cycles to which the oxidation responds with a drop.

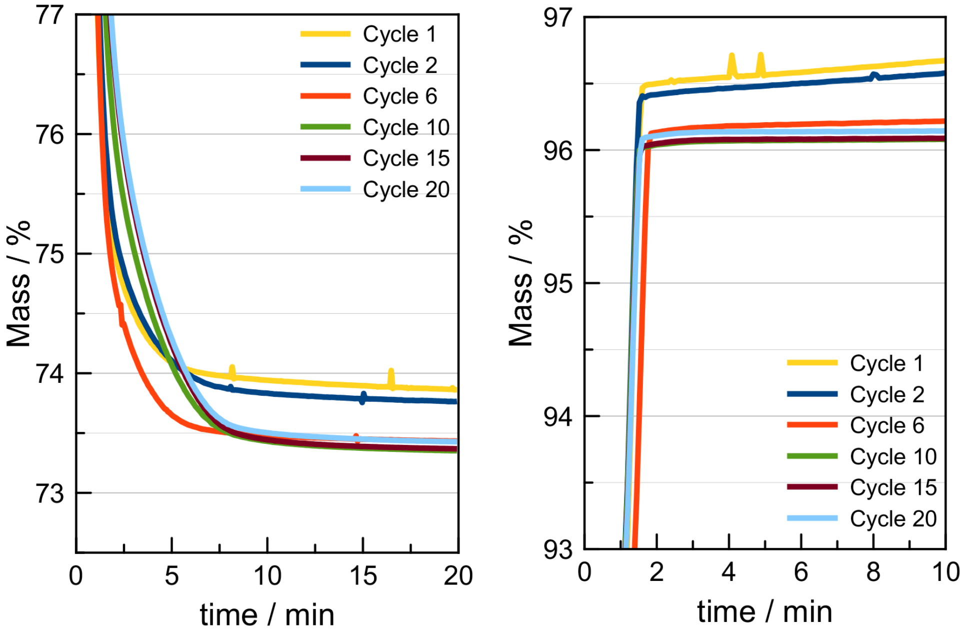

(a) Reduction Progress.

(b) Oxidation Progress.

Figure 4.17: Details of the reduction and oxidation progress of the oxygen carrier prepared by co-precipitation (Pre) for selected cycles.

Changes in reaction behaviour of sample **Pre** during the repeating reactions can be seen in figure 4.17. Neither, reduction ($w_{\mathrm{Fe,th}}$=73.0 wt%) nor oxidation ($w_{\mathrm{Fe_3O_4,th}}$=97.0 wt%) are completed. The comparison of reaction curves shows that reduction is an overall slower process than oxidation. While the fast oxidation step is finished under two minutes, reduction takes longer with about twelve minutes. From cycle 10 on the reduction progress remains almost stable, after deteriorating in the first 6 cycles. This progress goes along to the losses in oxygen exchange which also stabilises from the 11^{th} cycle on, as described in the chapter before. An explanation for the change during the measurement can be made when discussed in connection with SEM images. During the cyclic process surface area decreased because of grain growth, which can cause slower reaction towards the end of reduction. Further EDX showed an higher aluminium content after the cycling process. This suggest that hercynite most likely precipitated during repeated reductions. Therefore, it might be concluded that the slower reduction is the result of loss in surface area and the formation of a hercynite diffusion layer, which is known for reducing reduction kinetics [62].

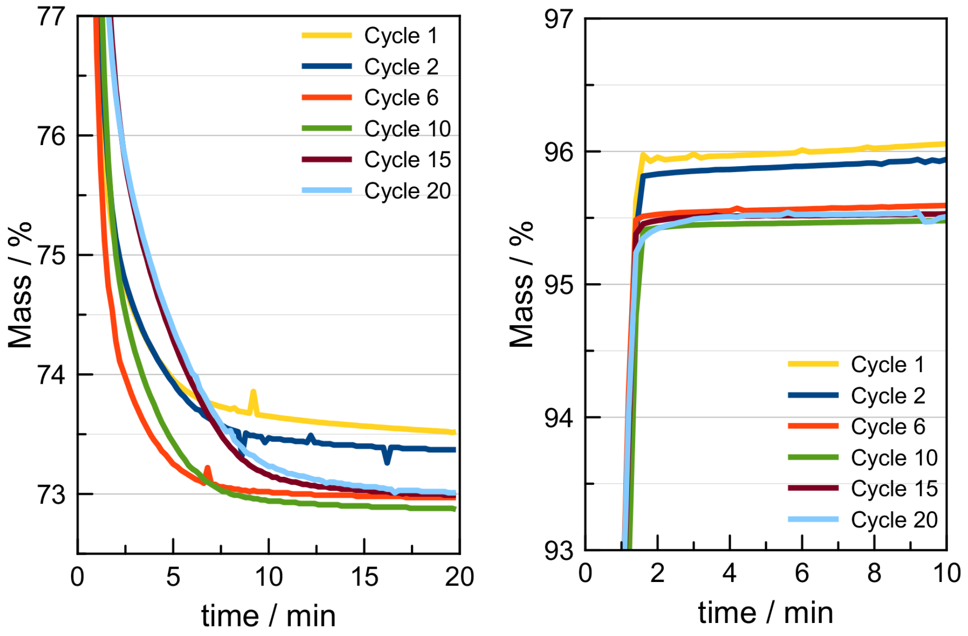

(a) Reduction (b) Oxidation

Figure 4.18: Details of the reduction and oxidation progress of the oxygen carrier prepared by the citrate method (Cit) for selected cycles.

In figure 4.18 the oxygen carrier **Cit** increased the reduction level from cycle 1 to 10. From cycle 10 on, the reduction speed decreased but stabilised around cycle 15. The shape of the final reduction curves resemble co-precipition. Yet, the reaction progress is slower. In contrast the oxidation, which also resembles oxygen carrier Pre, has the same curve shape, but the oxidation level is lower than for Pre. During cycle 15 and 20 the sharp bend slowly changed to a round transition. This change might be the effect of the long halt of the measurement after the 12^{th} reduction.

The oxygen carrier **Dis** in figure 4.19 loses reduction-velocity after the first cycle. But this drop in performance is overcome in cycle 6, which reaches a lower reduction weight but follows a similar reduction progress as in the first cycle. Reduction, however, becomes slower in cycle 20 on. Oxidation underwent bigger alterations. Its velocity of the first part of the reaction improved after the first cycle, the overall oxidation significantly deteriorated with cycle 10. The fast oxidation stopped earlier and the sharp bend became a slow transition. SEM images prove that oxygen carrier Dis is inhomogeneous and resulted in heavily sintered areas after cycling. Structural changes could be the reason for improvement during the first cycles. Area B in figure 4.7(f) possesses an higher porosity compared to the fresh sample in figure 4.7(d), which apparently had a positive effect during the first reaction phase. But areas, which were not stabilised with aluminium severely sintered and affected reaction velocity at the end of the reaction after several red-ox cycles.

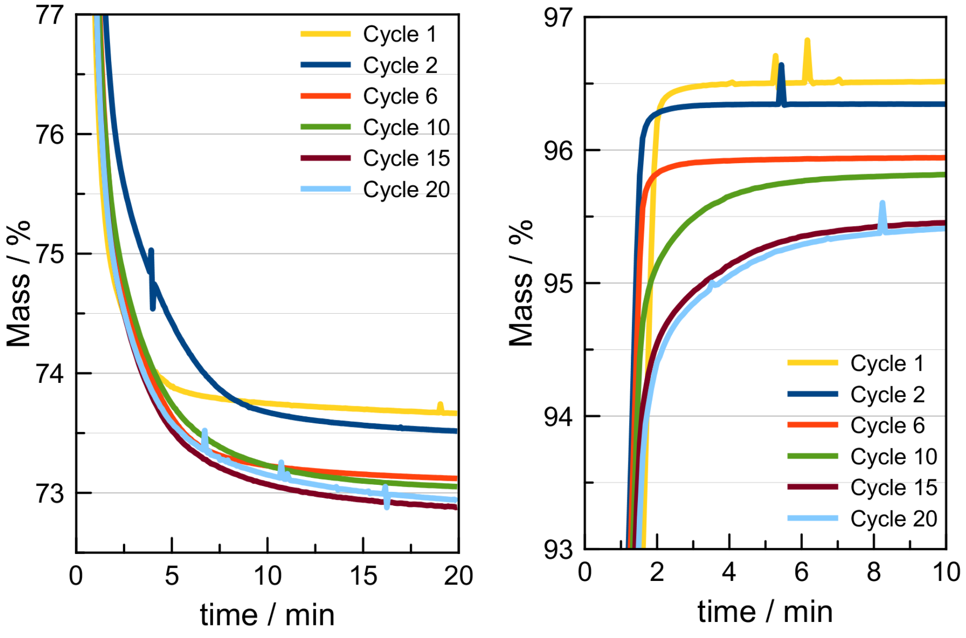

(a) Reduction (b) Oxidation

Figure 4.19: Details of the reduction and oxidation progress of the oxygen carrier prepared by dissolution (Dis) for selected cycles.

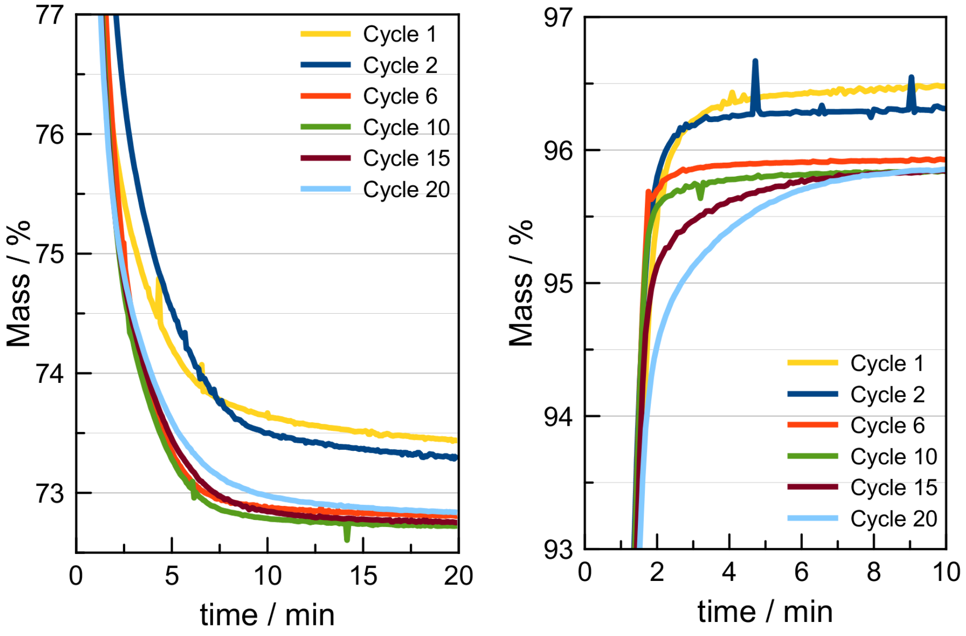

(a) Reduction (b) Oxidation

Figure 4.20: Details of the reduction and oxidation progress of the oxygen carrier prepared by Impregnation (Imp) for selected cycles.

Oxygen carrier **Imp** in figure 4.20 shows the similar changes in reaction speed as sample Dis. While the second reduction is slower than the first one, following curves are faster and reach a lower reduction state. Reduction in cycle 10 is the fastest one, but following cycles deteriorated slightly. This deterioration is also reflected by the oxidation curves. Until cycle 10 oxidation becomes faster, however, this improving effect stops and cycle 15 and 20 slows significantly down at the end of oxidation. Results indicate a positive effect of red-ox reaction process on the aluminium covered oxygen carrier. Nevertheless reaction kinetics slowly deteriorated with repeating cycles, but showing no effect on the reduction/oxidation level yet.

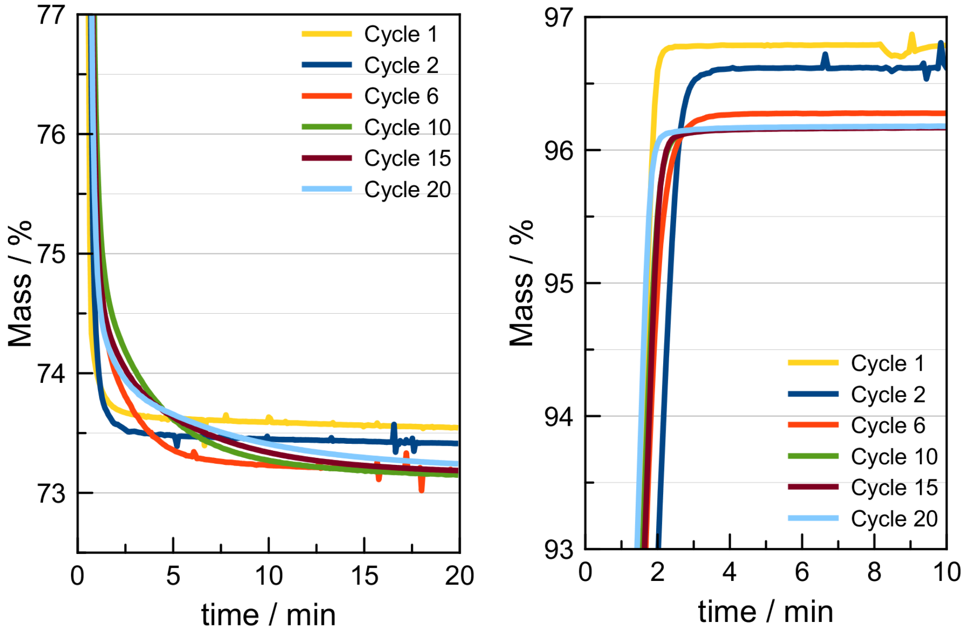

(a) Reduction (b) Oxidation

Figure 4.21: Details of the reduction and oxidation progress of the oxygen carrier prepared by Mechanical Mixing (MM) for selected cycles.

In figure 4.21 oxygen carrier **MM** stands out with the fastest speed for the first two cycles. These reactions are already finished before minute 3, which could be caused by the very high surface area this oxygen carrier possessed. Another feature, which could not be found in this extant for the other oxygen carriers, is the continuous improvement of the oxidation speed. While the first oxidation is the fastest the second oxidation is much slower like the oxygen carriers Dis and Imp. Yet, this deterioration is overcome with the following cycles until the oxidation speed of cycle 20 resembles the first oxidation.

With the purpose to compare the reaction speed of each oxygen carrier, reduction as well as oxidation of the 20th cycle are compared in table 4.4. The point of comparison is the point at which an almost steady weight is reached. From then on it is assumed that the reaction changes are too low to make significant impact on the overall conversion/hydrogen production.

In this comparison the co-precipitated oxygen carrier is the fastest sample during both reduction and especially oxidation. The oxidation process was completed under 10 minutes for all oxygen carriers. The reduction, however, never finished in the time specified in the measurement program. Therefore it led to the losses seen in the diagram for the overall oxygen exchange in figure 4.15.

Table 4.4: Reaction time of the 20^{th} cycle before only solid-solid reaction is rate determining.

sample	**reaction time [min^{-1}]**	
	redcution	**oxidation**
Co-precipitation	12	1.7
Citrate method	18	3.4
Dissolution	>20	8.3
Impregnation	17	8.9
Mechanical mixing	18	2.2

4.1.6 Conclusion and Choice of Preparation Method

In general an activation process of inhomogeneous and the non porous oxygen carriers could be observed during the tests. Diffusion processes, which occur during the repeating reduction and oxidation, are likely causing an increase of homogeneity as well as visible porosity, which showed a slightly positive effect on the reduction/oxidation behaviour of the samples, but still could not prevent deactivation.

Oxygen carrier Dis precipitated iron and aluminium unevenly. The sample consisted of different structures and compositions from the start (see figure 4.7). Its surface, however, could partly be improved by redox cycling like all other inhomogeneous samples. It showed minimal mechanical strength during SEM spectroscopy, which apparently decomposed the oxygen carrier. Those disadvantageous surface properties were reflected in low oxygen exchange capability and slowly decreasing oxidation leading to an oxygen carrier with the least attractive properties in this test series.

The citrate method resulted in an non-porous oxygen carrier, which was not homogeneous at the surface. Yet the surface underwent a restructuring process during cyclic reduction and oxidation 4.5. The surface became homogeneous and porous, which seemingly provided better accessibility for reaction/product gases during red-ox reaction. This activation process slightly improved the performance of the oxygen carrier during the first ten cycles. Like oxygen carrier Pre it also showed accumulation of aluminium (8.9 - 9.7 wt% instead of 8.5 wt%) at the surface after red-ox cycling.

Impregnation of iron sponge powder provided iron particles which had a layer of deposited aluminium on the surface. This covering layer was found by SEM images before TGA measurement (see figures 4.8(a) and 4.8(b)). A lower aluminium content of 2.3 - 4.3 wt%, after the measurement, suggests an intermixing of the metals by inward diffusion of aluminium during repeated red-ox reaction. Porosity increased as a result of the thermo-gravimetric measurement. A minimal activation could be seen at the first cycles. However, the sample slowly deactivated during reduction and oxidation but showed the lowest decrease in the oxidation process. In particular this preparation method was harder to control in terms of composition, since less aluminium could be deposited on this oxygen carrier.

In regard to surface properties and reactivity oxygen carrier MM is the most outstanding sample. While MM possesses the highest surface area and overall porosity, it lacked in homogeneity. A special characteristic is the terrace-like structure after repeated red-ox cycling (see figure 4.11(f)), which might contribute to its good reactivity and the improvement during the oxidation process because a well accessible pore structure is favourable for gas diffusion. Nevertheless, the reduction process decelerated after several cycles and could not provide a stable oxidation phase for hydrogen production.

In comparison to the mechanically mixed sample, oxygen carrier Pre slightly fell behind regarding specific surface area and porosity. Nevertheless, the co-precipitation method provided the best surface properties of the wet-chemical methods. In general, SEM images showed that it provided a homogeneous, grainy surface structure, where aluminium concentration increased at the surface during cyclic red-ox reaction. This behaviour could have positively affected stabilisation of the iron, because reduction and hence hydrogen production stabilised after several cycles. This method showed good results while providing a stable oxygen carrier with high homogeneity.

With respect to the experimental procedure and further up-scaling impregnation and dissolution are methods which need less expenditure of human labour than co-precipitation. Their disadvantage, however, is the slow evaporation of the liquids, which can form nitrose gases at the temperatures needed. The required precautions in form of gas deduction, which must be taken, further slowed down the evaportion process. The citrate method is much faster when used in the rotary evaporator, but only solutions with low concentrations of precursors can be used. This results in small amounts of oxygen carrier that can be prepared in one step. Co-precipitation needed a permanent control of the pH-value, which could be automatised like described by Kidambi et al. [20]. Nitrose gases were not formed during the precipitation at room temperature.

These results, which are summarised in table 4.5, lead to the conclusion that co-precipitation is the most attractive alternative to mechanical mixing in terms of surface properties, reaction stability, and homogeneity, as well as up-scaling potential. Therefore, it will be the method of choice for the following preparation of different iron-metal oxygen carriers.

Table 4.5: Comparison of the tested preparation methods for the iron-based oxygen carrier supported with 10 wt% alumina.

Characteristics	Co-Precipitation	Citrate Method	Dissolution	Impregnation	Mechanical Mixing
time of preparation	++	++	+	+	+++
scaleability in lab	++	-	++	+++	+++
yield	++	+	+	++	-
homogeneity	+++	++	-	-	+
porosity/surface	++	+	+	++	+++
stability	+++	+	-	++	++
advantages	automatation is possible no nitrose gases	fast evaporation	little preparational effort	little preparational effort	very fast and simple no nitrose gases
disadvantages	higher preparational effort	low educt concentrations nitrose gas formation	slow evaporation nitrose gas formation	slow evaporation nitrose gas formation	
	(+++) very good	(++) good	(+) sufficient	(-) bad	

4.2 Influence of Cerium, Zirconium, and Copper on the iron-based Oxygen Carrier

This section deals with the bimetallic systems consisting of iron with added cerium, zirconium or copper. These additive metals are known for preventing sintering and/or increasing the overall reactivity of the iron-based oxygen carrier. Their influence on the oxygen carrier, which was specifically prepared with co-precipitation, will be discussed in the following chapters. Already an optical difference can be found in figure 4.22, which displays the prepared oxygen carriers.

Figure 4.22: Oxygen Carriers synthesised with Pre. From left to right: Fe-Ce, Fe-Al-Ce, Fe-Zr, Fe-Al-Zr, Fe-Cu, Fe-Al-Cu (16 h), Fe-Al-Cu (3 h)

4.2.1 Oxygen Carrier Composition

For preparing the bimetallic oxygen carrier the amount of additive metal was adjusted to obtain 10 wt% of its oxidised form. These oxides were assumed to be either the most stable ones or are generally known as decomposition product of the precursors that form during precipitation [63, 64].

Table 4.6 lists the metal oxide composition obtained by elementary analysis. Its results correlate to the assumed oxide forms, which can be deduced from the sum of metal oxide of

100 wt%. Since all oxygen carriers were prepared by co-precipitation sodium is also listed in this table. In none of the samples sodium could be detected, which proves a good removal of the precipitating agent during the washing step. While sample Fe-Ce and Fe-Cu equate to determined composition, oxygen carrier Fe-Zr consists of only 0.2 wt% zirconia. In addition this oxygen carrier only reached a yield of 86.3%, which was the result of poor precipitation. Nevertheless the iron-based oxygen carrier did not sinter during calcination at 900 °C. For oxygen carrier Fe-Cu a special characteristic can be found in this table. While the haematite content calculated based on elementary analysis is 89.7 wt% it rises to 95.2 wt% when the TGA value of the first reduction is used. The reason for this deviation is that copper oxide is the only additive metal oxide which can be reduced with hydrogen under given conditions, which of course leads to incorrect results [65].

Table 4.6: Calculated theoretical metal oxide composition based on the metal content obtained by elementary analysis and *on the first reduction during TGA measurement.

sample	yield [%]	$Fe_2O_{3,Red}$* [wt%]	Fe_2O_3 [wt%]	Al_2O_3 [wt%]	CeO_2 [wt%]	ZrO_2 [wt%]	CuO [wt%]	Na [$ng.g^{-1}$]	$\sum$ Metal [wt%]
Fe-Ce	95.3	90.5	91.0	–	9.6	–	–	< 0.2	100.6
Fe-Zr	86.3	99.4	100.1	–	–	0.2	–	< 0.2	100.4
Fe-Cu	95.7	95.2	89.7	–	–	–	10.3	< 0.2	100.0

4.2.2 Stability during cyclic thermo-gravimetric measurement

Results of the thermo-gravimetric analysis are presented in the diagrams in figure 4.23. Only oxygen carrier Fe-Ce (figure 4.23(a)) shows a temporarily stable performance in this series of measurement. Throughout 6 cycles a high conversion could be obtained. During the 7th cycle, however, reduction started to deteriorate and the following oxidation mirrored this slower reaction behaviour towards the end of reaction. From this point on the oxygen carrier continued to lose its conversion capability with each cycle, which was caused by sintering of the iron-based oxygen carrier. The effect of it can be seen in figure 4.24. The loose powder densified and formed a metallic nugget like the haematite sample, which is also included in the figure. In this form, only a very small surface was accessible for the reaction gases, leading to the incomplete conversion during the cycling.

For the sample Fe-Zr the thermo-gravimetric cycling test (figure 4.23(b)) resulted in the sintering of the sample as well. But still the small amount of zirconium seemingly gave a limited stabilisation effect in the very first cycles. Cycles 1 and 2 reached almost complete conversion (99.0% and 98.0%) during oxidation, even-though, the second reduction and following oxidation were slower. Opposed to the cycling test of pure haematite in figure 4.23(d) this is a short-term improvement, which oxygen carrier Fe-Cu could not provide. The sample with copper added (figure 4.26(b)) could not provide one cycle with a complete conversion during oxidation. Already the first reduction is slowing down towards the end. As mentioned in the chapter before copper oxide was reduced besides the iron oxide. This can be clearly seen in the measurement curve 4.23(c) where the weight reduction in the first cycle is lower than the iron level. If the Tammann temperature of copper metal with 541.5 °C is considered, copper is even more likely to sinter than iron at the test temperature of 800 °C and thus could not act as a stabilising metal.

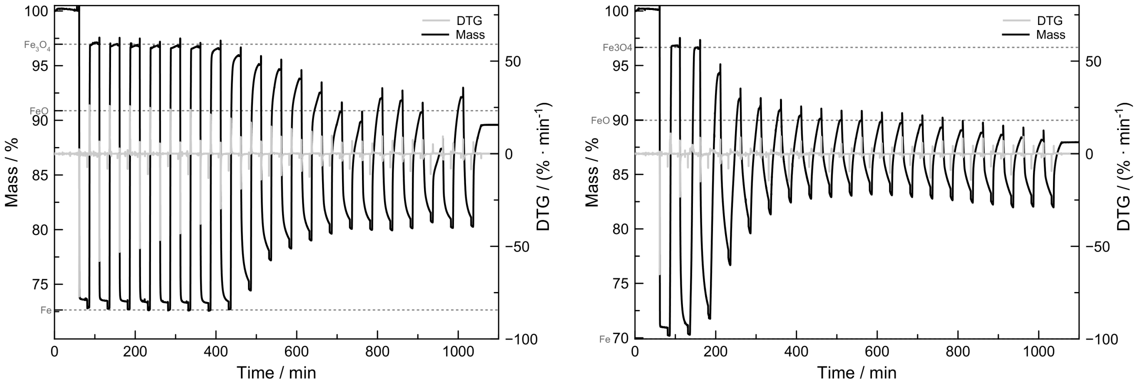

(a) Fe-Ce (b) Fe-Zr

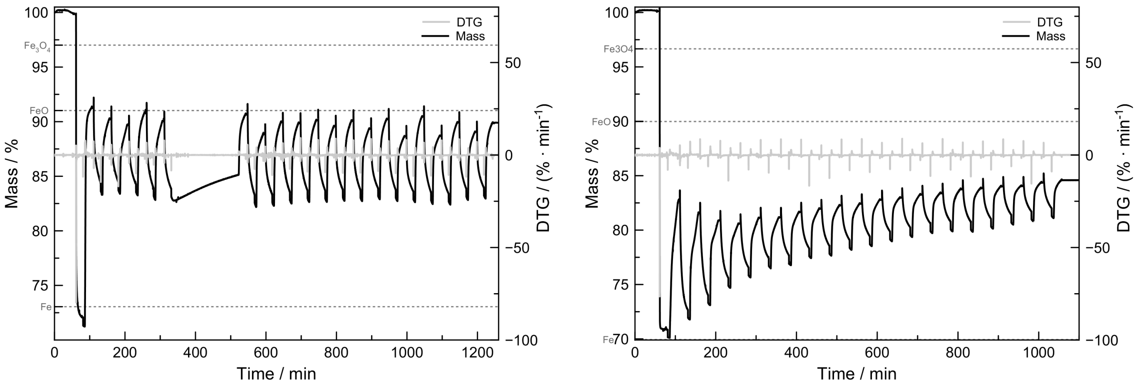

(c) Fe-Cu (d) Unsupported Hematite Powder

Figure 4.23: Results of thermo-gravimetric analysis with 20 cycles of alternating hydrogen reduction and following steam oxidation for the additives cerium, zirconium and copper.

The results illustrate that none of the additive metals could stabilise the iron over 20 cycles. This correlates to the results of Markus Thaler who studied the iron-based oxygen carrier with 10 wt% zirconia as well as cerium oxide prepared by a form of mechanical mixing [25]. Obviously the more homogeneous preparation method could not change the results on the deactivation by sintering.

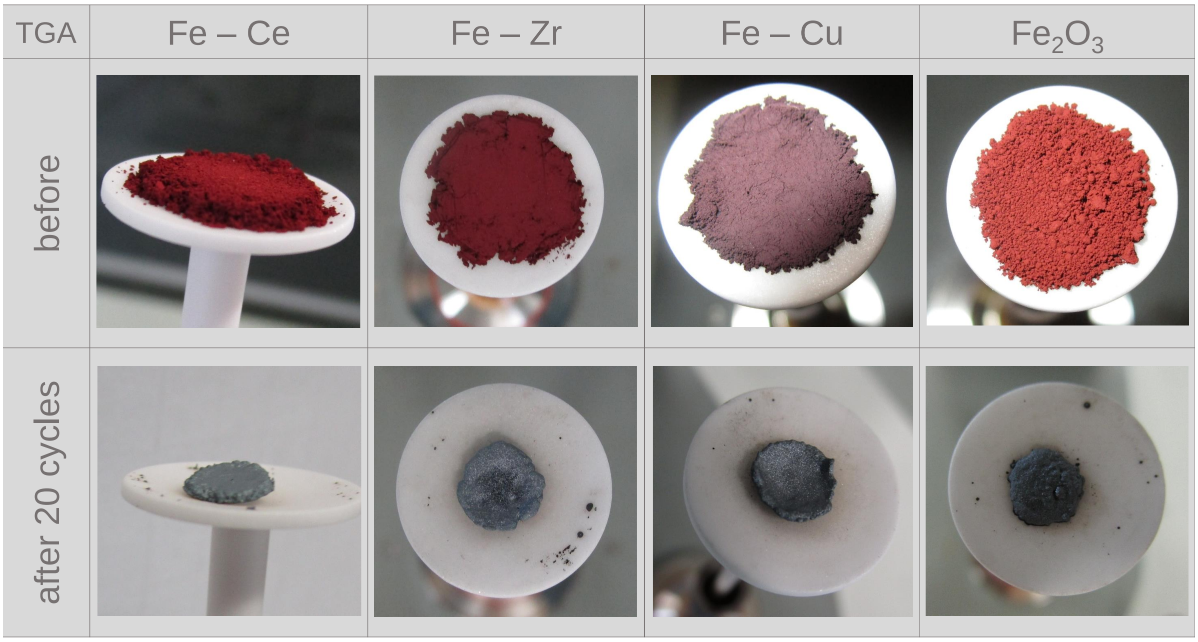

Figure 4.24: The effects of sintering on the oxygen carriers Fe-Ce, Fe-Zr, and Fe-Cu. Pictures taken before and after of the thermo-gravimetric analysis.

4.2.3 Stability of Hydrogen Production

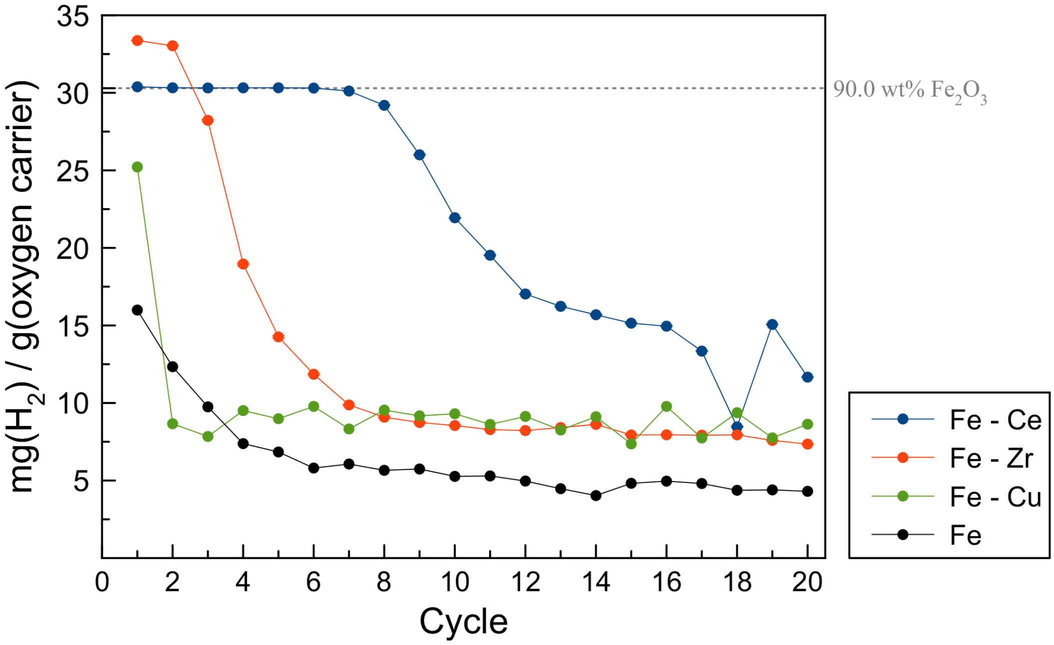

Figure 4.25: Hydrogen production during the oxidation with steam over 20 Cycles.

The specific hydrogen production (see figure 4.25) was calculated for each oxidation step, which represents the aforementioned characteristics. Sample Fe-Ce is the only oxygen carrier which steadily produced 30.3 $\mathrm{mg\,g^{-1}}$ hydrogen up to the 6^{th} oxidation. From then on the curve decreased until hydrogen production only reached half of its starting value with 15.0 $\mathrm{mg\,g^{-1}}$ in the 16^{th} cycle. Oxygen carrier Fe-Zr reached a far higher hydrogen value of 33.4 $\mathrm{mg\,g^{-1}}$. This results from an higher iron content of the sample. However, it deteriorated to only 9.1 $\mathrm{mg\,g^{-1}}$ during the 8^{th} oxidation step, which further diminished to 7.4 $\mathrm{mg\,g^{-1}}$ in the last oxidation. Fe-Cu never reached the maximal theoretical hydrogen production level. After 25.5 $\mathrm{mg\,g^{-1}}$ of hydrogen were produced during the first oxidation, the yield immediately dropped to 8.7 $\mathrm{mg\,g^{-1}}$ in the second cycle. Overall sintering could not be prevented by given metal oxides and hence the produced hydrogen is limited. Only sample Fe-Ce showed a good performance during the first 6 cycles, reaching almost complete oxidation. Nevertheless, after several cycles it deteriorated to a low level.

4.3 Influence of Cerium, Zirconium and Copper on the Alumina supported iron-based Oxygen Carrier

Chapter 4.2 showed that none of the additive metals cerium, zirconium, or copper could stabilise the iron-based oxygen carrier for more than 6 cycles. Nevertheless, those metals are known for promoting effects on the reduction or oxidation behaviour of the iron-based oxygen carrier. Therefore aluminium was added to chosen additive metals in order to give the needed support for study other positive effects of those metals. In addition sample Fe-Al-Cu will be examined for reproducibility of the precipitation step, influence of the calcination time and finally it will be compared to a mechanically mixed sample.

4.3.1 Oxygen Carrier Composition

Table 4.7: Calculated metal oxide composition based on the metal content obtained by elementary analysis and *on the first reduction during TGA measurement.

sample	yield [%]	$Fe_2O_{3,Red}$* [wt%]	Fe_2O_3 [wt%]	Al_2O_3 [wt%]	CeO_2 [wt%]	ZrO_2 [wt%]	CuO [wt%]	Na [$ng.g^{-1}$]	$\sum$ Metal [wt%]
Fe-Al-Ce	96.1	90.3	87.6	4.9	4.7	–	–	< 0.2	97.2
Fe-Al-Zr	91.0	94.0	93.5	5.2	–	0.1	–	< 0.2	98.8
Fe-Al-Cu (16 h)	95.9	93.1	90.0	5.0	–	–	5.2	< 0.2	100.2
Fe-Al-Cu (3 h)	96.3	92.7	88.4	5.0	–	–	5.2	< 0.2	98.6
Fe-Al-Cu (mixed)	–	91.1	86.7	5.7	–	–	7.1	< 0.2	99.6

The amount of aluminium and additive metal was adjusted for each sample to obtain a weight proportion of 5 wt% corresponding to its most stable oxide form as described in chapter 4.2. Overall yields of the co-precipitation were high with over 95% for all oxygen carriers but Fe-Al-Zr. Once again, zirconium could not be precipitated well enough to obtain 5 wt% of ZrO_2. Just 2 wt% of the intended amount of zirconium oxide could be found during elementary analysis. Oxygen carrier Fe-Al-Cu was prepared twice in order to control the repeatability of the precipitation method. In contrast to Fe-Al-Zr the metal composition shows that co-precipitation could integrate almost the same amount of additive metals repeatedly. Hence it is likely that the chosen pH-value for the zirconium containing oxygen carrier could not precipitate the zirconium. For the zirconium iron system a higher pH value of 10 was found for the co-precipitation process [66]. Clearly the conditions of co-precipitation for the metal mixture must be studied before synthesis. In Literature titration is used to determine the point of pH where metal systems precipitate [67]. However not every metal mixture can be co-precipitated homogeneously as a result of different pH-values for precipitation [31]. Therefore, a titration analysis can evaluate applicability for different metal systems.

4.3.2 Stability of Hydrogen Production

During thermo-gravimetric cyclic analysis all oxygen carriers were well stabilised, as diagrams in figure 4.26 show.

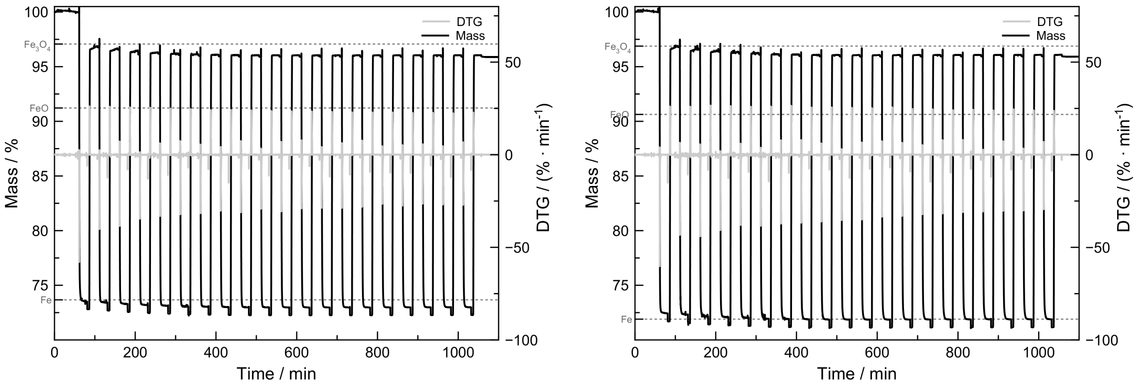

(a) Fe-Al-Ce

(b) Fe-Al-Zr

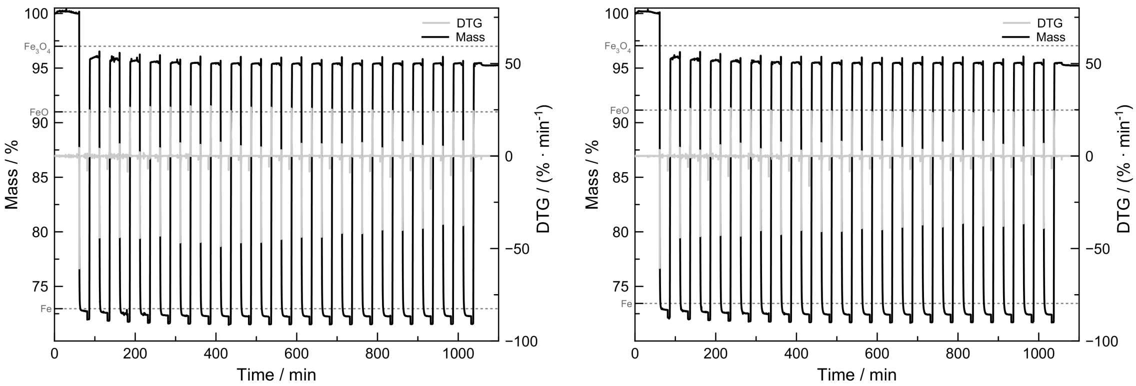

(c) Fe-Al-Cu (16 h)

(d) Fe-Al-Cu (3 h)

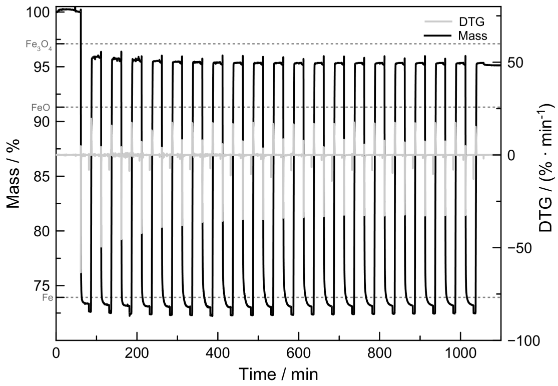

(e) Fe-Al-Cu (V33, mechanically mixed)

Figure 4.26: Results of thermo-gravimetric analysis with 20 cycles of alternating hydrogen reduction and following steam oxidation for the additves cerium, zirconium and copper with added alumina.

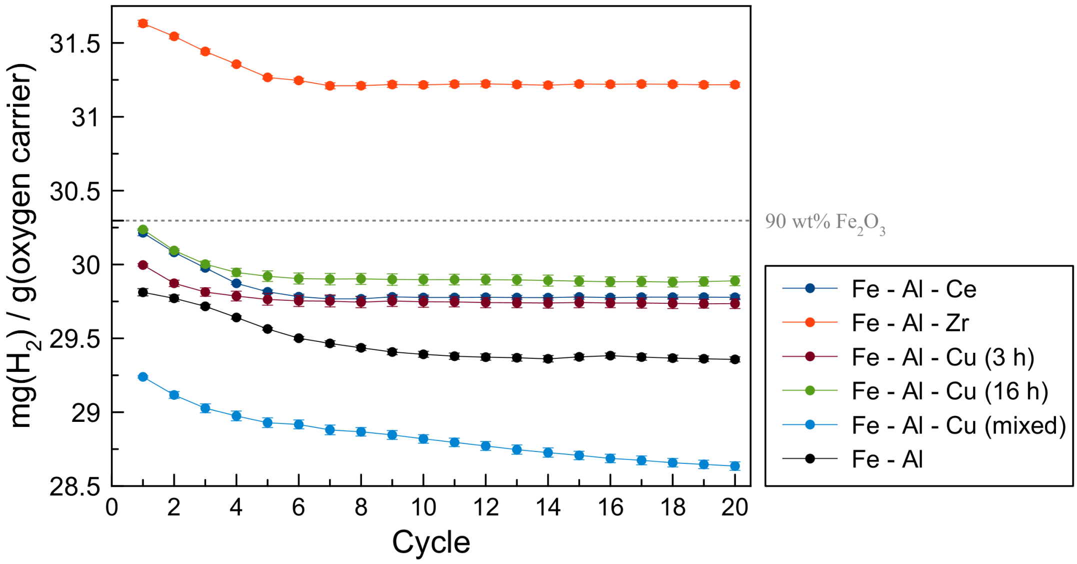

Figure 4.27: Specific hydrogen production of iron-based oxygen supported by alumina and additional metals cerium, zirconium, and copper.

Neither the lower amount of aluminium, nor the addition of a second metal did deteriorate the hydrogen production stability (see figure 4.27). In general all oxygen carriers prepared by the co-precipitation method yielded a high and constant amount of hydrogen over 20 cycles. Solely the mechanically mixed oxygen carrier Fe-Al-Cu (mixed) provided a lower productivity, which further deteriorated with each cycle until only 28.6 mg g^{-1} were reached in the last cycle. This continuous decrease was already observed for the mechanically mixed oxygen carrier in figure 4.15, which depicts the oxygen conversion of the samples prepared by different routes of synthesis. All samples prepared by co-precipitation had a similar progress during hydrogen production; at first a fast deterioration decreased the yield, which is then followed by a extremely stable phase up to twenty cycles. Oxygen carriers with Cu stabilised after the 4^{th} cycle, while Ce and Zr stabilised after the 6^{th} cycle. Derived from this, it can be confirmed that the more homogeneous wet chemically prepared samples are favourable for oxygen carriers with further additives.

Overall, the addition of a second additive metal enhanced hydrogen yield of the iron-based oxygen carriers during the oxidation phase. During the 20^{th} oxidation, all samples with a second additive metal surpassed the hydrogen yield of the sample with only alumina added (29.35 mg g^{-1}). According to the iron content Fe-Al-Ce performs slightly better than the samples with added Cu, which could be the result of Ce taking part in the red-ox reaction ($\mathrm{Ce}^{3+} \rightleftharpoons \mathrm{Ce}^{4+}$). Fe-Al-Ce and Fe-Al-Cu (3 h) both reach a specific hydrogen yield of 29.75 mg g^{-1} in the final cycle. Sample Fe-Al-Cu (16 h) with 29.90 mg g^{-1} surpassed the value of Fe-Al-Ce (3 h), which can be explained by a higher iron content. This is also the reason why Fe-Al-Zr generated the highest hydrogen yield during oxidation. With w(Fe_2O_3)=93.5 wt% this oxygen carrier surpassed the line of the theoretical possible hydrogen production of oxygen carriers with 90 wt% haematite, which is plotted in the diagram. The high stability of all oxygen carriers demonstrates that half of the supporting alumina was enough to inhibit sintering.

Since oxygen carrier Fe-Cu copper severally deteriorated during cyclisation (see figure 4.25), the effect of high temperature on the copper-added, iron-based oxygen carrier with alumina was investigated. Two separately prepared Fe-Al-Cu oxygen carriers were calcinated for two different lengths of time (3h and 16h). Yet, the extension of time did not have an apparent effect on hydrogen production. The main difference in their performance is the amount of produced hydrogen. This shift, however, can be explained by the varying amount of iron. The iron content of the oxygen carriers suggests a theoretical value of 0.14 $mg\,g^{-1}$, which is closely met with the experimental data that result in a shift of around 0.15 $mg\,g^{-1}$. Otherwise both samples have a resembling progression of hydrogen production over time, showing the same deactivation behaviour.

4.3.3 Change of Reactivity during the Reduction and Oxidation Process

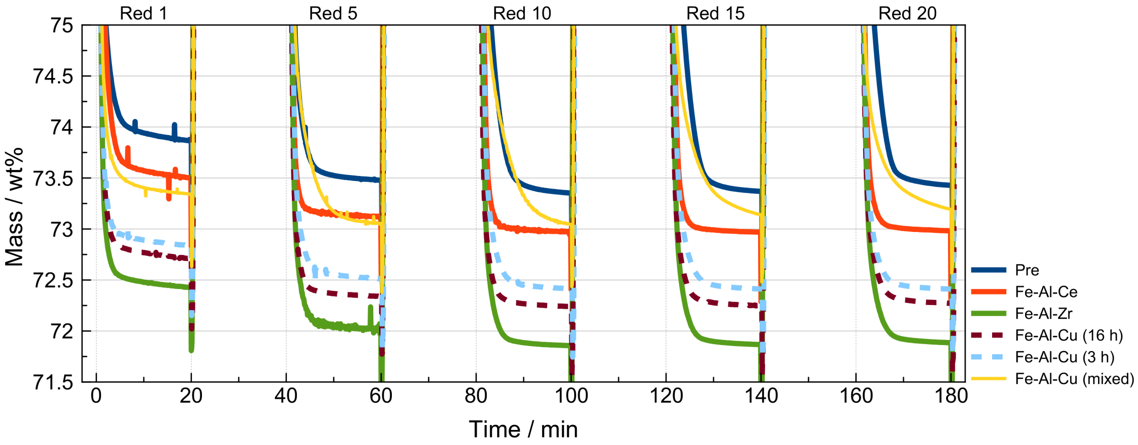

Figure 4.28: Detail of the reduction progress of selected cycles of the oxygen carriers with alumina and the additive metal: cerium, zirconium, copper

For comparison of the reaction progress cycles 1, 5, 10, 15 and 20 were selected and superimposed in the diagrams of figure 4.28 and 4.29. Figure 4.28 compares the reduction progress of the oxygen carriers including sample Pre, which only contained alumina (10 wt%). All samples show a better reducibility than sample Pre. Oxygen carrier Fe-Al-Cu (mixed) is the only sample which underwent a slow and over the cycles deteriorating reduction progress. As a result of the slow reduction rate it could not completely reduce in the given amount of time. This behaviour, which is worse than for the mechanically mixed oxygen carrier with 10 wt% Al_2O_3, might be caused by inhomogeneity. It is to presume that the single copper particles sintered after reduction and hence promoted the loss of reactive surface area, by e.g. closing pores or promoting sinter process of iron by building sintering necks.

Oxygen carrier Pre also decelerated at an comparably early stage. This behaviour slightly deteriorated towards the middle of red-ox cycling, as discussed in the chapter before. None of the other co-precipitated oxygen carriers with cerium, zirconium, or copper showed this progress during reduction. In general sample Fe-Al-Ce possesses the most stable reduction behaviour. It was steadily reduced under 10 minutes. Hereby cerium is known to promote reduction by increasing the oxygen conductivity through the lattice. It builds vacancies in the lattice, which helps oxygen diffusion through the solid [36]. Therefore cerium oxide might counteract the negative effect of aluminium on the oxygen conductivity, which slows down diffusion through the tighter hercynite lattice. Oxygen carrier Fe-Al-Cu also provided a faster reduction than Pre. Interestingly the oxygen carrier which was calcined for 16 h showed a slightly faster reduction than the one only calcined for 3 hours. However it decelerated in the 20^{th} cycle, where its speed of reduction equalized the other oxygen carrier. Although zirconium is only known for improving the oxidation of iron with steam, the reduction process was almost as fast as for the other oxygen carriers [25, 35]. A reason for this can be the formation of defects by the integration of foreign metal atoms into the iron oxide lattice, which can increase oxygen conductivity by generating vacancies. Another reason could be an overall beneficial effect of a lower amount of aluminium on the reduction, which also could have had a positive effect for the reduction of the other oxygen carriers. Therefore, the examination of lower alumina concentration for support might bring good results for the overall performance of the iron-based oxygen carrier.

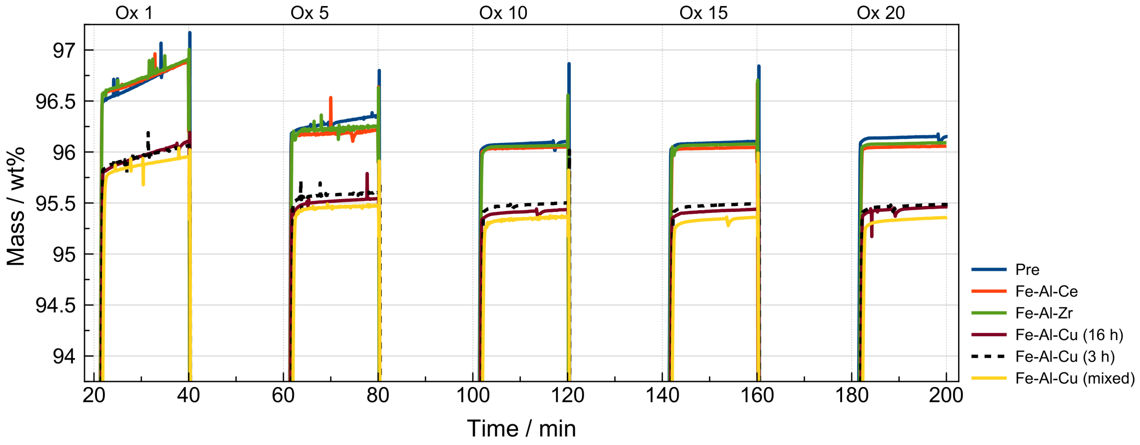

Figure 4.29: Detail of the oxidation progress of selected cycles of the oxygen carriers with alumina and additive metal: cerium, zirconium, copper

All oxygen carriers possessed a fast oxidation behaviour, just like the Pre. Only Fe-Al-Cu (mixed) slightly slowed down during oxidation while the reduction deteriorated significantly. As a result of its reducibility under hydrogen copper containing samples show a lower oxidation state than the other samples.

A striking feature for all oxygen carriers is the first oxidation (only for Pre also seen in the 5^{th} cycle) each sample shows a linear increase after the bend of the first and fast oxidation phase. The slope is much smaller but still linear leading to an unfinished oxidation. The exact reason could not be determined by the analysis methods made for this work. But certainly the oxygen carrier underwent major structural changes during the first cycles. One possible explanation is sintering which led to coagulation of the small grains on the particle. This resulted in bigger grains, which gave space for a higher porosity as discussed in chapter 4.1. Hereby smaller pores could be eliminated, which might have a rate limiting effect. Another reason is the formation of solid solution and compounds like hercynite, which might need several cycles for formation.

4.3.4 Surface Properties of the Cerium - Alumina supported Oxygen Carrier

Oxygen carrier Fe-Al-Ce showed interesting properties during thermo-gravimetric analysis, because the cerium oxide contributed to the redox process in contrast to alumina, zirconia and copper(II)oxide. Therefore further examinations were conducted on this sample to evaluate its homogeneity and surface structure.

Scanning Electron Microscopy

Investigations on the surface structure by scanning electron microscopy display agglomerates which consist of fine grains about 30 nm in size. Comparison to the oxygen carrier Pre, which was only supported by aluminium, found that the addition of cerium resulted in the reduction of grain-size in about a factor of 5. Even though smaller grains led to an increase in surface, which is favourable for the redox reaction process, it facilitated sintering during the post-preparation step. In figure 4.30(c) all grains are in a progressed state of sintering. Grain growth and loss of inter-granular room are clearly visible. Nevertheless, bigger pore cavities still provided room for the exchange of reaction and product gases from the particle interior. An overall EDX of figure 4.30(c) reveals a well distributed composition which goes along with the elementary analysis with 3.3 wt% of aluminium and 6 wt% of cerium.

Images of the sample taken after redox cycling depict major structural changes. The formerly small grains grew to a size of about 500 nm interconnecting with strongly developed necks. This structure leads to more interparticle space and a higher porosity. The biggest change however, are the small precipitated particle-agglomerates around the main structure. EDX, as seen in figure 9.5(e) indicate a significantly higher cerium content than in the surrounding material

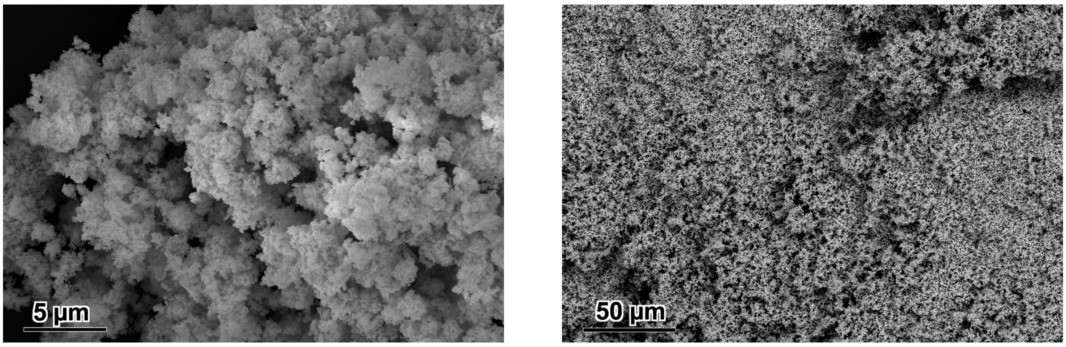

(a) A single particle of the fresh oxygen carrier.

(b) A single particle after 20 cycles of TGA-measurement.

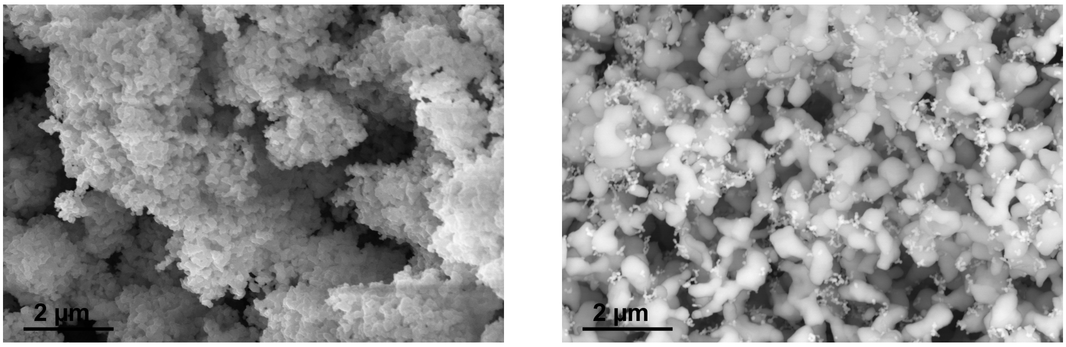

(c) Surface detail of the fresh oxygen carrier.

(d) Detail of the surface structure after 20 redox cycles.

Figure 4.30: SEM pictures of the oxygen carrier supported with cerium and aluminium.

(9.5(f)). A more detailed composition analysis was not feasible because of the small dimension of the precipitates, which may have caused misleading results by scattering effects.

Mercury Intrusion Porosimetry

Analysis performed by mercury intrusion porosimetry reflect the results of SEM images. Table 4.8 compares the obtained values for the aluminium oxygen carrier prepared by co-precipitation with the oxygen carrier Fe-Al-Ce with a specific surface area of $7.7\,\mathrm{m^2\,g^{-1}}$ and total porosity of 80.3%. The addition of Ce distinctly increased surface and porosity, which relates to the smaller grains within the agglomerates. This highly increased total porosity can also be found in the oxygen carrier Fe-Ce, but this positive effect does not relate to the specific surface. The pore diameter distribution in figure 4.32 clarifies this behaviour. Porosity results from a broader pore diameter range than in other oxygen carriers, starting at a high pore diameter, which can be also seen in figure 4.30(a). This might be the effect of a stronger agglomeration by small grains. Hysteresis curve of Fe-Al-Ce does not indicate enclosed mercury.

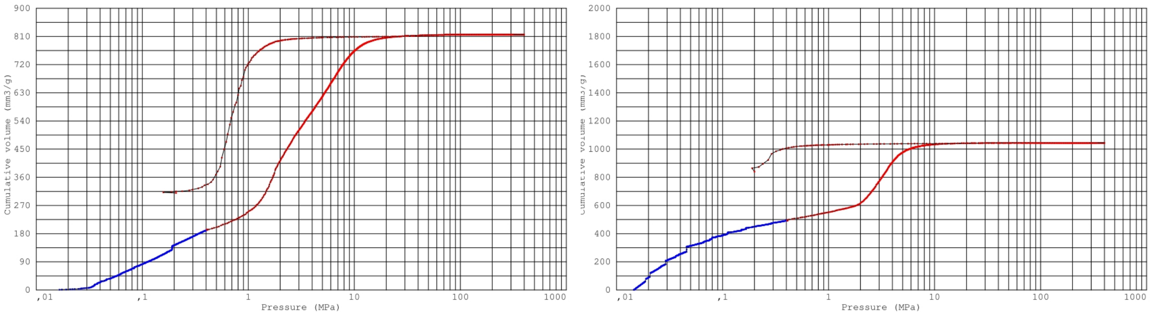

(a) Intrusion and extrusion curves of the oxygen carrier Fe-Al-Ce.

(b) Intrusion and extrusion curves of the oxygen carrier Fe-Ce.

Figure 4.31: Pore diameter distribution of oxygen carriers Fe-Al-Ce and Fe-Ce.

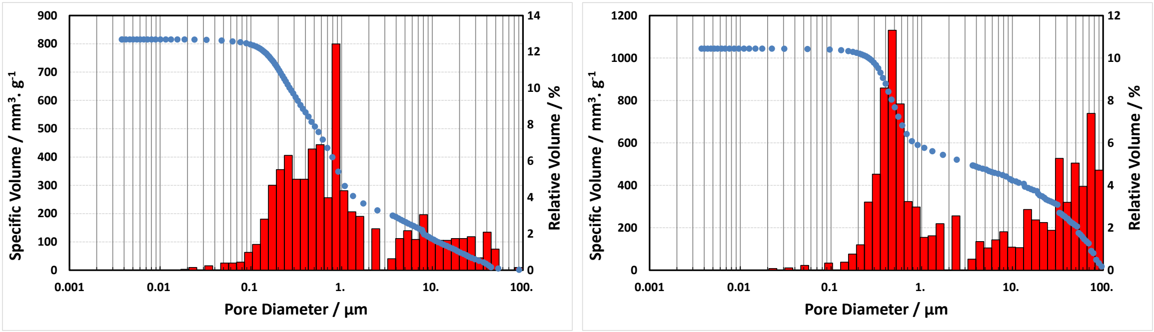

(a) Pore diameter distribution of the oxygen carrier Fe-Al-Ce.

(b) Pore diameter distribution of the oxygen carrier Fe-Ce.

Figure 4.32: Mercury intrusion curve of oxygen carriers Fe-Al-Ce and Fe-Ce.

Table 4.8: Values of surface properties for the Fe-Ce samples obtained by mercury intrusion porsimetry.

	Precipitation	**Mechanical Mixing**	**Fe-Ce**	**Fe-Al-Ce**
Total cumulative volume [$mm^3\ g^{-1}$]	295.4	362.3	1044.5	815.4
Total specific surface area [$mm^2\ g^{-1}$]	6.6	7.9	5.1	7.7
Average pore diameter [µm]	34.3	0.2	0.5	0.8
Total porosity [%]	39.0	49.4	86.9	80.3
Bulk density [$g\ cm^{-3}$]	1.3	1.4	0.8	1.0
Apparent density [$g\ cm^{-3}$]	2.2	2.7	6.4	5.0

5 Conclusion and Outlook

In this work five preparation methods – co-precipitation, citrate method, dissolution, impregnation and mechanical mixing – were compared by preparing iron-based oxygen carriers with 10 wt% of alumina as support.The obtained results showed that only co-precipitation could provide an oxygen carrier, which possessed a stable oxidation behaviour towards the end of repeated red-ox cycling. It also stands out with a good homogeneity before and after repeated oxidation and reduction. Although the other samples lacked in homogeneity before the cycling tests, they partly could improve during the thermo-gravimetric measurement. This 'activation process' also increased the apparent porosity, which can be favourable for gas diffusion.

After choosing co-precipitation as most appropriate preparation method, the effect of the addition of other metals was tested. For this the metals cerium, zirconium and copper with and without aluminium were added. It showed that none of the metals, without the addition of aluminium, could prevent sintering over a higher number of cycles. Oxygen carrier Fe-Ce supported a high and stable hydrogen yield of about 30.3 $\mathrm{mg\,g^{-1}}_{\mathrm{OC}}$ for 6 cycles. Only aluminium provided the stabilisation of the iron-based oxygen carrier needed to study the positive effects of the other additive metals. Oxygen carrier Fe–Al–Ce and Fe–Al–Cu showed a significant improvement in the reduction speed compared with the co-precipitated oxygen carrier Fe–Al (Pre). They both show a faster reduction behaviour and yielded a higher amount of hydrogen during oxidation with 29.8 and 29.9 $\mathrm{mg\,g^{-1}}_{\mathrm{OC}}$ compared to 29.4 $\mathrm{mg\,g^{-1}}_{\mathrm{OC}}$. Furthermore it could be found that the stability of hydrogen production decreased in a pattern for the co-precipitated oxygen carriers. After a rapid deterioration of the yield within the first cycles, the hydrogen production became stable in the following cycles. In contrast to the co-precipitated sample, the mechanically mixed sample Fe-Al-Cu (mixed) constantly deteriorated. This is a result of a decelerating reduction, which is assumed to be caused of sintering copper particles.

Despite the good results obtained by cerium and copper containing oxygen carriers concerning the co-precipitation method, zirconium showed its drawbacks. Hardly any of the metal could be precipitated, which is an issue if different metals are not precipitated at the same pH value. In contrast to this, the intended metal compositions for oxygen carrier Fe-Al (Pre), Fe-Ce, Fe-Cu, Fe-Al-Ce and Fe-Al-Cu were achieved. Oxygen carrier Fe-Al-Cu, which was prepared twice, showed a good reproducibility of the composition.

To increase the amount of hydrogen yield per cycle and to reduce the costs caused by the more expensive additive metals it would be of interest to lower the amount of alumina and further additive metals. Also a combination of different preparation methods might be favourable. Since the impregnated sample showed the slowest deterioration during hydrogen production a homogeneous precipitation with a following impregnation step might have a positive effect.

6 References

[1] Jan Willem Erisman et al. “How a century of ammonia synthesis changed the world”. In: *Nature Geoscience* 1 (2008), pp. 636–639.

[2] European Commission and Directoraten General for Research and Innovation. *HyWays: The European hydrogen roadmap*. Luxembourg, 2008. arXiv: `EUR23123`.

[3] Commission of the European Communities. *Communication from the Commission to the Council, the European Parliament, the European economic and social Committee and the Committee of the regions: A European strategic energy technology plan (SET-PLAN)*. Brussels, 2007.

[4] United Nations. *United Nations Framework Convention on Climate Change*. New York, 1992.

[5] United Nations. *Kyoto Protocol To the United Nations Framework Kyoto Protocol To the United Nations Framework*. Kyoto, 1998.

[6] Ken-ichiro Ota. “Environmental impact factor for hydrogen energy”. In: *Advanced Studies of Polymer Electrolyte Fuel Cells 8th International Summer School*. Ed. by Shigenori Mitsushima et al. Yokohama, 2015, pp. 11–19.

[7] Liang Shih Fan. *Chemical Looping Systems for Fossil Energy Conversions*. New Jersey: John Wiley & Sons, Inc., 2010.

[8] Viktor Hacker. “A novel process for stationary hydrogen production: The reformer sponge iron cycle (RESC)”. In: *Journal of Power Sources* 118.1-2 (2003), pp. 311–314.

[9] Stephan Nestl et al. “The production of pure pressurised hydrogen by the reformer-steam iron process in a fixed bed reactor system”. In: *Journal of Power Sources* 280 (2015), pp. 57–65.

[10] M. F. Bleeker, H. J. Veringa, and S. R. Kersten. “Deactivation of iron oxide used in the steam-iron process to produce hydrogen”. In: *Applied Catalysis A: General* 357.1 (2009), pp. 5–17.

[11] Viktor Hacker et al. “Hydrogen production by steam-iron process”. In: *Journal of Power Sources* 86 (2000), pp. 531–535.

[12] Viktor Hacker et al. “Usage of biomass gas for fuel cells by the SIR process”. In: *Journal of Power Sources* 71.1-2 (1998), pp. 226–230.

[13] Gernot Voitic et al. “Pressurized hydrogen production by fixed-bed chemical looping”. In: *Applied Energy* 157 (2015), pp. 399–407.

[14] Franz Oeters et al. “Iron”. In: *Ullmann’s Encyclopedia of Industrial Chemistry*. Weinheim, Germany: Wiley-VCH Verlag GmbH & Co. KGaA, 2006, pp. 1–177.

[15] J. W. Geus. “Preparation and Properties of Iron Oxide and Metallic Iron Catalysts.” In: *Applied Catalysis* 25 (1986), pp. 313–333.

[16] Ashriti Govender, Daniel Curulla Ferre, and J. W. Niemantsverdriet. “The Surface Chemistry of Water on Fe(100): A Density Functional Theory Study”. In: *ChemPhysChem* 13.6 (2012), pp. 1583–1590.

[17] Chenggang Zhou et al. “Density functional theory study of water dissociative chemisorption on the Fe3O4(111) surface”. In: *Journal of Physical Chemistry C* 114.49 (2010), pp. 21405–21410.

[18] Juntao Yuan et al. “Comparison between the oxidation of iron in oxygen and in steam at 650–750°C”. In: *Corrosion Science* 75 (2013), pp. 309–317.

[19] Fumihiko Kosaka et al. “Iron oxide redox reaction with oxide ion conducting supports for hydrogen production and storage systems”. In: *Chemical Engineering Science* 123 (2015), pp. 380–387.

[20] Piran R. Kidambi et al. “Interaction of iron oxide with alumina in a composite oxygen carrier during the production of hydrogen by chemical looping”. In: *Energy and Fuels* 26.1 (2012), pp. 603–617.

[21] Vladimir Galvita et al. “Deactivation of modified iron oxide materials in the cyclic water gas shift process for CO-free hydrogen production”. In: *Industrial and Engineering Chemistry Research* 47.2 (2008), pp. 303–310.

[22] *Alfa Aesar. Chemical data sheets. http://www.alfa.com (accessed Sep 19, 2015).*

[23] Hermann Salmang and Horst Scholze. *Keramik*. Ed. by Rainer Telle. 7th. Vol. 53. 7. Berlin - Heidelberg: Springer Berlin Heidelberg, 2007, p. 628.

[24] Julian Szekely, James W. Evans, and Hong Yong Sohn. *Gas-solid reactions*. New York: Academic Press, INC., 1976, p. 400.

[25] Markus Thaler. “Kontaktmassenentwicklung für den Metall-Dampf-Prozess zur Erzeugung und Speicherung von Wasserstoff für Brennstoffzellen”. PhD thesis. Technical University of Graz, 2009.

[26] G. R. Smolik et al. “Hydrogen generation from steam reaction with tungsten”. In: *Journal of Nuclear Materials* 258-263 (1998), pp. 1979–1984.

[27] G.R. Smolik et al. “Oxidation and volatilization from tungsten brush high heat flux armor during steam exposure”. In: *Fusion Engineering and Design* 54.3-4 (2001), pp. 583–591.

[28] Sakae Takenaka et al. “Production of pure hydrogen from methane mediated by the redox of Ni- and Cr-added iron oxides”. In: *Journal of Catalysis* 228.2 (2004), pp. 405–416.

[29] Sakae Takenaka et al. “Storage and supply of hydrogen by means of the redox of the iron oxides modified with Mo and Rh species”. In: *Journal of Catalysis* 228.1 (2004), pp. 66–74.

[30] Agnieszka Marta Kierzkowska et al. “Development of Iron Oxide Carriers for Chemical Looping Combustion Using SolGel”. In: *Industrial & Engineering Chemistry Research* 49.11 (2010), pp. 5383–5391.

[31] Christopher Bohn. “The Production of Pure Hydrogen with Simultaneous Capture of Carbon Dioxide”. PhD. University of Cambridge, 2010, pp. 1–232.

[32] Jae Chun Ryu et al. “Effect of additives on redox behavior of iron oxide for chemical hydrogen storage”. In: *Journal of Industrial and Engineering Chemistry* 14.2 (2008), pp. 252–260.

[33] F. Al-Raqom and J. F. Klausner. “Reactivity of Iron/Zirconia Powder in Fluidized Bed Thermochemical Hydrogen Production Reactors”. In: *Journal of Energy Resources Technology* 136.1 (2013).

[34] K. Otsuka et al. “Hydrogen storage and production by redox of iron oxide for polymer electrolyte fuel cell vehicles”. In: *International Journal of Hydrogen Energy* 28.3 (2003), pp. 335–342.

[35] Kohei Urasaki et al. “Hydrogen production via steam-iron reaction using iron oxide modified with very small amounts of palladium and zirconia”. In: *Applied Catalysis A: General* 288.1-2 (2005), pp. 143–148.

[36] Fang Liu et al. “Cerium oxide promoted iron-based oxygen carrier for chemical looping combustion”. In: *Industrial and Engineering Chemistry Research* 53.42 (2014), pp. 16341–16348.

[37] Doki Yamaguchi et al. “Redox Performance of Modified Iron Oxides for Hydrogen Production”. In: *Novel Gas Conversion Symposium 9, Lyon, France, 30 May - 4 June*. Elsevier, 2011, CDROM. arXiv: `EP104464`.

[38] Lei Guo et al. “Comparison of Large-Scale Production Methods of Fe2O3/Al2O3 Oxygen Carriers for Chemical-Looping Combustion”. In: *Chemical Engineering and Technology* 37.7 (2014), pp. 1211–1219.

[39] Juan Adanez et al. “Development of oxygen carriers for chemical-looping combustion - Results from the CO2 Capture Project Capture”. In: *Carbon Dioxide Capture for Storage in Deep Geologic Formations*. Ed. by D.C. Thomas and S.M. Benson. 1st. Vol. 1. Oxford: ELSEVIER Ltd, 2005. Chap. 34, pp. 587–604.

[40] Sung R. Son and Sang D. Kim. “Chemical-Looping Combustion with NiO and Fe2O3 in a Thermobalance and Circulating Fluidized Bed Reactor with Double Loops”. In: *Industrial & Engineering Chemistry Research* 45.8 (2006), pp. 2689–2696.

[41] B. Moghtaderi and H. Song. “Reduction Properties of Physically Mixed Metallic Oxide Oxygen Carriers in Chemical Looping Combustion”. In: *Energy & Fuels* 24.10 (2010), pp. 5359–5368.

[42] Tobias Mattisson et al. “Chemical-looping combustion using syngas as fuel”. In: *International Journal of Greenhouse Gas Control* 1.2 (2007), pp. 158–169.

[43] Fang He, Hua Wang, and Yongnian Dai. “Application of Fe2O3/Al2O3 Composite Particles as Oxygen Carrier of Chemical Looping Combustion”. In: *Journal of Natural Gas Chemistry* 16 (2007), pp. 155–161.

[44] C. D. Bohn et al. “Stabilizing Iron Oxide Used in Cycles of Reduction and Oxidation for Hydrogen Production”. In: *Energy & Fuels* 24.7 (2010), pp. 4025–4033.

[45] Haibo Zhao et al. “Comparison of preparation methods for iron-alumina oxygen carrier and its reduction kinetics with hydrogen in chemical looping combustion”. In: *Asia-Pacific Journal of Chemical Engineering* 9.4 (2014), pp. 610–622.

[46] Hongguang Jin, Toshihiro Okamoto, and Masaru Ishida. “Development of a Novel Chemical-Looping Combustion: Synthesis of a Solid Looping Material of NiO/NiAl2O4”. In: *Industrial & Engineering Chemistry Research* 38.1 (1999), pp. 126–132.

[47] P. G. Menon and B. Delmon. “Solid-State Reactions”. In: *Preparation of Solid Catalysts*. Ed. by Gerhard Ertl, Helmut Knözinger, and Jens Weitkamp. Weinheim, Germany, 2008. Chap. 3.7.

[48] David Ward and Edmond Ko. “Preparing Catalytic Materials by the Sol-Gel Method”. In: *Industrial & Engineering Chemistry Research* 34.2 (1995), pp. 421–433.

[49] Jitka Kirchnerova, Mihai Alifanti, and Bernard Delmon. “Evidence of phase cooperation in the LaCoO3 – CeO2 – Co3O4 catalytic system in relation to activity in methane combustion”. In: *Applied Catalysis A: General* 231 (2002), pp. 65–80.

[50] E. Lorente, J. A. Pena, and J. Herguido. “Separation and storage of hydrogen by steam-iron process: Effect of added metals upon hydrogen release and solid stability”. In: *Journal of Power Sources* 192.1 (2009), pp. 224–229.

[51] Masaru Ishida, Hongguang Jin, and Toshihiro Okamoto. “A Fundamental Study of a New Kind of Medium Material for Chemical-Looping Combustion”. In: *Energy & Fuels* 10.4 (1996), pp. 958–963.

[52] Masaru Ishida, M Yamamoto, and T. Ohba. “Experimental results of chemical-looping combustion with NiO/NiAl2O4 particle circulation at 1200 °C”. In: *Energy Conversion and Management* 43.9-12 (2002), pp. 1469–1478.

[53] Masaru Ishida, Hongguang Jin, and Toshihiro Okamoto. “Kinetic Behavior of Solid Particle in Chemical-Looping Combustion: Suppressing Carbon Deposition in Reduction”. In: *Energy & Fuels* 12.2 (1998), pp. 223–229.

[54] Bernhard Marius. “Investigation and characterization of contact mass stability for the reversible steam-iron process for production, storage and purification of hydrogen”. Master’s thesis. Graz University of Technology, 2015.

[55] Thermo Scientific. *Thermo Scientific Pascal Series Mercury Porosimeter*. Milan.

[56] Porotec. *Theorie der Auswertemodelle in der SOLID-Software*.

[57] Stephan Nestl, Gernot Voitic, and Viktor Hacker. “Investigations of the Steam Iron Process for Decentralised Renewable Hydrogen Production”. In: *4th European PEFC And H2 Forum 2013* July (2013), p. 2013.

[58] Michael Lammer. “Investigations on generation of ultra-pure hydrogen by the steam-iron process using a tubular reactor system”. Master’s thesis. Technical University Graz, 2014.

[59] S. Lowell et al. *Characterization of Porous Solids and Powders-Surface Area, Pore Size and Density*. 1st ed. Dordrecht: Kluwer Academic Publishers, 2004, pp. 157–188.

[60] Peter Klobes, Klaus Meyer, and Ronald G. Munro. *Practice Guide: Porosity and Specific Surface Area Measurements for Solid Materials*. Special Pu. Washington: National Institute of Standards and Technology, 2006, p. 89.

[61] A. Cabello et al. “Kinetic determination of a highly reactive impregnated Fe2O3/Al2O3 oxygen carrier for use in gas-fueled Chemical Looping Combustion”. In: *Chemical Engineering Journal* 258 (2014), pp. 265–280.

[62] Nobukazu Shigematsu and Hikoya Iwai. “Effect of SiO2 and/or Al2O3 addition on reduction of dense wustite by hydrogen.” In: *Transactions of the Iron and Steel Institute of Japan* 28.3 (1988), pp. 206–213.

[63] Arnold Hollemann and Nils Wiberg. *Lehrbuch der Anorganischen Chemie*. 101. Berlin: Walter de Gruyter, 1995.

[64] ROEMPP Redaktion and Helmut Sitzmann. *https://roempp.thieme.de/roempp4.0/do/data/RD-11-02453 (accessed: Feb 6, 2016).*

[65] Jae Y Kim et al. “Reduction of CuO and Cu2O with H2: H Embedding and Kinetic Effects in the Formation of Suboxides”. In: *Journal of the American Chemical Society* 125 (2003), pp. 10684–10692.

[66] Wen Liu, John S. Dennis, and Stuart A. Scott. “The Effect of Addition of ZrO2 to Fe2O3 for Hydrogen Production by Chemical Looping”. In: *Industrial & Engineering Chemistry Research* 51.51 (2012), pp. 16597–16609.

[67] Malte Behrens et al. “Understanding the complexity of a catalyst synthesis: Co-precipitation of mixed Cu,Zn,Al hydroxycarbonate precursors for Cu/ZnO/Al2O3 catalysts investigated by titration experiments”. In: *Applied Catalysis A: General* 392.1-2 (2011), pp. 93–102.

7 List of Figures

8 List of Tables

9 Appendix

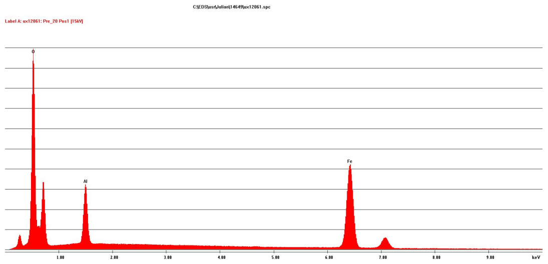

Figure 9.1: EDX of oxygen carrier Pre in figure 4.3(b).

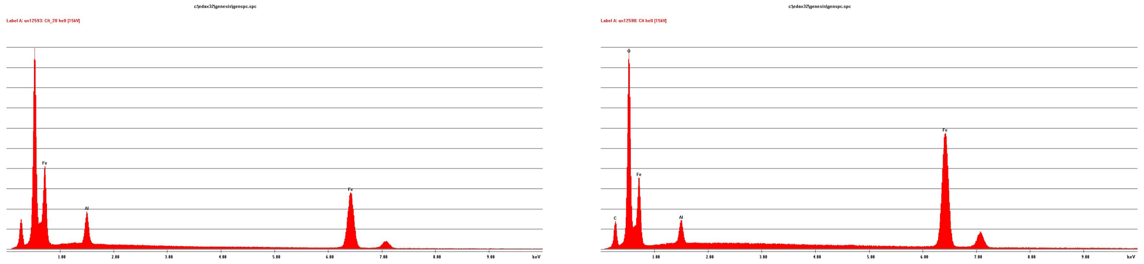

(a) EDX of figure 4.5(d)

(b) EDX of figure 4.5(e).

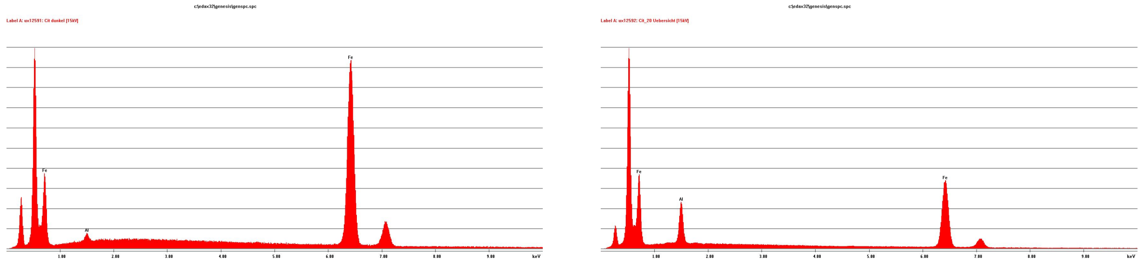

(c) EDX of figure 4.5(f)

(d) EDX of figure 4.5(g)

Figure 9.2: EDX spectra of the oxygen carrier Cit.

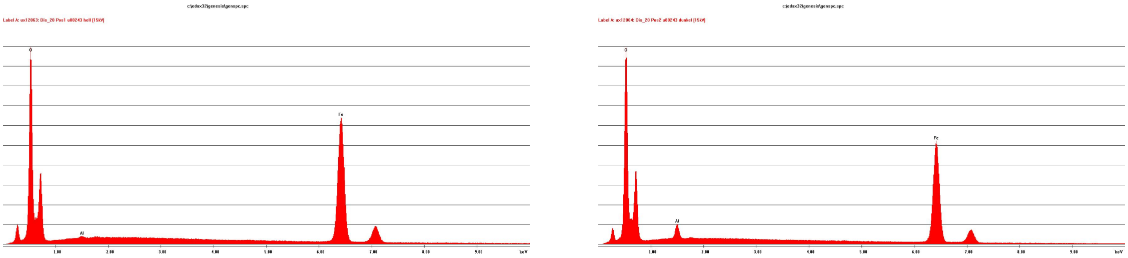

(a) Structure C of figure 4.7(e)

(b) Structure D of figure 4.7(f)

Figure 9.3: EDX spectra of the significant structures of sample Dis after 20 cycles of redox cycling (see figure 4.7(b)).

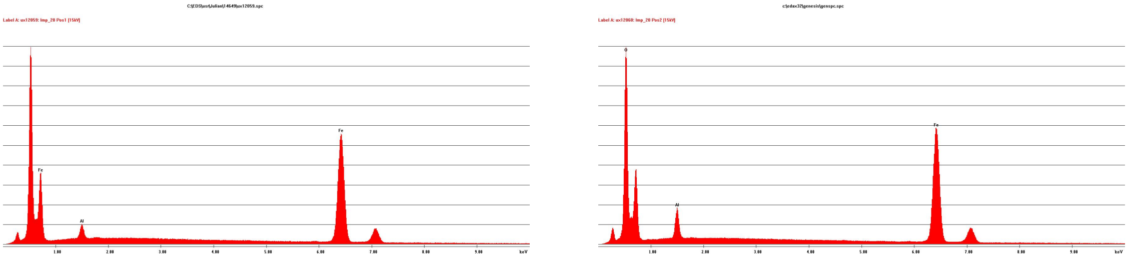

(a) Structure with higher porosity in figure 4.10(c).

(b) Structure with lower porosity inf igure 4.10(d).

Figure 9.4: EDX spectra of oxygen carrier Imp after 20 cycles of reduction and oxidation.

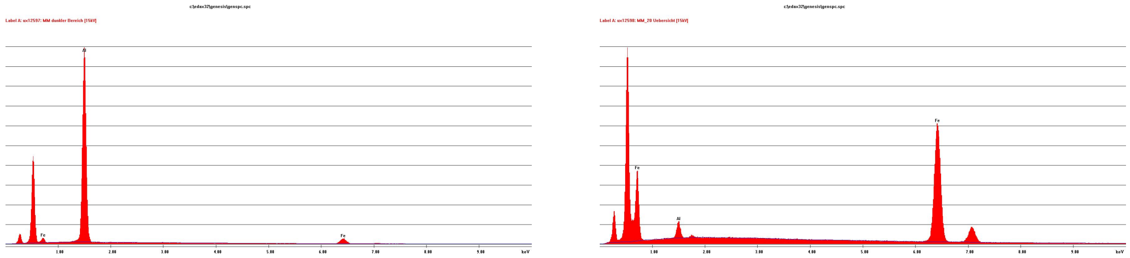

(a) Aluminium-rich phase of oxygen carrier MM as found in figure 4.11(c).

(b) Agglomerate which is found on a particle surface of oxygen carrier MM after redox cycling as seen in figure 4.11(d).

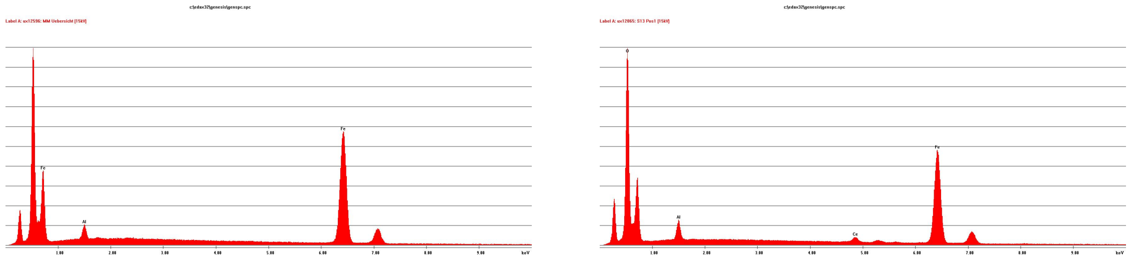

(c) Iron-rich phase of oxygen carrier MM before redox cycling as seen in figure 4.11(e).

(d) Fresh oxygen carrier of figure 4.30(a).

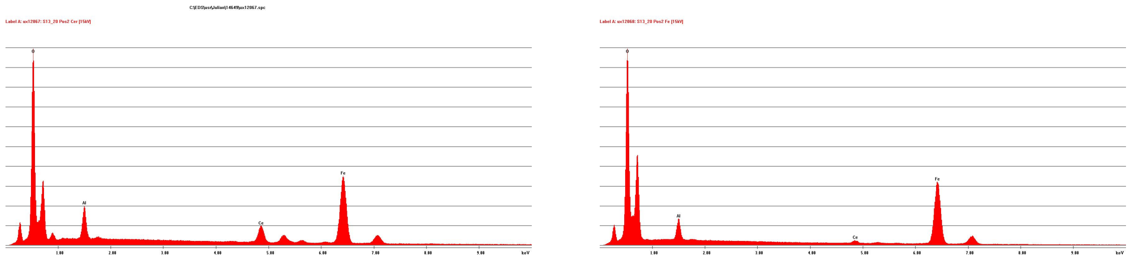

(e) Small, precipidated grains within the oxygen carrier after 20 redox cycles seen in figure 4.30(d).

(f) Large grains within the oxygen carrier after 20 redox cycles seen in figure 4.30(d).

Figure 9.5: EDX spectra of oxygen carriers MM and Fe - Al - Ce.